Salt marsh edge erosion due to wind-induced waves

Dissertation

submitted to and approved by the

Department of Architecture, Civil Engineering and Environmental Sciences

University of Braunschweig – Institute of Technology

and the

Department of Civil and Environmental Engineering

University of Florence

in candidacy for the degree of a

Doktor-Ingenieur (Dr.-Ing.) /

Dottore di Ricerca in Processes, Materials and Constructions in Civil and Environmental Engineering and for the Protection of the Historic-Monumental Heritage*)

by

(Michele Bendoni)

born (06/07/1984)

from (Bibbiena, AR), Italy

Submitted on	10/09/2015
Oral examination on	12/11/2015
Professorial advisors	Prof. (Luca Solari)
	Prof. (Hocine Oumeraci)

2016

*) Either the German or the Italian form of the title may be used.

A "quei ragazzi"...

(To "those guys"...)

Preface

The present manuscript contains the outcome of the PhD research carried out at the Department of Civil and Environmental Engineering of the University of Florence (Italy), at the Leichtweiss Institut for Hydraulic Engineering and Water Resources of the TU-Braunschweig (Germany), at the Water Science and Engineering Department of UNESCO-IHE, Delft (Netherlands) and at Deltares, Delft (Netherlands).

A crucial and "obvious" point to carry out a research activity is to clearly understand what a research activity is. I owe this understanding to my tutors, Prof. Luca Solari and Prof. Hocine Oumeraci. I am really grateful to them for what they taught me and for their support and encouragement during my PhD experience.

I am also grateful to Prof. Dano Roelvink, who strongly advised me during the period spent in the Netherlands and gave me the opportunity to join the XBeach developers community.

Many thanks to Eng.D. Simona Francalanci and Eng.D. Lorenzo Cappietti for the stimulating discussions and the valued suggestions provided me during the years of the PhD.

A great thank to Eng.D. Riccardo Mel, Eng. Chiara Pistoresi, Eng. Simone Bonistalli, Prof. Stefano Lanzoni and Marco Giada for their foundamental support during the field measurements activity, and to Prof. Simonetta Cola and Eng.D. Stefano Renzi for their advices and comments on the development of the toppling failure model.

I also want to thank all the PhD students and colleagues I meet during these years, and the secretaries, Serena and Gabi, who helped me a lot with administrative problems.

Last but not least, I want to thank all the precious persons who encouraged me during the PhD activity, especially during the moments when the research did not make headway. They know who they are. Thank to all, bar none.

I hope this research can give a significant contribution to the knowledge of the morphodynamic evolution of salt marshes and tidal environments, and inspire further research into this challenging topic.

Abstract

The erosion of the edge of the salt marshes due to wind waves modulated by tide is one of the chief mechanisms leading to marsh area reduction in various parts of the world. This entails the loss of a large amount of ecosystem services in estuarine and coastal environments.

Most part of the research on salt marshes focused on their vertical evolution, and less attention has been devoted to the lateral retreat mechanism.

The present research seeks to improve the knowledge about the erosion of the boundaries of the salt marshes, focusing on the processes occurring at the spatial scale of the salt marsh bank and the adjacent mudflat. The topic is addressed considering three different approaches, dealing with three different aspects of it.

The interpretation of laboratory experiments, previously carried out, inspired the development of a mathematical model describing the incipient mass failure of toppling type. The model is able to identify the wave group responsible for the failure of a block of soil identified by the presence of a tension crack. Furthermore, it gives information about the combinations of water level and wave height leading to bank instability, and it shows how the dynamic forcing of waves is crucial in promoting mass failure of toppling type.

A field campaign was carried out on a salt marsh of the lagoon of Venice. Localized and detailed measurements of erosion and wave climate provided the information to determine a relationship between wave energy flux and erosion rate at monthly time scale. A critical wave power value for the onset of erosion was identified around 1–2 W/m. In addition, field data demonstrated that in the monitored area the lower part of the bank is more prone to erosion than the top. This explains the formation of the characteristic cantilever profiles usually observed in the field. A simple mathematical model based on field data and field observations shows that the different erodibility of the marsh scarp along the vertical profile can lead to a higher cumulative retreat of the salt marsh edge.

The development of a 1-D process-based numerical model allowed to investigate, through numerical experiments, the effect of variations of soil composition on the temporal evolution of the bank profile, both in presence and in absence of vegetation. A salt marsh bank mostly composed by mud tends to retreat by maintaining the steep profile of the cliff, whereas decreasing the mud fraction the bank attains a more gentle and dissipative profile. The effect of vegetation in strengthening the soil matrix against shear erosion tends to be negligible for muddy banks. The lower the mud fraction, the stronger the effect of vegetation. Even for banks characterized by a similar amount of sand and mud, the presence of vegetation makes the bank to retreat maintaining a steep profile.

Present research gives several insights into the process of erosion of salt marsh edges due to the effect of wind-induced waves modulated by tide. Obtained results can be employed to evaluate and plan measures and interventions aimed at the preservation of salt marsh area in tidal environments. They can also lay the base for future researches and developments in the field of the morphodynamic evolution of tidal environments.

Contents

List of Figures

List of Tables

List of Symbols

A_{orb}	[m]	amplitude of wave orbital excursion
A_{tide}	[m]	tide amplitude
a_c	[m]	Van Rijn reference height
B	[g/m^2]	aboveground biomass
B_{max}	[g/m^2]	maximum aboveground biomass
b_{bg}	[g/m^2]	belowground biomass per unit area
b_F	[-]	relative bank freeboard
b_h	[m]	local salt marsh bank height
b_v	[m]	vegetation stem diameter
C	[m^3/m^3]	depth-averaged sediment concentration
C_a	[m^3/m^3]	sediment equilibrium concentration at reference level
C_{cu}	[N/m^2]	fatigue rupture strength of soil
C_{cz}	[m$^{1/2}$/s]	Chezy coefficient
$C_{cz,v}$	[m$^{1/2}$/s]	Chezy coefficient for a vegetated surface
C_D	[-]	drag coefficient
C_{Dv}	[-]	bulk drag coefficient for vegetation
C_E	[-]	empirical coefficient wave impact approach
C_{eq}	[m^3/m^3]	depth-averaged equilibrium sediment concentration
C_f	[-]	friction factor
CFL	[-]	Courant-Friedrichs-Levy number
C_m	[m^3/m^3]	depth-averaged mud concentration
C_r	[N/m^2]	root cohesion

C_s	[m^3/m^3]	depth-averaged sand concentration
c_d	[N·m·s]	rotational damping coefficient
c_x	[m/s]	wave group velocity
c_p	[m/s]	wave phase velocity
$c_{r,x}$	[m/s]	wave roller propagation velocity x direction
$c_{r,y}$	[m/s]	wave roller propagation velocity y direction
c_u	[N/m^2]	soil undrained shear strength
c_x	[m/s]	wave action propagation velocity x direction
c_y	[m/s]	wave action propagation velocity y direction
c_θ	[m/s]	propagation velocity in θ-space
c_σ	[m/s]	propagation velocity in σ-space
D	[m/s]	sediment deposition rate
D_b^*	[J/(m^2·s·rad)]	wave energy dissipation rate due to bottom friction per direction
D_b	[J/(m^2·s)]	wave energy dissipation rate due to bottom friction
D_{br}^*	[J/(m^2·s·rad)]	wave energy dissipation rate due to wave breaking per direction
D_{br}	[J/(m^2·s)]	wave energy dissipation rate due to wave breaking
D_m	[m/s]	mud deposition rate
D_s	[m/s]	sand deposition rate
D_{veg}^*	[J/(m^2·s·rad)]	wave energy dissipation rate due to vegetation per direction
D_{veg}	[J/(m^2·s)]	wave energy dissipation rate due to vegetation
d_{50}	[mm]	median grain diameter
d_*	[-]	dimensionless grain diameter
d_a	[m]	size of clay detaching aggregates
d_b	[m]	size of block in x direction
d_{PT}	[m]	distance of pressure transducer from the bottom
d_r	[J/(m^3·s)]	wave energy dissipation rate for equilibrium profile models
$d_{r,eq}$	[J/(m^3·s)]	equilibrium wave energy dissipation rate

d_{sc}	[m]	cell length for distribution of eroded material
E	[m/s]	sediment erosion rate
E_m	[m/s]	mud erosion rate
E_m^*	[m/s]	absolute erosion rate cohesive mixtures
E_r^*	[J/(m^2·rad)]	roller energy per direction
E_r	[J/m^2]	roller energy integrated over directions and frequencies
E_s	[m/s]	sand erosion rate
E_s^*	[m/s]	absolute erosion rate non-cohesive mixtures
E_{sc}	[m/s]	scarp erosion rate in vertical direction
E_{sc}^*	[m/s]	scarp erosion rate in horizontal direction
E_w^*	[J·s/(m^2·rad)]	wave energy per direction per frequency
E_w	[J/m^2]	wave energy integrated over directions and frequencies
e_0	[-]	void ratio
F_h	[N]	hydrostatic force
F_{hc}	[N]	hydrostatic force due to water in the crack
F_{hydro}^*	[N/m]	hydrostatic thrust per width on rigid model
F_l	[m]	fetch length
$F_{low,up,L,R}$	[m^2/s]	numerical fluxes
F_s	[-]	shape factor for sediment concentration profile
F_T	[N]	force per unit width due to incident wave computed by linear theory
F_w	[N]	force generated by wave impact acting on the block
F_{wb}	[N]	force generated by wave impact from PT data
F_w^*	[N/m]	force per unit width generated by wave impact on rigid model
$\bar{F}_{w,m}^*$	[N/m]	averaged maximum wave thrust per width on rigid model
$F_{w,max}^*$	[N/m]	absolute maximum wave thrust per width on rigid model

$F^{*}_{w,min}$	[N/m]	absolute minimum wave thrust per width on rigid model
F_{veg}	[N/m]	force per unit width due to vegetation
f_c	[1/s]	cut-off frequency
f_{mor}	[-]	morphological acceleration factor
f_p	[1/s]	peak frequency
f_s	[1/s]	sampling frequency
f_w	[-]	wave friction factor
G	[N/m^2]	soil shear modulus
g	[m^2/s]	gravitational acceleration
H_i	[m]	incident component of wave height
H_r	[m]	reflected component of wave height
H_{m0}	[m]	significant wave height
$H_{m0,E}$	[m]	estimated significant wave height
$H_{m0,M}$	[m]	measured significant wave height
H_{rms}	[m]	root-mean-square wave height
h	[m]	water depth
I_b	[kg·m^2]	moment of inertia of the block
I_s	[m^4]	moment of inertia of the failure surface
K_{bf}	[m^3/(kg·yr)]	wave erosion calibration coefficient
K_p	[-]	pressure response factor
K_r	[-]	wave reflection coefficient
K_{sp}	[-]	correction coefficient for dynamic spring stiffness
K_T	[m^4/N]	transport coefficient for equilibrium profile models
KC	[-]	Kulegan-Carpenter number
k	[1/m]	wave number
k_b	[-]	dimensionless vegetation parameter
k_p	[m/s]	soil permeability
k_s	[m]	Nikuradse roughness
k_{sp}	[N·m]	rotational spring stiffness
L	[m]	representative wave length

L_b	[m]	width of the block in y direction
L_{er}	[m]	erosion length at an erosion pin
L_p	[m]	reference length associated to an erosion pin
l_b	[m]	depth of the tension crack
M	[kg/(m^2·s)]	generic erosion parameter
M_D	[N·m]	moment due to dashpot
M_S	[N·m]	moment due to spring
M_c	[kg/(m^2·s)]	erosion parameter for cohesive mixtures
M_{nc}	[kg/(m^2·s)]	erosion parameter for uncohesive mixtures
M_{sc}	[m^3/J]	scarp erodibility coefficient
m_0	[m^2]	zero-th moment of the wave spectral density
m_b	[kg]	mass of the block subject to incipient failure
m_{hr}	[kg]	hydrodynamic added mass for rotational motion
$m_{j,k}$	[kg/m^2]	mass of the j-th sediment class in the k-th layer related to a specific cell area
m_k	[m^3/(W·yr)]	ratio of average erosion rate to wave power for the k-th bank portion
m_{toe}	[m^3/(W·yr)]	erodibility of the bank toe
m_{top}	[m^3/(W·yr)]	erodibility of the bank top
m^*_{sc}	[kg/(J·m)]	scarp erodibility coefficient
N	[J·s/(m^2·rad)]	wave action
N_{PT}	[-]	number of pressure transducers
N_p	[-]	number of erosion pins
N_s	[-]	number of sediment classes in the bed
N_v	[units/m^2]	vegetation stem density
n_p	[-]	bed porosity
p	[N/m^2]	pressure
$\hat{p}$	[m^2/s^2]	non-hydrostatic pressure normalized by density
p_d	[N/m^2]	dynamic component of wave-induced pressure
p_i	[-]	i-th sediment class mass fraction
p_m	[-]	mud mass fraction

$p_{m,cr}$	[-]	critical mud content
$p_{m,i}$	[N/m^2]	pressure measured by i-th PT
p_s	[-]	sand mass fraction
$\mathbf{q_b}$	[m^2/s]	bed-load sediment transport
$\mathbf{q_s}$	[m^2/s]	suspended sediment transport
$\mathbf{q_t}$	[m^2/s]	total sediment transport
RAR	[-]	root area per unit area of soil
R_{sc}	[m^3/(m·s)]	scarp volumetric erosion rate
r_d	[m]	depth of the root mat
S_{pp}	[m^2]	piezometric head spectrum
S_{sh}	[m/s]	speed of the discontinuity
S_{tot}	[J/(m^2·s·rad)]	source term in action balance equation
S_{xx}	[N/m]	wave radiation stress in x direction
$S_{\eta\eta}$	[m^2]	wave spectral density
s_f	[kg/m^2]	wave induced stress at bank toe
$s_{f,cr}$	[kg/m^2]	threshold wave induced stress for erosion
s_{max}	[m]	maximum scour depth for cantilever failure
s_{sc}	[-]	slope threshold for scarp erosion
T	[-]	dimensionless transport parameter
T_{nc}	[-]	dimensionless transport parameter non-cohesive mixtures
T_p	[s]	wave peak period
T_{rep}	[s]	representative wave period
T_{run}	[days]	duration of the simulation
T_s	[s]	adaptation time scale for sediment settling velocity
T_{tide}	[s]	tidal period
t_r	[N/m^2]	root tensile strength
U_w	[m/s]	wind speed
u	[m/s]	flow velocity in x direction
$u_{cr,v}$	[m/s]	critical erosion velocity in presence of vegetation

u_E	[m/s]	Eulerian flow velocity in x direction
u_L	[m/s]	Lagrangian flow velocity in x direction
u_{rms}	[m/s]	root-mean-squared orbital velocity due to waves
u_S	[m/s]	Stokes velocity in x direction
V_{La}	[m/s]	"Lysmer's analog" wave velocity
v	[m/s]	flow velocity in y direction
v_E	[m/s]	Eulerian flow velocity in y direction
v_L	[m/s]	Lagrangian flow velocity in y direction
v_S	[m/s]	Stokes velocity in y direction
$\mathbf{v}$	[m/s]	2D velocity vector
W	[W/m]	wave energy flux
W_b	[N]	block weight
W_{cr}	[W/m]	wave energy flux threshold for erosion
W_n	[m^2/Hz]	noise floor of pressure transducer
$w_{s,m}$	[m/s]	mud settling velocity
$w_{s,s}$	[m/s]	sand settling velocity
x_b	[m]	bed morphology function
x_{avg}	[m]	average position of the scarp in x-direction
x_{toe}	[m]	position of the toe of the scarp in x-direction
x_{top}	[m]	position of the top of the scarp in x-direction
Z	[m]	elevation of rotating point $\bar{O}$ with respect to mean water level
Z_w	[m]	arm of the wave forcing in the model for toppling failure
z_0	[m]	bed roughness
z_b	[m]	bottom elevation
z_{b0}	[m]	initial bottom elevation
z_i^{PT}	[m]	position of the PT with respect to the bottom of the flume
z_p	[m]	pin elevation with respect to P.S.
αh	[m]	vegetation height
β_0	[rad]	average slope of the bank

γ	[-]	peak enhancement factor
Δ_i	[m]	thickness of i-th layer
Δ_s	[-]	dimensionless sediment submerged density
ΔT	[days]	interval between two consecutive surveys
ΔW_s	[N/m]	weight of eroded material due to wave impact
Δt	[s]	time step for numerical simulations
Δt_{ji}	[hours]	time during which erosion occurs at a specific i-th pin in j-th sector
Δx	[m]	cell length in numerical simulations
$\Delta\theta$	[rad]	wind direction range influencing a certain salt marsh sector
ϵ_h	[m^2/s]	sediment horizontal dispersion coefficient
ζ_0	[-]	surf similarity parameter
η	[m]	water surface displacement
η_i	[m]	water surface displacement due to incident wave component
θ	[rad]	wave direction
θ_n	[rad]	direction normal to a sector of the salt marsh
θ_w	[rad]	wind direction
κ	[-]	von Karman constant
ν	[m^2/s]	water kinematic viscosity
ν_P	[-]	Poisson coefficient (soil)
ρ	[kg/m^3]	water density
ρ_{root}	[kg/m^3]	root mass density
ρ_s	[kg/m^3]	sediment bulk density
φ	[rad]	angle of oscillation of the block
σ	[rad/s]	intrinsic wave frequency
σ_s	[N/m^2]	normal stress on soil matrix
τ_b	[N/m^2]	bottom shear stress
τ_c	[N/m^2]	bottom shear stress due to currents
τ_{cr}	[N/m^2]	critical shear stress for sediment erosion

$\tau_{cr,c}$	[N/m^2]	critical shear stress for cohesive mixtures
$\tau_{cr,d}$	[N/m^2]	critical shear stress for sediment deposition
$\tau_{cr,m}$	[N/m^2]	critical shear stress for pure mud
$\tau_{cr,nc}$	[N/m^2]	critical shear stress for non cohesive mixtures
$\tau_{cr,s}$	[N/m^2]	critical shear stress for pure sand
$\tau_{cr,v}$	[N/m^2]	critical shear stress in presence of vegetation
τ_{dep}	[N/m^2]	critical shear stress for deposition
τ_m	[N/m^2]	bottom shear stress due to wave-current interaction
τ_{xx}	[m^2/s^2]	horizontal turbulent stress normalized by density
τ_{xy}	[m^2/s^2]	horizontal turbulent stress normalized by density
τ_{yx}	[m^2/s^2]	horizontal turbulent stress normalized by density
τ_{yy}	[m^2/s^2]	horizontal turbulent stress normalized by density
τ_w	[N/m^2]	bottom shear stress due to waves
φ	[rad]	angle of the vertical axis of the block of soil with respect to the vertical
ψ_1	[m^2/s^2]	dispersive terms x direction
ψ_2	[m^2/s^2]	dispersive terms y direction

Chapter 1

Introduction

1.1 Problem statement and motivations

In the last years, tidal wetlands and salt marshes have been receiving increasing attention by the scientific community, due to their role in providing ecosystem services to coastal population [*Barbier* et al., 2011].

Ecosystem services are defined as the benefits that humans derive from the natural ecosystems and they are intrinsic features of healthy natural environments [*Ojea* et al., 2012]. Tidal wetlands and salt marshes provide a unique habitat for several plants and animal species. Moreover, they act as a buffer reducing the input of contaminants to estuaries, and provide a first defence barrier against storm surges and flooding, principally due to the presence of halophytic vegetation [*Gedan* et al., 2011]. These properties generate a really high and valuable natural capital which deserves to be protected [*Costanza* et al., 1997].

Nevertheless, several factors such as increasing anthropic pressure, sea level rise, subsidence and the intensifying of erosive processes are threatening the extent of the salt marsh area in various parts of the world [*Gedan* et al., 2009].

The erosion of the boundaries of the salt marshes due to the effect of surface waves is one of the chief mechanisms leading to marsh area loss [*Schwimmer*, 2001; *Marani* et al., 2011]. On the one hand, salt marshes likely have the capability to keep peace with the sea level rise if enough sediment are available [*French*, 2006; *Kirwan* et al., 2010] but, on the other hand, they are quite vulnerable to the lateral erosion process even in absence of sea level rise [*Mariotti* and *Fagherazzi*, 2013a; *Fagherazzi* et al., 2013].

This results in a rather delicate issue, since the presence of salt marshes reduces the energetic density of the flow in case of storm surges and flooding [*Möller* et al., 2014], but the boundaries of the marsh area can be subject to intense erosive processes [*Day* et al., 1998; *Van der Wal* et al., 2008]. In addition, the "building with nature" philosophy [*De Vriend* and *Van Koningsveld*, 2012] is nowadays promoting the coupling of traditional measures (sea dikes, embankments) and soft measures (restoration of marsh area) to cope with coastal risk reduction [*Temmerman* et al., 2013].

Thus, it is necessary to improve the knowledge about the lateral erosion of the salt marsh boundaries induced by waves at shorter temporal scales (order of days to months), in order to better understand the mechanisms underlying the process.

Horizontal migration of salt marsh banks is an eco-morphodynamic process in which a large diversity of factors, such as the characteristics of the flow filed, of the morphology and of the vegetation interact, leading to a rather complex dynamic of the system. The latter is generally characterized by the alternation of continuous erosion and occasional mass failures. Currently, failure events have been described only qualitatively [*Allen*, 1989], except the study by *Van Eerdt* [1985a]. Field measurements mainly aimed at interpreting the retreat mechanism were performed at large spatial and temporal scales in the order of km and years [*Schwimmer*, 2001; *Marani* et al., 2011] and local measurements of the erosive effect of waves on the scarp of the salt marshes are hardly available in the literature. Furthermore, mathematical modelling to describe the dynamic of the salt marsh boundary essentially focused on the long term evolution of the system, necessarily simplifying some aspects of the involved processes [*Mariotti* and *Fagherazzi*, 2010, 2013a].

1.2 Objectives

The main objective of the present work is to investigate the process of lateral erosion of salt marshes due to the combined effect of wind-induced waves. Three different aspects of the topic will be investigated.

First, the results of a previous experimental activity [*Francalanci* et al., 2013] will be accurately interpreted in order to derive a mathematical model for the mass failure of toppling type as observed in laboratory experiments.

The determination of a relationship, at short time scale (i.e. the order of months), between the wave energy flux impinging the marsh edge and the volumetric erosion rate per unit width, and the effect of mass failures on marsh cumulative retreat, will be addressed through a detailed field measurement campaign on a salt marsh of the Lagoon of Venice.

The role played by soil composition and the presence of vegetation on the erosive mechanism of a salt marsh subject to continuous wave forcing, are investigated through the implementation of several additional physical processes relevant for salt marshes in the numerical model XBeach, which was initially developed for sand beaches and dunes under storm surges and waves [*Roelvink* et al., 2009].

1.3 Methodology

The adopted research methodology is reflected by the following outline of the thesis.

Chapter 2 contains the current state of the art on the topic, developed on a detailed analysis of the available literature. The gaps of knowledge and in the current interpretations of the processes underlying salt marsh bank erosion are identified in order to specify more precisely the objectives and methodology of the research.

In Chapter 3, a mathematical model for the description of the incipient toppling failure is reported. It is based on the results of an experimental activity related to the study of the effect of wind waves and tide on a salt marsh bank by means of laboratory experiments performed in a wave flume [*Francalanci* et al., 2013].

Chapter 4 is dedicated to the field measurement campaign carried out from November 2013 to April 2015 on a salt marsh bank of the Lagoon of Venice. Horizontal retreat of the salt marsh edge was measured by means of erosion pins distributed horizontally on the scarp. Wave height was measured through pressure transducers in the field, and put in correlation with the wave climate estimated from wind, fetch and bathymetry data, thus reducing the needs for recurrent field measurements. A relationship was found between wave energy flux and erosion rate at monthly time scale. Finally, a simple mathematical model was developed to describe the effect of mass failures on cumulative bank retreat.

In Chapter 5, a 1-D hydro-morphodynamic numerical model is developed within the existing XBeach code [*Roelvink* et al., 2009]. Several processes relevant for salt marsh bank are additionally implemented in the model: interaction between sand and mud, possible wave reflection, effect of wave impact on the lateral retreat with a new formula for the bed update in presence of steep slope, and stabilizing effect of vegetation roots. The model is then used to carry out a sensitivity analysis of the main parameters on the evolution of salt marsh bank profile.

In the final chapter, the key results of the research activity are summarized and concluding remarks are drawn, including suggestions for further developments.

Chapter 2

Review and Analysis of Current Knowledge and Modelling

This chapter aims at reviewing and analysing the current knowledge on the erosion of salt marsh edges induced by wind-generated waves in connection with the salt marsh dynamics in a tidal environment. The available knowledge of the related processes and their modelling is analysed in order to identify the knowledge gaps and to specify more precisely the objectives and the methodology of the PhD study.

2.1 Salt marshes and salt marsh ecosystem services

Salt marshes are muddy flat lands covered chiefly by halophytic vegetation periodically flooded by tidal waves [*Allen*, 2000], where fine sediments are transported by water and stabilized by vegetation [*Boorman*, 2003]. They form along coastlines where hydraulic forcing is moderate enough to allow the accumulation of sediments and the growth of vegetation. Thus, sheltered environments such as lagoons, estuaries, shallow bays, landward sides of barrier islands and spits are adequate to accommodate salt marshes. They are also common near large rivers and deltas, which provide the sediment input for their formation and evolution [*Chapman*, 1974; *Weinstein* and *Kreeger*, 2000]. Indeed, gentle nearshore slopes, which commonly develop in macrotidal coasts and coasts adjacent to major river deltas, damp waves sufficiently to allow the development of fringing marshes. These geomorphic structures usually turn seaward into mudflats or sandflats, from which they can be separated by a ramp, or a cliff with a generalized erosive trend. Landwards, they can develop into freshwater marshes and coastal woodland communities [*Friedrichs* and *Perry*, 2001; *Allen* and *Pye*, 1992].

Salt marshes, together with mudflats and the meandering channels network are part of tidal environments and lagoons which dynamics are controlled by complex and often non-linear interactions among hydrodynamics, morphodynamics and ecological processes [*Allen*, 2000; *Van de Koppel* et al., 2005; *Marani* et al., 2010; *Mariotti* and *Carr*, 2014]. Erosion, deposition and sediments transport determine the morpohological characteristics of tidal environments, influencing ecosystem behaviour, vegetation development and hydrodynamics [*Fagherazzi* et al., 2012; *Da Lio* et al., 2013]. Vegetation, in turn, affects transport and trapping of inorganic sediments by increasing surface roughness and marsh elevation. The latter is also affected by the production of organic matter added on the marsh surface [*Morris* et al., 2002; *D'Alpaos* et al., 2007].

Salt marshes are located all over the world, mainly in low-energy coasts at temperate and high latitudes as well as in macrotidal to microtidal regimes [*Allen* and *Pye*, 1992], experiencing diverse modifications in plant typologies and species differentiation with changes in latitude and surrounding environments [*Adam*, 1993].

Nowadays, they are threaten by several factors, such as anthropic pressure, sea level rise, subsidence and hydrodynamic forcings [*Van der Wal* and *Pye*, 2004; *Gedan* et al., 2009; *Kirwan* and *Temmerman*, 2009; *Kirwan* et al., 2010]. A general reduction in marsh area is occurring, for example, in the Lagoon of Venice (Italy) [*Sarretta* et al., 2010].

The Venice Lagoon is located in the northern part of Italy. It has a surface area of roughly 550 km^2, a length of 55 km and a maximum width of 15 km. Its watershed is 1800 km^2 large [*Ravera*, 2000]. It is characterized by a microtidal regime and three inlet openings connecting it hydraulically to the Adriatic Sea. This environment has experienced, since a long time, intense and varied human impacts that range from reclamation, dredging, river diversion, fishing and livestock grazing, to more modern activities such as restoration efforts and the built of sea defence structures against extreme high water levels (e.g. MOSE[1]).

The combination of natural processes, human activities and sedimentological feedbacks produced significant morphological changes in the Lagoon of Venice since the 10th century [*D'Alpaos*, 2010, in italian]. Therefore, the case of Venice represents a typical example of the search for a balance between human activities such as industrial, commercial and tourist development on the one hand, and the conservation and safety of the fragile lagoon ecosystem on the other hand [*Yu* et al., 1996; *Pranovi* et al., 2003; *D'Alpaos*, 2010; *Solidoro* et al., 2010].

Recent studies [*Sarretta* et al., 2010], based on the comparative observation of the areal distribution of bed elevation, showed a decrease by more than 50% of the whole area of salt marshes of the lagoon of Venice, passing from 68 km^2 in 1927 to 32 km^2 in 2002 and the deepening of the bottom with a significant increase in the area of tidal flats from 88 to 206 km^2 in the same period (Figure 2.1). This shows that salt marshes in the Venice Lagoon are generally subject to a permanent erosion as also reported by *Carniello* et al. [2009] too. Moreover *Day* et al. [1998] observed a rapid deterioration of salt

[1] https://www.mosevenezia.eu/

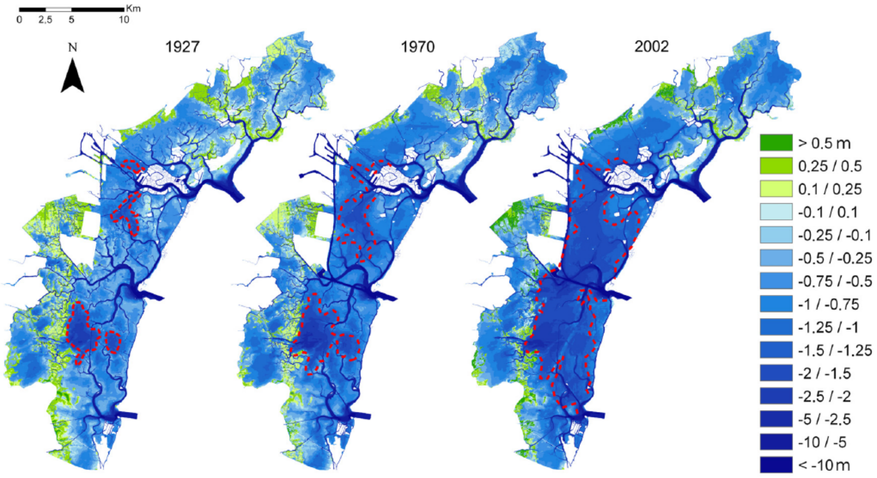

Figure 2.1: Colour-shaded bathymetric maps of the lagoon of Venice (from left to right: 1927, 1970, 2002). Dotted red line indicates migration of -1.2 m contour line, showing an overall increase in depth (progressively darker blue colour). Emergent areas are indicated in green [after *Sarretta* et al., 2010].

marshes in the Venice Lagoon, based on field measurements of diverse aspects of sediment dynamics and geomorphological changes. Marsh edge retreat rates up to 1.2–2.2 m/yr and growth of wave-cut gullies were caused by high wave energy fluxes generated by strong winds with large fetches.

Nowadays, the exploitation of natural resources and environmental changes may expose tidal environments to irreversible transformations with severe ecological and socio-economic consequences [*Day* et al., 2007; *Gedan* et al., 2009; *Silliman* et al., 2012]. Indeed, a highly valuable biodiversity and a high primary production are typical characteristics of salt marshes and tidal environments, but their importance also consists in providing diverse and valuable "ecosystem services" to human communities. Ecosystem services are the benefits that humans derive from ecological systems and are generated directly from the processes that sustain ecosystems [*Ojea* et al., 2012]. Several studies were aimed at the quantification of their socio-economical value and importance [*De Groot* et al., 2002; *Costanza* et al., 2006], devoting particular attention to coastal environments [*Zedler* and *Kercher*, 2005; *Barbier* et al., 2008, 2011].

Salt marshes furnish a habitat for a large number of species and a preferential zone for fish nurseries [*Boesch* and *Turner*, 1984]. They are important sinks of carbon dioxide [*Chmura* et al., 2003] or nitrogen and phosphorous, reducing nutrients input to estuaries [*Gosselink* and *Pope*, 1974; *Valiela* and *Teal*, 1979]. Mainly due to the presence of vegetation, salt marshes play an important role in protecting shorelines through dissipation of wave energy [*Möller* and *Spencer*, 2002; *Möller* et al., 2014], reducing the needs for maintenance of sea walls or dikes to protect the hinterland and acting as an ecosystem-based coastal defence against floods, storm surges and hurricanes [*Costanza* et al., 2008; *Gedan* et al., 2011; *Shepard* et al., 2011; *Temmerman* et al., 2013]. Moreover, the binding effect of plant roots on soil can prevent shoreline erosion [*King* and *Lester*, 1995; *Coops* et al., 1996; *Chen* et al., 2012]. Recently, however, *Feagin* et al. [2009] raised doubts about this statement, showing that the role played by vegetation in preventing erosion needs a closer examination.

For all the above reasons, salt marshes generate some of the highest and most valuable ecosystem services among natural ecosystems [*Costanza* et al., 1997; *Barbier* et al., 2011]. At present, one of the main motivations for the protection of such environments is to preserve the quality and quantity of the services they directly and indirectly provide to human communities.

For the sake of completeness, it is worth noting that salt marshes are recognized as one of the key habitat in the European Habitat directive [*Council of European Union*, 1992] and, for example, many of the UK estuaries are designed as Areas of Outstanding Natural Beauty, National Natural Reserve, Special Area of Conservation and Site of Special Scientific Interest.

2.2 Processes underlying salt marsh bank erosion and their modelling

One of the main mechanisms contributing to marsh reduction is the erosion of the bank edge by wind-generated waves [*Schwimmer*, 2001; *Mariotti* and *Fagherazzi*, 2010; *Marani* et al., 2011], which usually induce a lateral migration of the marsh boundary. The retreat of the marsh boundary is a complex phenomenon involving the characteristics of flow field, soil, vegetation and bank geometry. Typical structures of salt marsh banks and adjacent mudflats for several salt marshes located in different areas worldwide are illustrated in Figure 2.2. It is possible to notice the presence of a net discontinuity between the vegetated marsh and the mudflat, even if the marsh edge is small or almost absent.

A general distinction can be made between the description of the hydrodynamic processes and those related to sediment transport and morphological changes. Nevertheless, the biological aspects, related for example to vegetation and biota, may have an active role in determining erosive trends [*Van Eerdt*, 1985b; *Le Hir* et al., 2007; *Chen* et al., 2012], but their evolution occurs over larger temporal scales with respect to the specific erosion process. For this reason, the description of their dynamics is not part of the review, whereas their effect in modifying hydrodynamics and bank erodibility is considered.

If erosion is conceived as the ensemble of processes through which material is worn away from earth surface, it is possible to distinguish two fundamental way in which the marsh scarp can retreat landward: surface and mass erosion, and mass failure [*Winterwerp* et al., 2012]. The former is characterized by the continuous detachment of particles from a surface (under drained or undrained

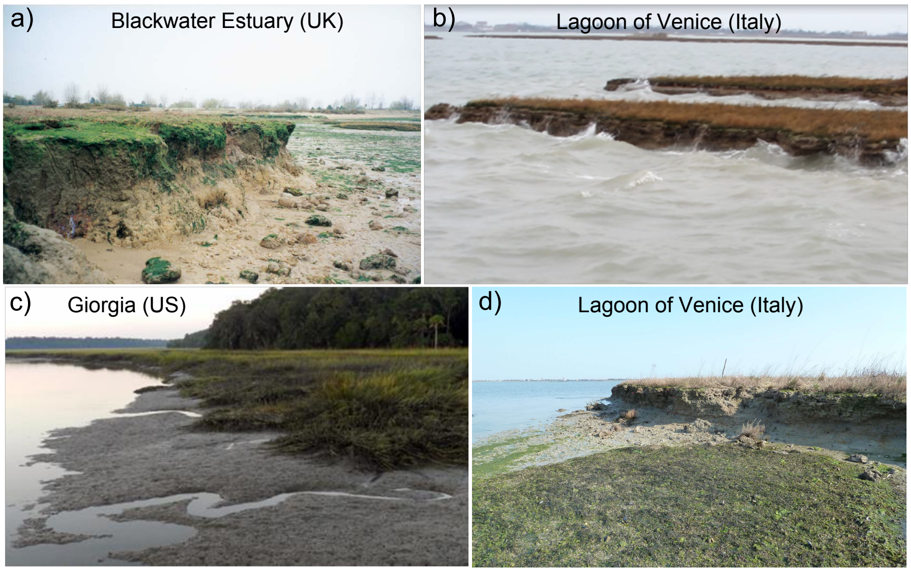

Figure 2.2: Pictures depicting salt marsh banks and adjacent tidal flat. a) Marsh cliff in St. Lawrence Bay, Blackwater Estuary (UK) [after *Van der Wal* and *Pye*, 2004]. b) Salt marsh subject to wave attack in the Lagoon of Venice (Italy). c) Tidal marsh located in Georgia (US). d) Marsh cliff in the Lagoon of Venice (Italy) and partially vegetated tidal flat.

conditions); the latter is a discontinuous process of the detachment of the whole portion of material of different sizes, generally from a bank, that can occur in several ways such as rotational slips, cantilever failures, toppling and other typologies of failures depending on the configuration of the bank itself [*Van Eerdt*, 1985a; *Thorne* and *Tovey*, 1981]. For the sake of simplicity, the term "surface erosion" will be used hereafter to indicate mass and surface erosion, unless otherwise specified. Both processes are mostly driven by hydrodynamic processes and gravity and are strongly influenced by the presence of vegetation, the typology of the material and the morphology. It is obvious that such a distinction is a simplification and that the two processes may occur in the same time influencing each other and that the amount and size of particle aggregates detached by waves can vary strongly.

Salt marsh bank retreat was specifically studied by several authors qualitatively or proposing conceptual models [*Allen*, 1989; *Pringle*, 1995; *Allen*, 2000; *Van der Wal* et al., 2008; *Wilson* and *Allison*, 2008; *Chauhan*, 2009]. On the other hand, some attempts have been made in order to develop a mathematical description of the phenomenon. Some studies are based on empirical data and field measurements [*Schwimmer*, 2001; *McLoughlin* et al., 2014] and on dimensional analysis [*Marani* et al., 2011]. Others considered bank retreat as a subset of morphodynamic models describing the temporal evolution of a marsh transect [*Mariotti* and *Fagherazzi*, 2010, 2013a] or focused on the longitudinal evolution of the boundary [*Leonardi* and *Fagherazzi*, 2014]. Moreover, the stability of the marsh cliff depending on the geometrical profile and soil characteristics was studied by *Van Eerdt* [1985a] and *Gabet* [1998].

To get a clear view of the phenomenon, Figure 2.3 depicts a scheme of the interaction of the diverse processes leading to marsh retreat.

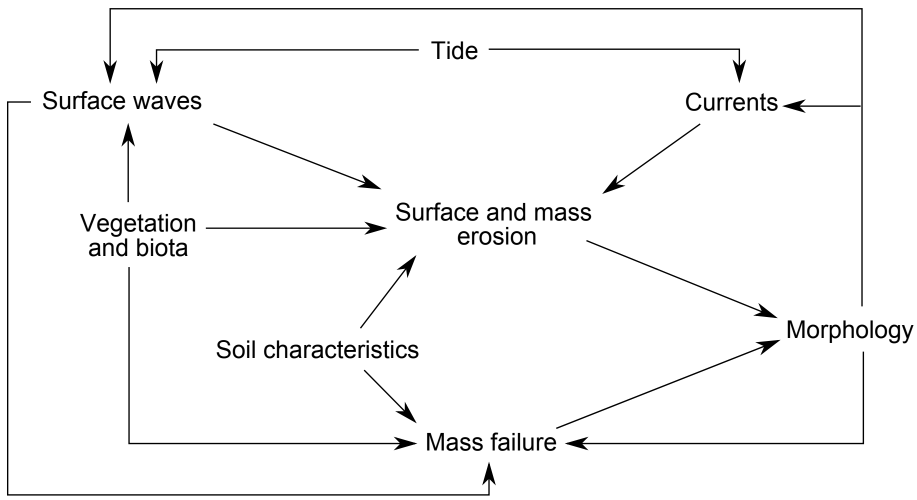

Figure 2.3: Interaction among processes and elements leading to bank retreat (processes related to marsh growth, such as organic and inorganic deposition, vegetation dynamic or sediment compaction are not considered).

In this scheme, all the processes related to the growth of the salt marsh due to organic and inorganic sediment deposition, vegetation dynamic and sediment trapping are not considered. Furthermore, the effect of sediment compaction or subsidence are not addressed in this study. With reference to Figure 2.3, tide generates currents and influences surface wave propagation, which are mainly responsible for surface erosion and mass failures and are affected by the local morphology and the presence of vegetation. Erosive processes are affected by soil composition and the presence of roots and generate morphological changes of the system, which in turn affect, at shorter temporal scales, hydrodynamics, and at longer, vegetation dynamics.

In the following sections, the current knowledge and modelling of the hydrodynamic and morphodynamic processes is reviewed and analysed, followed by the effect of vegetation.

2.2.1 Hydrodynamic processes

Hydrodynamics play a crucial role in shaping bank morphology. This study is focused on the effect of wind-generated waves, whereas ship-induced waves are not specifically addressed. Water level variations due to the effect of tide modulate wave forcing affecting the wave energy flux reaching the bank. Wind waves can be modelled, in general, by means of Airy Linear Wave Theory [*Dean* and *Dalrymple*, 1991] and nonlinear wave theories, such as Stokes' Wave Theory [*Stokes*, 1847; *Dingemans*, 1997]. Both linear and nonlinear theories provide analytically the flow field under surface waves for specific boundary conditions.

Another kind of distinction can be made between phase-resolving and phase-averaging models, which consider, respectively, the numerical resolution of continuity and momentum equations [*Madsen* et al., 1991; *Tonelli* et al., 2010; *Zijlema* et al., 2011], and wave action balance equation [*Hasselmann* et al., 1973; *Booij* et al., 1999].

The former usually employ Nonlinear Shallow Water Equations (NSWE) or Boussinesq Equations and provide the instantaneous flow field in term of depth averaged velocity $\mathbf{v} = [u(x, y, t), v(x, y, t)]^T$ and surface elevation $\eta(x, y, t)$. The model by *Zijlema* et al. [2011] is able to simulate non-hydrostatic flows and give a correct representation of the effect of frequency dispersion by increasing the number of vertical layers. Conceptually, the vertical structure of the flow is part of the solution, although the model remains depth averaged. *Tonelli* et al. [2010] propose a Boussinesq-type model in which dispersive terms are neglected in shallow water where nonlinear terms are predominant. Both models are sufficiently able to capture the wave breaking processes, provided a specific tuning parameter. The continuity and momentum equations are formulated as follows:

$$\frac{\partial \eta}{\partial t} + \frac{\partial hu}{\partial x} + \frac{\partial hv}{\partial y} = 0 \tag{2.1a}$$

$$\frac{\partial u}{\partial t} + u\frac{\partial u}{\partial x} + v\frac{\partial u}{\partial y} + g\frac{\partial \eta}{\partial x} = C_f \frac{u\sqrt{u^2+v^2}}{h} + C_x \tag{2.1b}$$

$$\frac{\partial v}{\partial t} + u\frac{\partial v}{\partial x} + v\frac{\partial v}{\partial y} + g\frac{\partial \eta}{\partial y} = C_f \frac{v\sqrt{u^2+v^2}}{h} + C_y \tag{2.1c}$$

where $h = \eta - z_b$ is the water depth, z_b the coordinate of the bottom C_f the friction factor and C_x and C_y are two terms depending on the applied model, defined as follows:

$$C_x = \begin{cases} -\dfrac{1}{h}\displaystyle\int_{-d}^{\eta} \frac{\partial \hat{p}}{\partial x} dz + \frac{1}{h}\left(\frac{\partial h\tau_{xx}}{\partial x} + \frac{\partial h\tau_{xy}}{\partial y}\right), & \text{for } \textit{Zijlema} \text{ et al. [2011]} \\ \dfrac{\psi_1}{h}, & \text{for } \textit{Tonelli} \text{ et al. [2010]} \end{cases}$$

$$C_y = \begin{cases} -\dfrac{1}{h}\displaystyle\int_{-d}^{\eta} \frac{\partial \hat{p}}{\partial y} dz + \frac{1}{h}\left(\frac{\partial h\tau_{yx}}{\partial x} + \frac{\partial h\tau_{yy}}{\partial y}\right), & \text{for } \textit{Zijlema} \text{ et al. [2011]} \\ \dfrac{\psi_2}{h}, & \text{for } \textit{Tonelli} \text{ et al. [2010]} \end{cases}$$

in which $\hat{p}(x, y, z, t)$ is the non-hydrostatic pressure (normalized by water density ρ), τ_{xx}, τ_{xy}, τ_{yx} and τ_{yy} are the averaged horizontal turbulent stress terms and ψ_1 and ψ_2 collect the modified dispersive terms.

The latter approach provides an averaged description of waves by means of the spectral action balance $N(x, y, \sigma, \theta, t)$, that is the ratio of the wave energy $E_w(x, y, \sigma, \theta, t)$ to the wave frequency σ [*Booij* et al., 1999]:

$$\frac{\partial N}{\partial t} + \frac{\partial c_x N}{\partial x} + \frac{\partial c_y N}{\partial y} + \frac{\partial c_\sigma N}{\partial \sigma} + \frac{\partial c_\theta N}{\partial \theta} = \frac{S_{tot}}{\sigma} \tag{2.3}$$

where θ is the wave direction, $c_x = c_g \cos\theta + u$, $c_y = c_g \sin\theta + v$, c_σ and c_θ are the propagation velocities in the respective spaces, and c_g is the group velocity. S_{tot} is the source term, representing the sum of wave generation, dissipation and nonlinear wave-wave interaction in terms of energy density. In this case the wave breaking process is described by a parametric breaking model [*Battjes* and *Janssen*, 1978; *Roelvink*, 1993; *Baldock* et al., 1998]. To get the significant wave height H_{m0}, the quantity $N \cdot \sigma = E^*_w$ has to be integrated over all frequencies and wave directions to get the zero-th moment of the wave energy density spectrum:

$$m_0 = \frac{1}{\rho g} \int_0^\infty \int_0^{2\pi} E^*_w(x, y, \sigma, \theta, t)\, d\theta d\sigma \tag{2.4}$$

then:

$$H_{m0} = 4\sqrt{m_0}. \tag{2.5}$$

Three dimensional Navier Stokes-based models are also available [*Lin* and *Liu*, 1998; *Dalrymple* and *Rogers*, 2006] which can describe the entire wave breaking process (e.g. OpenFOAM[2]); however, they are generally computationally expensive and therefore not considered in this study.

For the propagation of long waves such as tidal waves, NSWE-based models are commonly used [*Defina*, 2000; *Carniello* et al., 2005]. However, a detailed study of the effect of tidal waves in modulating wave impact and of the tide-induced currents won't be specifically addressed. As a starting point, it is indeed assumed a simple sinusoidal tide in order to avoid to add more complexity to the study. Regarding tide-induced currents, it is assumed that they can play a major role in promoting the erosion of the banks of the tidal channels. Their effect is then initially neglected since the focus i on the salt marsh bank facing large mudflats.

The processes associated with the different types and locations of wave breaking relative to the scarp and the interaction of the swash with the scarp toe won't be explicitly addressed in the present work. This choice is justified by the fact that this kind of analysis would require a really detailed study of the flow field including the use phase-resolving models and it would excessively enlarge the work. For this reason these processes are implicitly accounted in the description of the flow field through a phase-averaging model.

[2]www.openfoam.org

2.2.2 Sediment transport of sand-mud mixtures

Changes in the morphology of salt marsh boundaries are induced by the transport of the sediment due to flow and gravity. Generally, salt marshes are characterized by cohesive sediment mixtures where sand ($0.063 < d_{50} < 2$ mm), silt ($0.004 < d_{50} < 0.063$ mm) and clay ($d_{50} < 0.004$ mm) are distributed in variable fractions [*Allen*, 1989; *Wilson* and *Allison*, 2008; *Amos* et al., 2010].

Incipient motion and transport of sand [*Shields*, 1936; *Yalin*, 1972] is widely reported in literature and several formulations for bed-load q_b [*Van Rijn*, 1984a; *Parker*, 1990], suspended load q_s [*Bagnold*, 1966; *Van Rijn*, 1984b] and total load $q_t = q_b + q_s$ [*Ackers* and *White*, 1973; *Soulsby*, 1997] have been proposed. A comprehensive review book on the mechanics of sand transport has been published by *Van Rijn* [1993].

Cohesive sediment erosion E and deposition D are generally described by the formulation proposed by *Partheniades* [1965] and *Krone* [1962], and a more detailed description of cohesive and fine sediment dynamics can be found in *McAnally* and *Mehta* [2003] and *Winterwerp* and *Van Kesteren* [2004]. More recently, attentions have been devoted to the interaction of sand and mud [*Mitchener* and *Torfs*, 1996; *Van Ledden*, 2003; *Van Ledden* et al., 2004; *Jacobs* et al., 2011] also with reference to tidal environments [*Waeles* et al., 2007; *Le Hir* et al., 2011].

In tidal environments, surface erosion strongly depends on the interaction between sand and mud (i.e. a mixture of silt and clay). Sand-mud mixtures are generally characterized by fine sediment fractions and are modelled by the coupling of erosion and deposition formulations, the advection-diffusion equation and the Exner equation. Generally, the ratio between clay and and silt is fairly constant in tidal environments and the two fractions can be combined in a single class called mud [*Flemming*, 2000]. Consequently, the soil composition can be identified by a sand fraction (p_s) and a mud fraction (p_m) in terms of mass, such that $p_m + p_s = 1$. Since the cohesive behaviour of sediments depends on the clay content [*Raudkivi*, 1990], it is possible to define a critical mud fraction, $p_{m,cr}$, as a threshold between the cohesive and non-cohesive regime of the mixture. *Van Ledden* [2003] proposed to determine the erosion rates for mud and sand differently, based on the value of p_m with respect to $p_{m,cr}$. In cohesive regime the erosion rate is controlled by the mud fraction and sand is eroded proportionally to the mud, whereas in non-cohesive regime it is the mud to be easily washed away with sand [*Murray*, 1977; *Mitchener* and *Torfs*, 1996]. In the following, a generalization of the erosion formulation proposed by *Van Ledden* [2003] is described:

$$E = M(p_m) \cdot T[\tau_{cr}(p_m)] \tag{2.6}$$

where M is an erosion parameter depending on the relative sand-mud content and T is a dimensionless transport parameter which may be determined in different ways in case p_m is higher or lower than $p_{m,cr}$. A general formulation for transport parameter is:

$$T = \left(\frac{\tau_b}{\tau_{cr}(p_m)} - 1\right) H_f \left(\frac{\tau_b}{\tau_{cr}(p_m)} - 1\right) \tag{2.7}$$

in which τ_b represent the bottom shear stress, H_f is the Heaviside function[3] and the critical shear stress τ_{cr} is based on different formulations for the cohesive and non-cohesive regime.

Deposition occurs differently for sand and mud. Sand grains settle without mutual interactions at velocity w_s dependent on the grain size and the viscosity of the fluid [*Van Rijn*, 1993]. On the other hand, the settling velocity of cohesive sediment is affected by the sediment concentration. At high concentration fine sediment may flocculate forming flocs of larger dimension and, increasing the mud concentrations (higher than 2 g/l), the deposition process is hindered [*Winterwerp*, 2002; *Winterwerp* and *Van Kesteren*, 2004]. For mud deposition, the formulation proposed by *Krone* [1962] considers a critical shear stress $\tau_{cr,d}$ (generally lower than the critical shear stress for erosion) over which settling does not occur. Nevertheless, such a paradigm of the mutually exclusive erosion and deposition is still debated and *Winterwerp* and *Van Kesteren* [2004] proposed to determine the deposition flux as:

$$D = C_b w_{s,f} \tag{2.8}$$

where C_b is the near bed sediment concentration and $w_{s,f}$ is a settling velocity depending on the flocculation process. For mixtures, sand and mud interact during settling when mud concentration is higher than the "gel point concentration" that is around 30–180 mg/l [*Winterwerp*, 1999].

Once sediment are set in motion, the advection-diffusion equation in two dimensions is usually employed to describe the time evolution of the depth-averaged sediment concentration C for a generic fraction [*Galappatti*, 1983]:

$$\frac{\partial hC}{\partial t} + \nabla \cdot (hC\mathbf{v}) - \nabla \cdot \epsilon_h \nabla(hC) = E - D \tag{2.9}$$

in which ϵ_h is the sediment horizontal dispersion coefficient.

Bed level changes z_b are modelled by means of the Exner equation [*Exner*, 1920; *Paola* and *Voller*, 2005]:

$$(1 - n_p)\frac{\partial z_b}{\partial t} + \nabla \cdot \mathbf{q_b} = E - D \tag{2.10}$$

where $\mathbf{q_b} = [q_{b,x}, q_{b,y}]^T$ is the bed-load transport flux and n_p is the sediment bed porosity (assumed constant).

[3] $H_f[f(x)] = 1$ if $f(x) \geq 0$; $H_f[f(x)] = 0$ if $f(x) < 0$.

If more than one sediment typology is present in the bed, its composition changes due to the interaction of multiple fractions. In order to describe the process, *Hirano* [1971] introduced the concept of “mixing layer”. It is a layer of finite depth at the interface between the bed and the fluid where a certain number of sediment fractions are instantaneously and completely mixed. A sublayer with a proper sediment composition is located below the mixing layer. The exchange of sediment occurs between the water column and the mixing layer and between the mixing layer an the underlying sublayer. The model has been improved by introducing more layers in the bed [*Ribberink*, 1987] in order to account for bed stratification, or by considering the bed composition as a continuous function of the vertical coordinate originating at the bed surface [*Armanini*, 1995], leading to the possibility of variation in bed composition at infinitively small distance from the bed surface. *Parker* et al. [2000] substituted the bed elevation and the erosion and deposition fluxes with probability density functions in order to remove the restriction of discrete layers, at the cost of more needed information on the introduced characteristics of the probabilistic functions.

2.2.3 Mass failures

Mass failures are episodic changes in the morphology of banks or cliffs in rivers, estuaries or coasts [*Allen*, 1989; *Selby*, 1993]. Their description is based on the equilibrium balance between the driving forces such as gravity and flow, which may cause the failure, and the resisting forces such as soil shear strength (σ_s) and root tensile strength (t_r), counteracting the mass wasting [*Thorne* and *Tovey*, 1981; *Van Eerdt*, 1985a; *Darby* et al., 2000].

The lithology of the marsh, together with the root-mat due to the presence of vegetation, can induce specific retreat mechanisms. Muddy sediments yield tall cliffs subject to toppling failure or sliding (Figure 2.4 a, b) due to the formation of tension cracks [*Allen*, 1989], which can form as a consequence of the shrinkage of the material during the warm season [*Morris* et al., 1992], or for to the accumulation of shear and volumetric deformation induced by cyclic oscillation of effective stresses due to the tidal excursion [*Cola* et al., 2008]. Once cracks are formed, they can widen during the ebb tide when the presence of water in the crack, filled at the high tide, induces an additional pressure leading to an overall trust directed shoreward [*Francalanci* et al., 2013].

Sandy marshes are characterized by a dense root-mat, which strengthens the upper part of the bank. In this case, most of the failure modes are of cantilever type because of the higher erosion below the root-mat (Figure 2.4 c) induced by waves or currents [*Allen*, 1989].

Cantilever type failures have been described mathematically by *Thorne* and *Tovey* [1981] and *Van Eerdt* [1985a]. The failure of the overhanging block of soil occurs once the scour at the bank toe exceeds a limiting value, and in the formulation, also the tensile strength of the root-mat is accounted for. Such

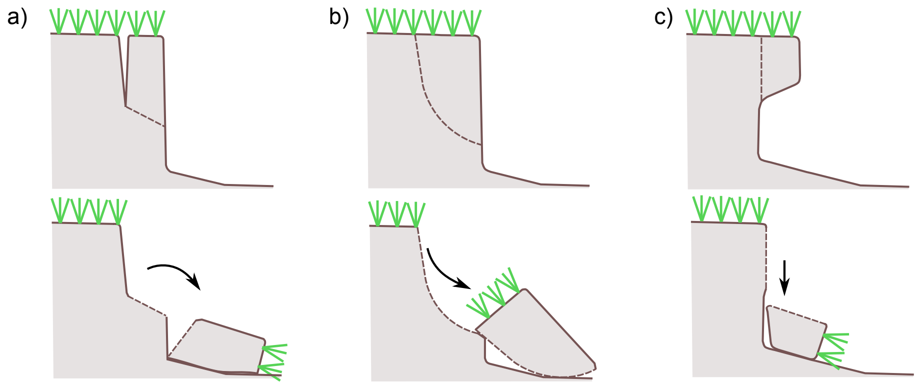

Figure 2.4: Mass failure modes related to salt marsh banks. a) Toppling failure. b) Rotational sliding. c) Cantilever failure.

a model has been employed by *Gabet* [1998] to quantify the lateral migration rate of a tidal channel in a salt marsh of the San Francisco Bay (US). Sliding failures are generally modelled with reference to the fluvial environment [*Darby* and *Thorne*, 1996; *Rinaldi* and *Casagli*, 1999], and they differ based on the geometry of the bank and the presence of tension cracks triggering the mass failure. Toppling failure are described analytically only with reference to rock mechanics [*Goodman* and *Bray*, 1976; *Amini* et al., 2009], whereas a qualitative description referred to salt marsh banks can be found in [*Thorne* and *Tovey*, 1981; *Allen*, 1989; *Francalanci* et al., 2013].

2.2.4 Effect of vegetation on waves and on marsh erosion

The presence of vegetation in marsh environments affects the trajectory of the system by modifying the flow field, due to the presence of the stems, and by providing a stabilization of the soil due to the effect of the roots [*Fagherazzi* et al., 2012]. Furthermore, organic production and sediment trapping contribute to the vertical dynamic of the marsh surface [*Morris* et al., 2002; *Marani* et al., 2010].

The effectiveness of marsh vegetation in dissipating wave energy has been tested by several authors through field measurements and laboratory experiments [*Möller* and *Spencer*, 2002; *Riffe* et al., 2011; *Jadhav* et al., 2013; *Möller* et al., 2014]. Presence of marsh vegetation considerably attenuates wave height even when stems are submerged, furthermore, although waves progressively damage the stems, the marsh substrate tends to remain stable and resistant to surface erosion [*Möller* et al., 2014].

In order to introduce the effect of vegetation in the modelling of wave propagation, *Mendez* and *Losada* [2004] added a dissipative term D_{veg} to the wave energy balance, that is the wave action balance (Equation 2.3) multiplied by a constant wave frequency σ. Such a term depends on the characteristics of the flow and of the plant species. Integrating over all directions the wave energy balance, it can be written as:

$$D_{veg} = -\rho C_{Dv} b_v N_v f(k, \sigma, h, \alpha h) H_{rms}^3 \tag{2.11}$$

where C_{Dv} is the "bulk drag coefficient", b_v is the stem width, N_v is the vegetation unit density, $H_{rms} = H_{m0}/\sqrt{2}$ is the root-mean-square wave height and f is a function of wave field characteristics (wave number k and frequency σ, and water depth h) and plant height αh. The value of C_{Dv} depends on the particular plant species and on the Keulegan-Carpenter number [*Keulegan* and *Carpenter*, 1958] and is therefore determined empirically. *Jadhav* et al. [2013] and *Ozeren* et al. [2013] determined C_{Dv} for *Spartina Alterniflora* that is a typical marsh plant. However, *Jadhav* et al. [2013] obtained the result using a slightly different formulation as compared to Equation 2.11. In a similar manner, the effect of vegetation in a phase-resolving wave model can be accounted for by adding a source term to the NSWE. Such an approach has been addressed by *Suzuki* [2011].

The effect of vegetation in enhancing soil strength, thus reducing erosion, is a widely accepted concept [*Gray*, *Leiser*, et al., 1982], specifically for salt marsh banks [*King* and *Lester*, 1995; *Chen* et al., 2012] and different types of root systems differ in their efficiency to reduce lateral cliff erosion [*Van Eerdt*, 1985b]. However, a debate on some issues still remains among researchers. *Feagin* et al. [2009] argued that salt marsh plants do not mitigate the total amount of erosion along the wetland edge and that the soil type is the primary variable that influences the lateral erosion rate. Plants may only indirectly influence erosion rate via modification of soil parameters. Nevertheless, they refer specifically to the process of detachment of particles from a volume of soil where roots are present and not to the role of vegetation in enhancing bank stability. Furthermore, *Howes* et al. [2010] showed that low salinity wetlands were preferentially eroded as compared to higher salinity wetlands during Hurricane Katrina and that this can be ascribed to geotechnical differences between the two cases caused by different plant characteristics. Recently, *Francalanci* et al. [2013] showed through laboratory experiments that the presence of vegetation can induce a delay in mass failure, but if its effect in decreasing total eroded material is low.

It is important to stress that salt marshes are subject both to shear stress erosion and wave impact erosion. To date no quantitative descriptions have been reported in the literature on the effect of vegetation on marsh edge erosion by frontal wave impact, except the approach proposed by *Mariotti* and *Fagherazzi* [2010]. On the other hand, the effect of the root-mat in decreasing shear erosion has been modelled with reference to sea dikes by *Van der Meer* et al. [2007] and *Tuan* and *Oumeraci* [2012]. They included the effect of grass root reinforcement of the clay cover of sea dikes by modifying a formulation prosed by *Mirtskhoulava* [1991]. The critical velocity for the erosion of grass-permeated soil is a function of undrained shear strength of the soil c_u, tensile strength of the roots t_r and root are ratio RAR defined as roots area per unit area.

2.2.5 Implications for this study

An accurate description of the flow field is necessary in order to quantify the hydrodynamic forcing at the marsh edge. However, using a highly detailed description of wave propagation, such a phase-resolving model, would lead to an excessive computational demand as the modelled time span reaches the duration of several days. Therefore, the wave action balance (Equation 2.3), in combination with the NSWE (Equations 2.1a, b, c) for the mean flow field are considered adequate to describe the hydrodynamics prevailing at the marsh boundary.

Regarding the morphodynamics processes and since salt marshes are characterized by a mixture of cohesive and non-cohesive sediment, the modelling framework proposed by *Van Ledden* [2003] is a good starting point to possibly model sediment erosion, transport and deposition, coupled to the mixing-layer concept proposed by *Hirano* [1971].

Vegetation plays a fundamental role in driving salt marsh evolution and several works [*Mendez* and *Losada*, 2004; *Jadhav* et al., 2013] provided a valuable base to consider its effect on surface wave propagation. Furthermore, the model to quantify the effect of roots in increasing the shear strength of soils protected by grass [*Tuan* and *Oumeraci*, 2012] can be easily extended to salt marsh vegetation by employing in the formulation the parameters of vegetation and root mat, associated to marsh plants (i.e. RAR, t_r).

Mathematical models to describe cantilever and sliding failures are available for both marsh banks [*Van Eerdt*, 1985a] and river banks [*Rinaldi* and *Casagli*, 1999]. However, toppling failures are described only qualitatively [*Allen*, 1989; *Francalanci* et al., 2013] and quantitative descriptions of such a failure mechanism is still missing.

2.3 Available models for wave-induced bank erosion

The erosion of the marsh edge has been studied by means of numerical, process-based models [*Van de Koppel* et al., 2005; *Mariotti* and *Fagherazzi*, 2010] and empirical models based on field measurements [*Schwimmer*, 2001; *Marani* et al., 2011]. Nevertheless, the description of the lateral bank retreat is rather simplified, being only a subset of larger numerical model systems describing the interaction of the marsh with the adjacent mudflat for long term forecast [*Mariotti* and *Fagherazzi*, 2010, 2013a], or focusing on the longitudinal (2D) evolution of the marsh boundaries [*Leonardi* and *Fagherazzi*, 2014]. With reference to empirical models, a relationship between wave energy flux W and lateral retreat R_{sc} is obtained for larger spatial (basin size) and temporal (years) scales.

In this section, a review of the available approaches employed to study cliff erosion by waves is reported, with a particular focus on salt marsh banks, characterized by mixtures of cohesive sediment and vegetated surface.

2.3.1 Bank retreat models

Several models are aimed at the description of sandy dunes attacked by waves by using both the equilibrium profile approach [*Larson* and *Kraus*, 1989; *Steetzel*, 1993] and the wave impact approach [*Nishi* and *Kraus*, 1996; *Larson* et al., 2004], including an attempt to also account for the effect of mass failures [*Erikson* et al., 2007].

For the 1D cross-shore models based on the equilibrium profile concept, the cross-shore sediment transport rate q_x is generally expressed by a relation of the type:

$$q_x = K_T(d_d - d_{d,eq}) \tag{2.12}$$

in which K_T is a transport parameter determined empirically, d_d is the wave energy dissipation rate and $d_{d,eq}$ is the wave energy dissipation rate for the dune profile at equilibrium.

The wave impact approach is based on the dependence of the eroded mass on the value of the force of the wave impacting the bank:

$$\Delta W_s = C_E F_w \tag{2.13}$$

where ΔW_s is the mass of eroded material per unit width, C_E is an empirically determined coefficient and F_w is the force exerted on the bank by wave impact. Such a model has been improved by the inclusion of the effect of mass failure events by *Erikson* et al. [2007]. The model focuses on the effect of waves on the scour at the bank toe, which shape is modelled analytically, whereas the hydrodynamic forcing involves only the description of the force exerted by the bore reaching the scarp of the bank.

Roelvink et al. [2009] developed the numerical model XBeach to describe the erosion of sand dunes and beaches induced by storm surges (Figure 2.5).

The model solves the wave action balance equation for short waves and the NSWE model, forced by radiation stresses determined from the former wave model, for the description of long waves. Sediment transport is modelled by an advection-diffusion equation where the source term is dependent on the difference between sediment concentration C and an equilibrium sediment concentration C_{eq} determined by the Soulsby-Van Rijn formulation [*Soulsby*, 1997]. Bed level is updated through Exner equation (Equation 2.10) and multiple sediment fractions are managed through the active layer concept [*Hirano*, 1971]. The effect of mass slumping is also included by means of an avalanching mechanism triggered when the scarp slope exceeds a specific threshold. Furthermore, the effect of vegetation on hydrodynamics is modelled by means of *Mendez* and

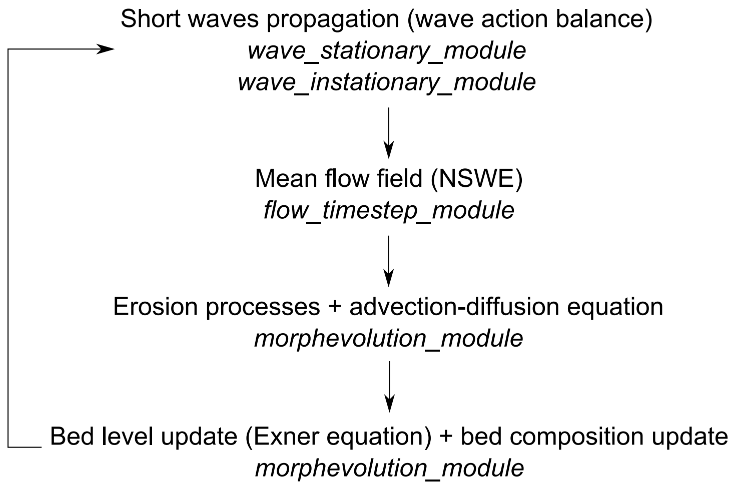

Figure 2.5: Structure of the XBeach model [*Roelvink* et al., 2009]

Losada [2004] formulation for a generic plant typology. In Figure 2.5 a sketch describing the structure of the XBeach numerical model is depicted.

Castedo et al. [2013] proposed a mathematical model to describe the recession of cohesive clay coasts, based on the previous studies of *Trenhaile* [2009], which also described mass failures. The function for the evolution of the bluff is of the type $x_b = x_b(z)$ instead of $z_b = z_b(x)$ (Figure 2.6 b), leading to the opportunity to model notches formation and development, at the cost of a less detailed description of wave forcing. The erosion rate in horizontal direction at the bank toe due to the impact of broken waves is:

$$E^*_{sc} = N_0 K_{bf} \left(s_f - s_{f,cr} \right) \tag{2.14}$$

in which E^*_{sc} is the horizontal retreat rate, expressed in [m/yr], N_0 is the number of waves in a year, K_{bf} is a calibration coefficient for wave erosion, s_f is the shear stress exerted by waves at the bluff toe and $s_{f,cr}$ is a threshold value of the shear stress for the onset of erosion.

With reference to salt marsh environment *Mariotti* and *Fagherazzi* [2010], starting from the study of *Van de Koppel* et al. [2005], described the evolution of the coupled system salt marsh-tidal flat, considering the dynamic of the vegetation and the effect of wave impact on the marsh bank. Short waves are described by means of an energy balance and the tidal wave is modelled in a quasi-static way, based on continuity equation. Sediment erosion and deposition are simulated through the Partheniades-Krone formulations [*Partheniades*, 1965], the advection-diffusion equation is devoted to the sediment transport and Exner equation to the bed level update. The erosion due to wave impact

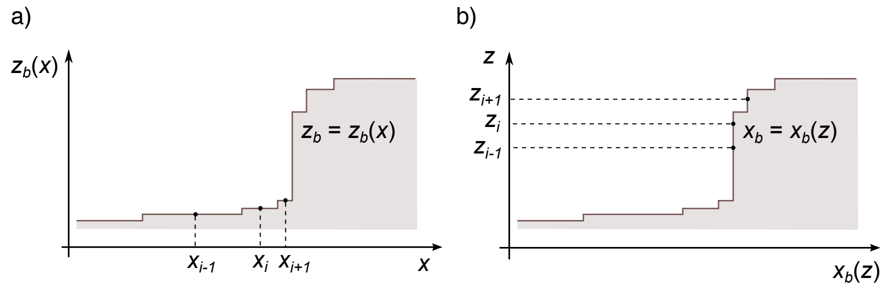

Figure 2.6: Approaches describing the evolution of the bank profile in the 1D model: a) Bed morphology z_b is a function of the horizontal coordinate x. b) Bed morphology x_b is a function of the vertical coordinate z.

is modelled as follow:

$$E_{sc} = \begin{cases} 0, & W < W_{cr} \\ m^*_{sc}\frac{(W-W_{cr})}{d_{sc}}, & W \geq W_{cr} \end{cases} \tag{2.15}$$

where E_{sc} is the erosion rate due to wave impact in vertical direction, m^*_{sc} is an erodibility coefficient, W is the wave energy flux, W_{cr} is a threshold value for the onset of erosion and d_{sc} is the length over which erosion has to be distributed. It is important to stress that the erosion due to wave impact is distributed into two cells at the shoreline and that this formulation produces a vertical erosion of a cell column rather than the horizontal migration of the scarp. Furthermore, the effect of mass failures is implicitly accounted for in the retreat rate. The effect of vegetation in mitigating erosion is accounted for by increasing the threshold value of W_{cr}:

$$W_{cr,v} = W_{cr}\left(1 + k_b\frac{B}{B_{max}}\right) \tag{2.16}$$

where $W_{cr,v}$ is the critical value in presence of vegetation, k_b is a dimensionless parameter accounting for the effectiveness of vegetation increasing the critical shear stress, B is the aboveground biomass and B_{max} is it maximum.

Above mentioned models are employed on large temporal scales [*Van de Koppel* et al., 2005; *Mariotti* and *Fagherazzi*, 2010; *Castedo* et al., 2013], except XBeach, which is usually used to describe the effect of single storm surges on sand dunes and beaches. In general, the bank retreat process is modelled using a linear relation between the forcing in terms of wave power, wave force or wave induced stress and the erosion rate by means of a calibration coefficient. The morphology is updated using two different types of functions describing the bed: $x_b = x_b(z)$ or $z_b = z_b(x)$. The former approach (Figure 2.6b), can better reproduce the horizontal retreat mechanism characterizing the scarp attacked by waves, but at the cost of a less detailed description of the hydrodynamics. The latter approach (Figure 2.6a) allows a more detailed description of the flow field, but tends to reduce the horizontal retreat to a vertical variation of the bed. Previous models consider a single sediment fraction (except for XBeach). Cohesive sediment are also not modelled and the effect of vegetation is included only in the model by *Mariotti* and *Fagherazzi* [2010], but the employed formulation is based on the assumption that the presence of vegetation linearly increases the critical shear stress of the soil.

Another aspect which is usually not considered in in modelling salt marsh bank retreat is related to the effect of wave reflection induced by the bank morphology. However, *Chellew* et al. [2011] showed through a simplified model that wave reflection may have a significant effect on the morphology of intertidal mudflats.

2.3.2 Relationships between wave power and erosion rate of marsh banks

Erosion of salt marsh edges has been also examined through field measurements, aimed at the determination of a relationship between the observed retreat rate R_{sc} and the estimated wave power W (Figure 2.7).

Schwimmer [2001] measured yearly the lateral erosion rates of some salt marshes located in Rehoboth Bay (Delaware, US) using an electronic measurement station, and determined a relationship with the local wave power estimated through wind, bathymetry and fetch data, using also field measurements provided by other authors [*Maurmeyer*, 1978; *Swisher*, 1982; *Phillips*, 1985; *French*, 1990].

Marani et al. [2011] obtained the theoretical form of the relationship between wave energy flux and retreat rate by means of the Buckingham's theorem of dimensional analysis [*Langhaar*, 1951]. They determined the erosion rates at several marshes in the Lagoon of Venice by means of aerial photographs and found a correlation with the wave energy flux obtained by wind, fetch and bathymetric data as input to a wave propagation model [*Carniello* et al., 2005; *Fagherazzi* et al., 2006].

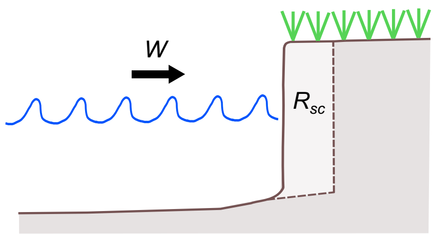

Figure 2.7: Wave energy flux W and volumetric erosion rate R_{sc} (principle sketch).

A difference between the two approaches, apart from the different technique adopted to measure erosion, is that *Schwimmer* [2001] considered a lateral erosion rate expressed in [m/yr], whereas *Marani* et al. [2011] a volumetric rate in [$m^3/(m \cdot yr)$], obtained by multiplying the lateral retreat by the local bank height b_h.

Recently, [*McLoughlin* et al., 2014] analyzed the relation between erosion rates of four salt marshes in the Virginia Coastal Bay (Virginia, US) obtained by aerial photographs, and wave power from a numerical model, SWAN [*Booij* et al., 1999], and the mathematical model proposed by *Young* and *Verhagen* [1996]. They found that the volumetric erosion rate [$m^3/m \cdot yr$] is more strongly correlated to the wave forcing as compared to the lateral retreat rate [m/yr]. Moreover, *Mariotti* and *Fagherazzi* [2013a] found an optimal value for the calibration coefficient relating wave power and marsh edge lateral retreat by calibrating their model using field data of basin width.

In order to compare results obtained by the authors, the different relationships are manipulated to get dimensionally congruent formulations with retreat rate R_{sc} expressed in [m^2/yr] and wave energy flux W in [W/m]. Formulation by *Marani* et al. [2011] remains unchanged. To convert the relation proposed by *Schwimmer* [2001] a regression analysis of the data used by the author applying the same relation is carried out. Since erosion rates are in [m/yr], and the height of the marsh bank lies between 30 and 90 cm, such a rate is multiplied by 0.6 m to obtain [m^2/yr] and the wave power is expressed in [W/m]. To recover the volumetric erosion rate in [$m^3/(m \cdot yr)$] from the relationship proposed by *Mariotti* and *Fagherazzi* [2013a], the value of lateral retreat in [m/yr] is multiplied by 1 m, assumed as reference bank height.

Results of the comparison are reported in Table 2.1. It is noticed that the coefficient linking W to R_{sc} strongly differs among the three studies even by factors of several orders of magnitude. This may be related to differences in reference environments, since the erosion rates are likely affected by the soil composition, by the health state of the vegetation and by the employed procedure to measure the erosion. In addition, different ways to retrieve erosion rates from the sampled eroded material can lead to strong differences in the results, depending on the sampling interval through which it is assumed that the erosive process occurred [*Singh* et al., 2009]. Furthermore, the approach used for calculating the wave energy flux can play a significant role, since detailed information about the local wave forcing close to the marsh edge are not available and different way to handle wind, fetch and bathymetric data may lead to different calculated wave energy fluxes as discussed by *McLoughlin* et al. [2014]. Another important aspect to be underlined is that *Schwimmer* [2001] also employed data from other studies [*Maurmeyer*, 1978; *Swisher*, 1982; *Phillips*, 1985; *French*, 1990] based on really large temporal scales (order of several decades) to recover its relationship, and this can partially reflect the difference of the erosion rate he retrieved with respect to the results of *Marani* et al. [2011] and *Mariotti* and *Fagherazzi* [2013a]. Nevertheless, a specific and clarifying explanation for the different outcomes obtained by the authors is still lacking.

The spatial and temporal scales analysed are quite large (in the order of the entire tidal basin and years or decades). This provides quite reliable results, but does not allow to identify the relative contribution of the processes (e.g. mass and surface erosion and mass failures) to bank retreat.

Table 2.1: Comparison among relationships for the three studies for erosion rate R_{sc} as a function of wave energy flux W reformulated in [m^3/(m·yr)] and [W/m] respectively.

Relation	Environment	Reference
$R_{sc} = 0.0364 \cdot W$	Lagoon of Venice	*Marani* et al. [2011]
$R_{sc} = 0.3320 \cdot 10^{-3} \cdot W$	Rehoboth Bay	*Schwimmer* [2001]
$R_{sc} = 0.1000 \cdot W$	Mid Atlantic Coast	*Mariotti* and *Fagherazzi* [2013a]

In previous works wave climate was always estimated by means of numerical or mathematical models. Measurements of wave climate in front of a marsh bank are limited and available data are reported in the literature with different objectives in the search for a relation W versus R_{sc}. *Möller* et al. [1999], *Möller* [2006] and *Jadhav* et al. [2013] studied the effect of marsh vegetation on wave energy dissipation. *Callaghan* et al. [2010] identified the relative importance of waves and tidal currents in shaping salt marsh morphology in relation to induced shear stress, *Priestas* and *Fagherazzi* [2011] analysed wave transformation over wave-cut gullies, whereas *Houser* [2010] tried to distinguish the effect of wind and ship-induced waves on salt marsh retreat. The latter found a positive correlation between the cumulative wave force expressed in [kg/m] and the marsh retreat [m]. He concluded that for the analysed area (Port of Savannah, Georgia), wind-generated waves are mainly responsible for the marsh retreat.

2.3.3 Implications for this study

Several models are available to describe the effect of waves on bank erosion, both for cohesive [*Trenhaile*, 2009; *Castedo* et al., 2013] and non-cohesive cliffs [*Larson* and *Kraus*, 1989; *Erikson* et al., 2007; *Roelvink* et al., 2009]. Numerical models related to salt marsh edges account for the main processes involved but are focused on long time and large spatial scales [*Mariotti* and *Fagherazzi*, 2010, 2013a; *Leonardi* and *Fagherazzi*, 2014]. A process based numerical model able to describe the erosion of the marsh boundary at short time scale (order of several storm surges or months) is not yet available. Furthermore, a sensitivity study on the relative contributions of the main parameters to marsh bank retreat, such as bank composition and vegetation characteristics would be particularly useful in order to better identify the research priorities towards an improved understanding of the underlying processes and enhanced model capabilities. Such a process-based model may preferrably be built within the XBeach model by implementing the behaviour of sand-mud mixtures, the effect of specific marsh vegetation on hydrodynamics and soil resistance as well as the contribution of wave impact erosion to marsh bank retreat.

The available relationships to quantify the erosion rate as a function of wave forcing are based on field measurements carried out over large time span (years or decades) which do not allow to identify the different contributions of surface erosion and mass failures to bank retreat [*Schwimmer*, 2001; *Marani* et al., 2011; *McLoughlin* et al., 2014]. Furthermore, the used wave forcing was not based on measurements or reliable detailed approaches for the assessment of the local wave climate, leading to large uncertainties in the evaluation of the wave forcing striking the bank. A more detailed study at shorter time scales (months) would be required in order to investigate more accurately the retreat mechanism involving marsh edges.

2.4 Specification of objectives and methodologies

In this section, the objectives and methodologies outlined in the first chapter are specified more precisely. They are based on the results of the review and analysis of the current knowledge and models related to the lateral retreat of marsh banks mainly induced by wind-generated waves.

2.4.1 Objectives

The boundaries of the salt marshes are subject to lateral migration due to the effect of surface waves. The main purpose of this study is therefore to improve the knowledge and modelling of the processes and mechanisms underlying marsh bank erosion and retreat under wave forcing. More specifically three objectives are identified.

- Development of a mathematical model to describe toppling failures, mainly based on the knowledge and data gained from laboratory experiments carried out previously [*Francalanci* et al., 2013].
- Planning and implementation of field measurements to develop a relationship between wave energy flux and marsh bank erosion rate at the time scale of months, and to identify the relative importance of continuous erosion and mass failures.
- Development and validation of a numerical model based within the existing XBeach model system [*Roelvink* et al., 2009] to describe the lateral retreat of mixed sediment banks covered by vegetation, forced by wind-generated waves modulated by the tide.

2.4.2 Methodologies

This research study can be structured in three principal parts, each being aimed at the achievement of one of the objectives specified in the previous section.

The development of the mathematical model to describe the toppling failure induced by wind waves should be mainly based on the results of a previously performed laboratory study. Two physical models of a salt marsh bank, one with and one without vegetation, were built in a wave flume and subject to irregular waves modulated by tide. The experimental setup, the analysis of the results and a detailed description of the observed processes are reported by *Francalanci* et al. [2013] and by *Bendoni* [2011, in italian]. The prospective mathematical model should describe the mass failures observed during the experiments. A block of soil prone to failure, identified by the presence of a tension crack, is considered attached to the underlying layer by a system of spring ad dashpot in order to reproduce the viscoelastic behaviour of the cohesive matrix. It behaves like a dynamic system subject to the time dependent forcing of surface waves. Mass failure occurs once the tensile strength of the soil is exceeded in at least one location over the failure surface. Wave climate and the dimensions of the blocks were measured during the experiments. The prospective model will be validated against experimental results with a particular focus the capability of the model to identify the wave group responsible for the mass failure.

The field measurements are carried out at a salt marsh of the Venice Lagoon. Measurements of erosion are obtained monthly by means of erosion pins located horizontally at different positions on the marsh boundary. Wave climate is measured during three storm surges through pressure transducers located close to the bank edge. Wave height is obtained from pressure head spectra by means of a transfer function based on linear wave theory [*Jones* and *Monismith*, 2007]. Direct measurements of wave climate are used to calibrate a model for the forecast of wave height from wind, bathymetry and fetch data [*Young* and *Verhagen*, 1996; *Breugem* and *Holthuijsen*, 2007] in order to avoid frequent local wave climate measurements. Wind and water level data are collected hourly from several measurement stations located in the Lagoon of Venice. A relationship should be developed between the wave energy flux and the erosion rate with or without consideration of mass failures. Furthermore, a possible interpretation of the role of mass failures on cumulative bank retreat will be proposed. The campaign started in November 2013 and is still ongoing. In the present work results until April 2015 are reported.

A process-based 1D numerical model is to be developed starting from XBeach [*Roelvink* et al., 2009]. Several processes are added to the model system.

– Interaction of sand and mud for cohesive and non-cohesive mixtures mainly based on the study by *Van Ledden* [2003].

– Effect of specific salt marsh vegetation on waves propagation and on soil erosion using results from *Mendez* and *Losada* [2004] and *Jadhav* et al. [2013].

– Wave impact erosion based on the study of *Mariotti* and *Fagherazzi* [2010] and a novel approach to describe the consequent horizontal migration of the marsh edge aimed at the possibility to form vertical scarp.

- Effect of the partially reflected wave pattern induced by the bank morphology inspired by the study of *Xie* [1981].

The implemented process are summarized in Figure 5.1 together with the names of the modules containing the related numerical code.

Chapter 3

Mathematical Modelling of Toppling Failure Induced by Wind Waves

In this chapter, the mathematical model of the mass failure of toppling typology due to wind-induced water waves is presented. The model is developed based on (i) the results of a previous experimental study, aimed at the observation of salt marsh bank retreat due to wind waves and tide [*Bendoni*, 2011; *Francalanci* et al., 2013], and (ii) a new experimental study, to measure the wave thrust on the marsh surface and the pressure wave propagation within the soil.

First, a summary of the previous study is provided. Second, the setup for the new experiments is described. Third, the mathematical model for the toppling failure is developed. Then, experimental results are shown and the model is run for some test cases. Finally, a critical discussion is carried out and conclusions are drawn.

In order to better identify the part of the research activities before and during the PhD study, a summary of the laboratory studies and further activities is reported in Figure 3.1.

3.1 Summary of previous experimental study

The previous experimental activity was carried out in the Hydraulic Laboratory of the Department of Civil and Environmental Engineering of the University of Florence. A more detailed description of the experimental setup and procedure can be found in *Bendoni* [2011] and *Francalanci* et al. [2013].

Two physical models of a salt marsh bank, one with vegetation and one without vegetation, were built inside a 50 m long, 0.8 m wide and 0.8 m deep wave flume. In order to reduce the quantity of material required to build the models, the wave flume was narrowed to 0.5 m for about 8 m, in front of the

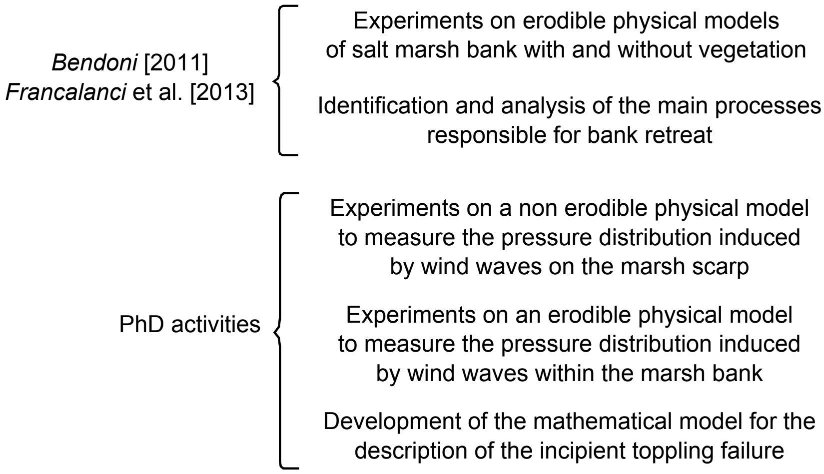

Figure 3.1: Summary of the research activities carried out before and during the PhD study.

physical models. Such a length was considered sufficient to allow incoming waves to "adapt" to the narrowed width. Wave climate was monitored by means of five resistive wave gauges: two close to the wave maker and three in the narrowed part of the flume, spaced 25 cm to better characterize wave climate close to the bank and to determine the reflected waves.

Waves were generated at one end of the flume through a hydraulic piston-type wave maker driven by a signal obtained from the deterministic spectral amplitude technique [*Hughes*, 1993], whereas the physical models of the salt marsh bank were built at the opposite side. The bank was 0.6 m high, 0.5 m wide and roughly 1 m long. The dimensions are comparable to those observed for several marshes in the Lagoon of Venice in scale 1:1.

Four experiments were carried out on each physical model of the salt marsh bank, one with and the other without vegetation on the top. The series of four experiments consisted of:

– variation of water level at the high tide phase;

– variation of water level at the low tide phase;

– variation of water level at the high tide phase superimposed to wave forcing;

– variation of water level at the low tide phase superimposed to wave forcing.

The analysis of the experimental results allowed to identify the main processes responsible of bank retreat. The effect of tidal wave oscillation promoted the formation and widening of tension cracks parallel to the bank edge, both in case of vegetated and non-vegetated bank. The presence of tension cracks led to an unstable bank configuration, triggering mass failure events such as toppling failures: the waves induced a "shaking" on the block identified by the presence of a crack until the block overturned and slumped in front of the bank. For this type of failure, the tensile strength of the soil, rather than the shear strength, seems to be exceeded. Indeed, wave forcing transferred a torque on the failure surface, inducing alternating compression and traction of the soil fibres until the tensile strength of the soil was reached. Furthermore, some failure events of sliding type were observed, but less frequently.

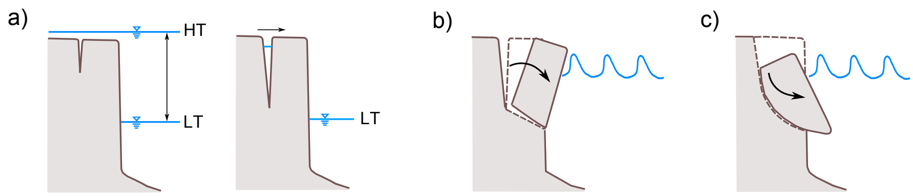

Figure 3.2: Sketch of the main processes observed during the experiments. a) Formation and widening of tension cracks due to tidal excursion (HT: high tide, LT: low tide); b) Toppling failure; c) Sliding failure.

A sketch of the observed processes is reported in Figure 3.2 (after *Francalanci* et al. [2013]). Mass failures occurred during the first part of the experiments which was characterized by a higher erosion rate. Then, erosion rates decreased and continuous mass and surface erosion [*Winterwerp* and *Van Kesteren*, 2004] were observed throughout the whole experiments both in vegetated and non-vegetated case. The presence of vegetation led to a delay in the mass failure of vegetated clods, and it is possible to argue that roots played a stabilizing role by anchoring the block of soil to the underlying layer.

Qualitative information about the failure mechanism can be obtained by the experimental observations. If tension cracks are present in salt marsh bank, several forces act on the overhanging unstable block: the weight of the block itself, the force due to the pressure distribution of water in front of the bank and possibly inside the crack, the force due to the cohesion of the soil and the time varying force induced by waves. Their combination, together with the dimensions of the block can lead to stable or unstable conditions. This framework will be employed to derive a mathematical model describing the incipient failure of a block of soil subject to hydrodynamic forcing.

3.2 Material and methods

Two additional sets of experiments were carried out within the present PhD study, in order to measure the pressure field induced by waves on the marsh surface and within the bank. The experimental setup for the wave flume and the measuring instruments are the same as those employed by *Francalanci* et al.

[2013] (Figure 3.3a).

For both sets of experiments, the effect of tide was reproduced by assuming a semi-diurnal tide with an approximate period of 12 hours. Based on field observations and due to flume constraints, the tidal excursion was set equal to 30 cm around the average water level in the channel, imposed at 47 cm from the bottom (in this chapter, water level η and water depth h will be used indifferently since the reference frame for the water level is the bank toe, which corresponds to the bottom of the wave flume). From an operational point of view it was not possible to continuously change the water level in the channel to reproduce the tidal wave. Four different tidal levels were then selected to reproduce the tide. Two water levels equal to 54 and 62 cm from the bottom corresponded to the high tide phase (HT), and two water levels equal to 40 and 32 cm from the bottom to the low tide phase (LT).

Wave forcing was reproduced according to field data measured at a wave measurement station in the Lagoon of Venice [see *Francalanci* et al., 2013]. The JONSWAP spectrum [*Hasselmann* et al., 1973] employed to reproduce the wave climate was characterized by: a significant wave height H_{m0} of 0.1 m, a peak period T_p of 1.4 s and a peak enhancement factor $\gamma = 2$.

For the first test series, the new physical model was made by rigid impermeable material (plywood) since the permeability of the soil in the reference environment was very low (ranging from 10^{-8} to 10^{-6} m/s) [*Cola* et al., 2008; *Francalanci* et al., 2013]. Several pressure transducers (PTs) Series 46x, produced by Keller Instruments (resolution 0.1 mbar, range of measurement 0.0–100.0 mbar) were located on the model in two different configurations based on the high tide (HT) or low tide (LT) experiments (Figure 3.3b). The former consisted of two experiments of 5 minutes duration, each with water depth in front of the model set at 54 and 62 cm. The latter consisted of two experiments of the same duration with water depth set at 32 and 40 cm. Pressure was continuously measured at a sampling rate of 100 Hz.

The second set of experiments were aimed at the study of pressure wave propagation through the soil for an erodible physical model. The salt marsh bank was built with the same material and the same procedures employed by *Francalanci* et al. [2013]. The material (42% mud, 17% clay, 5% organic matter and remaining part very fine sand) was collected in a salt marsh of the Lagoon of Venice, near Campalto. The model was gradually built by creating a series of 10 cm thick layers up to the height of 60 cm. A static load was applied to each layer for at least 24 hours in order to consolidate the soil. Six PTs (previously employed for the first set of experiments) were located inside the bank to measure the wave induced pressure (Figure 3.3c).

Five different experiments were carried out on the erodible model. In all cases water level in the channel was set to the desired value before starting with wave generation. For the first four experiments, water level was set respectively equal to 54 cm, 62 cm, 32 cm and 40 cm; experiments lasted 5 minutes each.

The fifth experiment was different from the previous four and was devoted to the measurement of wave induced pressure during the failure process and the observation of any further failure mechanism. Water level was set to 54 cm and the experiment was divided in two parts of 5 and 25 minutes of continuous wave forcing. A summary of the experiments carried out is reported in Table 3.1.

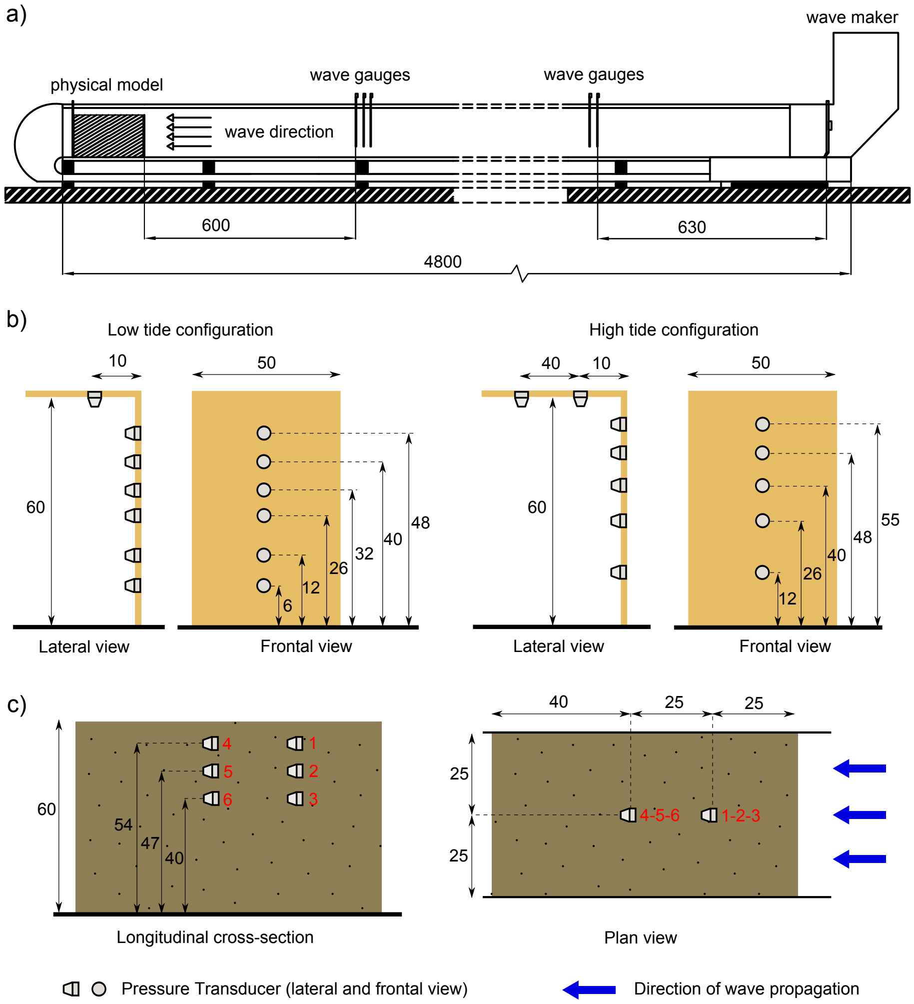

Figure 3.3: Experimental setup for: a) Wave flume employed for the experiments with the location of wave gauges; b) measurement of wave induced pressure on the marsh surface; c) measurement of wave induced pressure inside the salt marsh bank. All dimensions in cm.

Table 3.1: Summary of the experiments carried out and respective labels to refer to them in the text. h is the mean water depth in the flume expressed in cm.

Experiment Typology	Label	Tide	h
Pressure on marsh surface (rigid model)	*Psurf32*	Low	32
	Psurf40	Low	40
	Psurf54	High	54
	Psurf62	High	62
Pressure inside the bank (erodible model)	*Pinbank54*	Unique	54
	Pinbank62	Unique	62
	Pinbank32	Unique	32
	Pinbank40	Unique	40
	Pfailbank54	Unique	54

3.3 Toppling failure model formulation

3.3.1 Simplified scheme for toppling failure

In order to develop a new formulation for the modelling of toppling failures, a cross section of the bank in the x-z vertical plane, and an approximately prismatic block of soil are considered. The block extends for a given width L_b along the longitudinal coordinate y.

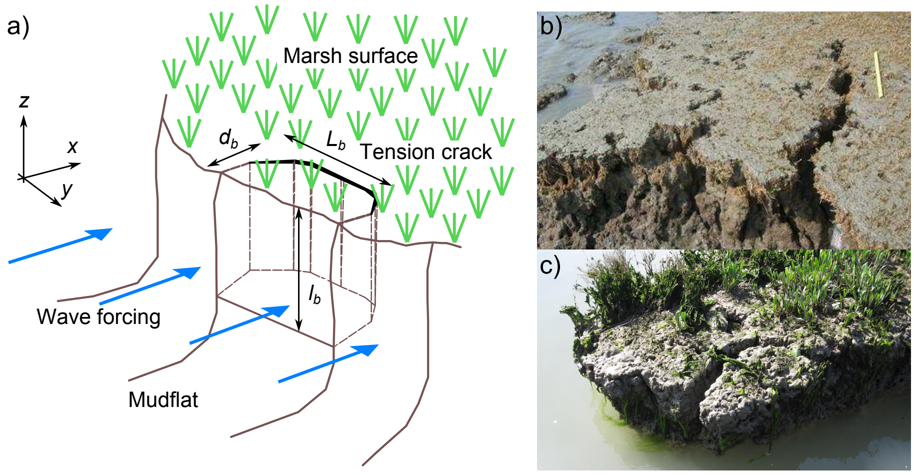

Figure 3.4: a) Sketch representing an unstable bank configuration in which a block, subject to wave forcing, is identified by the presence of a tension crack. The thick black line identifies the geometry of the crack; dotted brown lines identify the hypothesized geometry of the block. b) and c) Pictures of tension cracks on the surface of salt marshes (Figure 3.4b courtesy of G. Mariotti).

A sketch of the scheme is reported in Figure 3.4a. In Figure 3.4b and 3.4c,

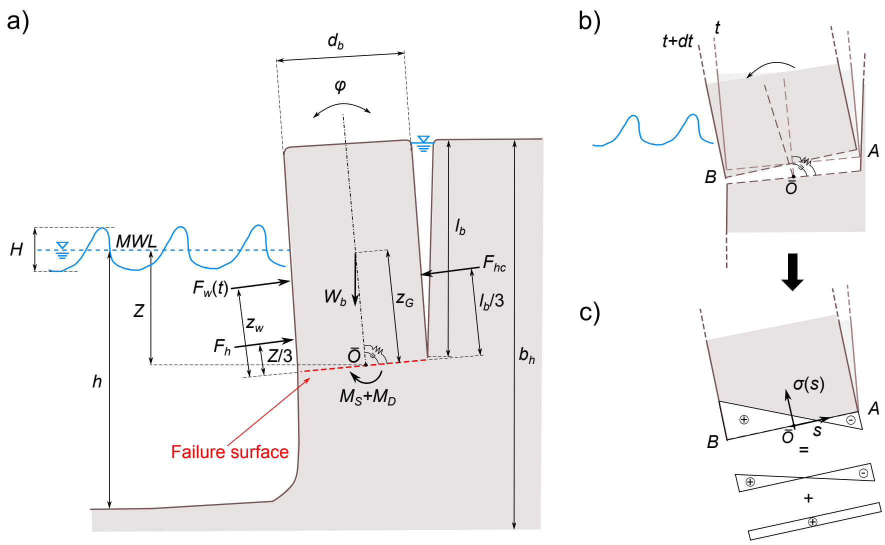

Figure 3.5: a) Sketch of the cross section of the system upon which the dynamic model is based. The extension of the system in the orthogonal direction to x-z plane is determined by the width of the block L_b. b) and c) Schematic of the failure surface with the stress distribution induced by a small clockwise rotation of the block from its equilibrium configuration.

two blocks on the verge of failure observed in the field are reported. The block can be subject to wave forcing and is modelled as a rigid body of mass m_b, attached to the underlying soil layer by a system composed by a spring and a dashpot and identified by the presence of a vertical tension crack (Figure 3.5a and 3.5b). The width of the block, the location and depth of the crack are determined from the experimental results. The soil is considered homogeneous and isotropic with a viscoelastic behaviour and its dynamic is described by a Kelvin-Voigt model [*Malkin* and *Isayev*, 2006]. The soil matrix is assumed impermeable with reference to the time scales involved in the process, indeed, permeability k_p ranges from 10^{-8} to 10^{-6} m/s for soil composing the salt marshes of the Lagoon of Venice [*Cola* et al., 2008]. The modelled system behaves dynamically as a consequence of the external forces. Hydrodynamic thrust due to wave impact, hydrostatic thrust and gravity induce small oscillations of the block of an angle φ (positive clockwise) around an equilibrium configuration. The lateral forces acting on the side vertical surfaces of the block are neglected. However, in the field the shear resistance on the lateral sides of the block is present, even if the block itself may have a less regular shape. This assumption is in agreement with the present experimental framework, where the friction of the lateral wall, made of glass, can be neglected. For this reason it would be contradictory to add to the model something that is not possible to be validated. Next developments will also account for this aspect that likely tend to increase to resistance of the block against failure.

The criterion of failure is based on the exceed of the tensile strength of the material on at least one point of the failure surface. This implicitly assumes that the fracture instantaneously propagates along the partially reduced failure surface, which is hypothesized plane and tilted of a small angle φ_0 with respect to the horizontal direction. This assumption can be considered conservative with respect to the failure criterion since it neglects the residual resistance of the partialized section of the failure surface. However, a further improvement of the model would require to relax this assumption in order to check if the system is able to show a higher resistance against failure. The failure surface is located at a depth from the top of the bank equal to the depth of the tension crack l_b (Figure 3.4a and 3.5a). Its dimensions are assumed equal to the width L_b and length d_b of the block (Figure 3.4a). Mean water level MWL and mean sea level MSL are assumed to be the same since the effect of wave setup is neglected (Figure 3.5a). Finally, the tensile strength of the soil is assumed equal to the cohesion c_u measured by a consolidated undrained triaxial test, and ranged from 5 to 20 kPa for the samples collected in the Lagoon of Venice [*Francalanci* et al., 2013].

The initial configuration without waves is considered to be equilibrated and characterized by an angle $\varphi_0 + d\varphi$ with respect to the vertical direction. The small perturbation clockwise $d\varphi$ represents the rotation induced by the weight of the block itself and is proportional to φ_0. When waves act on the block, it is partially free to oscillate due to the soil at the base and the possible presence of water inside the crack. As a consequence, counter-clockwise rotations with respect to the initial configuration are not allowed.

The mass of the block m_b is determined through the height l_b, the length d_b, the width L_b and the wet soil density ρ_s. Referred to the mean water level (MWL) h is the water depth and Z is the elevation of the rotating point $\bar{O}$ (Figure 3.5a).

The failure surface remains unchanged when the block oscillates, it means the point $\bar{O}$ is fixed and located at $d_b/2$, even if the neutral axis would change its position during the rotation due to the variation of the ratio M_{tot}/W_b (see Equation 3.5). Furthermore, the coefficients of the model are determined once at the beginning of the simulation (see the values of c_d and k_{sp} in Appendix A). This choice is made in order to avoid to implement an iterative procedure to locate the position of the neutral axis at each time step. It is possible to argue that such assumption does not significantly influence the results since the new position of the point $\bar{O}$ seems to have a negligible effect on the calculation of M_{tot} (see Section 3.3.2 and Equation 3.4). Further developments of the model should verify the validity of this assumption.

The combining effect of the moments and the normal force due to the block weight induces a stress distribution on the failure surface as depicted in Figure 3.5b. Compression and tension stresses are respectively indicated with plus and minus sign.

3.3.2 The equation of motion

The governing equation for the rotation of the system is:

$$I_b \frac{d^2\varphi}{dt^2} = \sum_i M_i \tag{3.1}$$

where φ is the angle (positive clockwise) with reference to the equilibrium configuration, I_b is the moment of inertia of the block with respect to rotation point $\bar{O}$ (considering also the hydrodynamic mass contribution), and M_i is the i-th moment with respect to $\bar{O}$ due to the forces acting on the block.

The hydrodynamic mass for rotational motions, with reference to the base of the block, is estimated through [*Oumeraci* and *Kortenhaus*, 1994]:

$$m_{hr} = 0.218\rho L_b Z^2 \tag{3.2}$$

and such a term is included in the moment of inertia I_b:

$$I_b = m_b \left(\frac{l_b^2 + d_b^2}{12} \right) + (m_b + m_{hr}) \frac{l_b^2}{4}. \tag{3.3}$$

in which $m_b = \rho_s d_b l_b L_b$ is the block mass.

According to Figure 3.5a, soil elasticity is modelled through the reaction moment of the spring ($M_S = -k_{sp}\varphi$), and soil viscosity through the reaction moment of the dashpot ($M_D = -c_d \frac{d\varphi}{dt}$). k_{sp} and c_d are, respectively, the dynamical spring stiffness and the damping coefficient, both depending on forcing frequency (see Appendix A). $W_b = gm_b$ is the block weight, $F_h = \frac{1}{2} g\rho L_b Z^2$ is the hydrostatic force at elevation $Z/3$ due to water in front of the bank (Figure 3.5a), and $F_{hc} = \frac{1}{2} g\rho L_b l_b^{*2}$ is the hydrostatic force at elevation $l_b^*/3$ due to water possibly filling the crack (for small oscillation angle φ, $\cos(\varphi_0 + \varphi) \approx 1$). l_b^* represents the water depth in the crack, obtained by the product of the degree of filling of the crack and the crack depth l_b. The degree of filling is defined as the ratio between the water depth inside the crack and the depth of the crack. The wave-induced force F_w is located at elevation Z_w (see Figure 3.5a and next section). Replacing the forces and moments described above in Equation 3.1, and assuming small rotations ($\sin(\varphi_0 + \varphi) \approx \varphi_0 + \varphi$), it is possible to obtain:

$$I_b \frac{d^2\varphi}{dt^2} + c_d \frac{d\varphi}{dt} + k_{sp}\varphi = -F_h \frac{Z}{3} + F_{hc} \frac{l_b^*}{3} - F_w(t) Z_w(t) + W_b \frac{l_b}{2} (\varphi_0 + \varphi) \tag{3.4}$$

For small rotations, the direction of the force does not change with φ and thus remains horizontal. Equation 3.4 is converted to a set of two ordinary differential equations (Appendix A) and solved numerically using a fourth-order Runge-Kutta method with specific initial conditions for φ (solution of Equation 3.4 in case $F_w = 0$) and $d\varphi/dt = 0$.

To calculate the stress acting on the failure surface, for small deformations, a linear stress-strain relation is assumed with the same behaviour in compression and extension. The total reaction moment exerted on the failure surface is $M_{tot} = M_S + M_D$ and the normal force on it is directly given by the block weight W_b, since $\cos(\varphi_0 + \varphi) \approx 1$. Then, considering a reference system centred in the point $\bar{O}$, with the spatial coordinate s along the segment AB, positive from $\bar{O}$ to B (Figure 3.5b), the stress on the failure surface is:

$$\sigma_s(s) = \frac{M_{tot}}{I_s} s + \frac{W_b}{d_b L_b} \tag{3.5}$$

where $I_s = \frac{1}{12} d_b^3 L_b$ is the moment of inertia of the failure surface orthogonal to the x-z plane of the failure surface. It is also assumed that the failure criterion is only related to the tensile strength of the soil, since the shear strength of the material is unlikely exceeded due to positive values of σ_s.

3.3.3 Computation of the wave forcing

The value of the wave forcing $F_w(t)$ on the vertical face of the block is determined through Airy Linear Wave Theory [*Dean* and *Dalrymple*, 1991] and the application of a correction factor based on the results of the experiments carried out on the non-erodible physical model (*Psurf40* and *Psurf54*). For a given water depth h, water surface elevation η_i due to the incident wave component with period T of a regular wave train moving toward a vertical wall, $F_w(t)$ can easily be calculated. For irregular waves $F_w(t)$ can also be calculated using linear wave theory on every single wave identified by a zero up-crossing analysis [*Holthuijsen*, 2007]. The analysis considers a wave as the profile elevation between two consecutive upward crossing of the mean surface elevation. The wave height is the difference between the maximum and minimum value of the profile elevation associated to a specific wave. In the calculation of $F_w(t)$, the effect of wave reflection from the vertical face is not directly considered.

The temporal development of the vertical distribution of the wave-induced pressure is:

$$p_d(z, t) = \rho \cdot g \cdot K_p(z) \cdot \eta_i(t) \tag{3.6}$$

where $K_p(z)$ is the pressure response factor accounting for the dynamic component due to water particle acceleration and $\eta_i(t)$ is the water surface displacement at a given location x due to the incoming wave (see Section 3.4.1). Wave-induced force F_w is determined by integrating the hydrodynamic pressure $p_d(z)$ over the vertical column, i.e. from the bottom to the free surface, or to the upper limit of the bank in case of wave overtopping, and finally by multiplying the resulting force per unit width F_w^* by the width of the block L_b.

The elevation (Z_w) from the point $\bar{O}$ of the application of wave force $F_w(t)$

on the vertical face of the block is determined by:

$$Z_w(t) = Z + \frac{\int_{-Z}^{\eta_i(t)} z \cdot p_d(z,t)dz}{F_w^*(t)}. \tag{3.7}$$

3.4 Experimental results

The experimental results are divided in two parts: wave force on the surface of the rigid salt marsh bank model and wave pressure within the erodible salt marsh bank model.

3.4.1 Wave force on the surface of the rigid salt marsh bank model

Forces exerted by waves on the salt marsh bank surface can be estimated through the pressure measurements collected during the experimental study with the rigid model of a salt marsh bank (Figure 3.3b). For each water level, the force per unit width F_w^* is determined by assuming the measurement of each PT $p_{m,i}$ representative of the pressure exerted on a portion of the vertical surface ΔZ_i:

$$F_w^*(t) = \sum_{i=1}^{N_{PT}} p_{m,i}(t)\Delta Z_i \tag{3.8}$$

where N_{PT} is the number of pressure transducers placed on the bank and $\Delta Z_i = \frac{1}{2}(z_{i+1}^{PT} - z_{i-1}^{PT}); i = 2, .., N_{PT} - 1$, $\Delta Z_1 = \frac{1}{2}(z_1^{PT} + z_2^{PT})$ and $\Delta Z_{N_{PT}} = b_h - \frac{1}{2}(z_{N_{PT}}^{PT} + z_{N_{PT}-1}^{PT})$. z_i^{PT} is the elevation of the pressure transducer with respect to the bottom of the channel and b_h is the height of the bank.

In Figure 3.6 wave-induced forces per unit width on the vertical surface of the rigid salt marsh bank model are plotted against relative water depth h/b_h which represents each tested tidal level. Figure 3.6a reports the average maximum force $\bar{F}_{w,max}^*$ determined by averaging the maximum force associated to each wave, whereas Figure 3.6b shows the difference between the absolute maximum wave force $F_{w,max}^*$ and minimum wave force $F_{w,min}^*$ as well as the difference between $F_{w,max}^*$ and hydrostatic force F_{hydro}^* measured during each experiment. To identify each wave, a zero up-crossing analysis has been carried out on the time series F_w for each experiment.

It is possible to observe that the wave force tends to increase more slowly as the water level approaches the bank top ($h/b_h = 1$). Indeed, part of the wave propagates over the bank, without hitting its vertical face as shown through numerical simulations by *Tonelli* et al. [2010].

Obtained results are used to better estimate the wave forcing as input to the model for incipient toppling failures. The value of F_w is calculated applying a correction factor to the theoretical value of wave force F_t determined through linear wave theory [*Dean* and *Dalrymple*, 1991]. To separate the incident and

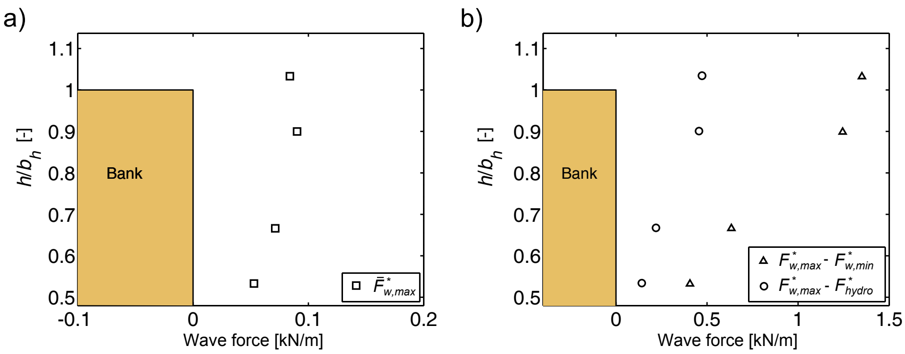

Figure 3.6: Wave-induced force per unit width on the vertical surface of the rigid salt marsh bank model. a) Average value of the maximum wave force (black square) associated to each wave for different water depths h (32 cm, 40 cm, 54 cm and 62 cm). b) Difference between absolute maximum and absolute minimum wave force during a single experiment (black triangle) and difference between absolute maximum wave force and hydrostatic force (black circle) during a single experiment for different water depths h (32 cm, 40 cm, 54 cm and 62 cm).

reflected wave component in time domain, a modified version of the method proposed by *Goda* and *Suzuki* [1976] has been implemented. First, the incident wave amplitude and phase, as a function of frequency, were determined by means of data collected by the three wave gauges located close to the physical model, considered in pairs. Then, the time series of the water displacement η_i, due to incident wave, was obtained as a sum of Fourier components. The value of F_t was determined by the integrating Equation 3.6 over the frontal surface of the physical model. To check the overlapping of F_t and $F_{wb} = F^*_w \cdot L_b$, a cross correlation analysis was carried out between the two series, resulting in a maximum value for the normalized cross correlation equal to 0.9. Then, a zero up-crossing analysis was carried out on F_t and F_{wb} and for each wave identified, the difference between maximum and minimum force was collected in two vectors, ΔF_t and ΔF_{wb}. These values, representing the magnitude of the wave force, were put in correlation and plotted in Figure 3.7.

The linear regression line between the two datasets was constrained to pass through the origin, giving the following equations:

$$\Delta F_{wb} = 1.66 \Delta F_t, \quad h = 54 \text{ cm}; \tag{3.9a}$$

$$\Delta F_{wb} = 1.80 \Delta F_t, \quad h = 40 \text{ cm}. \tag{3.9b}$$

Only experiments with mean water depth at 54 cm and 40 cm were considered for the previous analysis. Indeed, water depth of 32 cm does not allow waves to strike the upper part of the bank prone to mass failures. The correction factor applied to F_t was set equal to 1.75, which is closer to that obtained by the experiment at 40 cm water level. This is a more conservative choice with respect to 1.80, and it is more reliable since during the experiment at 54 cm water depth,

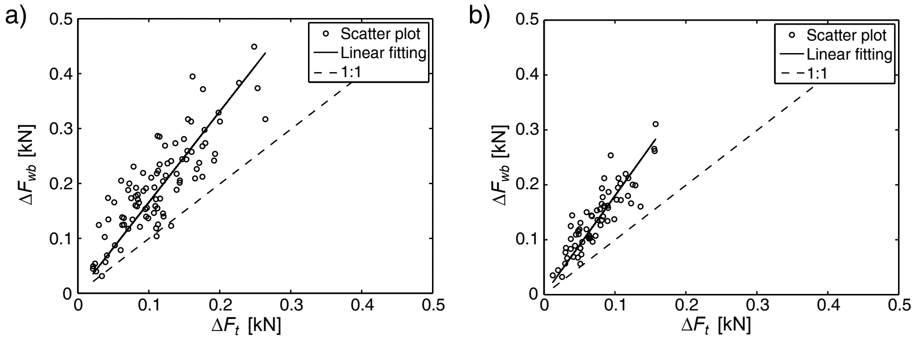

Figure 3.7: Scatter plot between ΔF_t and ΔF_{wb} (black circles), linear regression line (black line) and 1:1 line (black dashed line) for mean water depth in the channel equal to: a) 54 cm and b) 40 cm.

several waves overtopped the bank. It is important to stress that the correction factor equal to 1.75 was used for all the further calculations independently of the water depth h in the channel. Even if this is a simplification, the use of a constant value does not likely affect the results since the range of variation of such a facto is between 1.66 and 1.80.

The procedure to determine the time series as input for the model for toppling failure is summarized as follows:

- determination of incident wave component from measured water levels;
- computation of wave force F_t;
- application of the correction factor to F_t to obtain F_w and the lever arm Z_w (see Equations 3.4 and 3.7).

3.4.2 Wave pressure within the erodible salt marsh bank model and observed failure processes

The damping of the wave-induced pressure within the bank has been analysed by comparing the measurements collected by each pair of PTs located at the same depth from the top of the bank (Figure 3.3c).

The noise was removed from the measurements by a low-pass filtering procedure. The filtered time series corresponding to each pair of PTs located at the same elevation were analysed by a zero up-crossing procedure. The amplitude Δp associated to each pressure recorded by the PTs close to the marsh edge (PT number 1, 2 and 3) was compared to that of the same pressure wave travelling by the farther PTs (PT number 4, 5 and 6), Δp_d. The comparison was carried out between PTs located at the same depth.

In Figure 3.8, the results of the comparison between Δp and Δp_d for $h = 54$ cm are reported. Other results are shown in Appendix B. Results from the couple of PTs 1 and 4, located 54 cm above the bottom are not reported since PT 1 stopped functioning after 1 minute from the beginning of the experiment. The damping of the pressure wave is higher for the PTs located 47 cm from the bottom of the channel (PTs 2 and 5) with respect to those located at 40 cm from the bottom (PTs 3 and 6).

Afterwards, a spectral analysis through Welch method [*Welch*, 1967] was carried out for each pair of PTs in order to observe the pressure wave damping as a function of frequency. The spectrum of each pair of PTs is reported in Figure 3.9. The results from the spectral analysis are in agreement with the results of time domain analysis, indeed the damping of pressure waves appears to be much higher for pair PTs 2 and 5 located at 47 cm from the bottom of the channel than pair PTs 3 and 6 located at 40 cm.

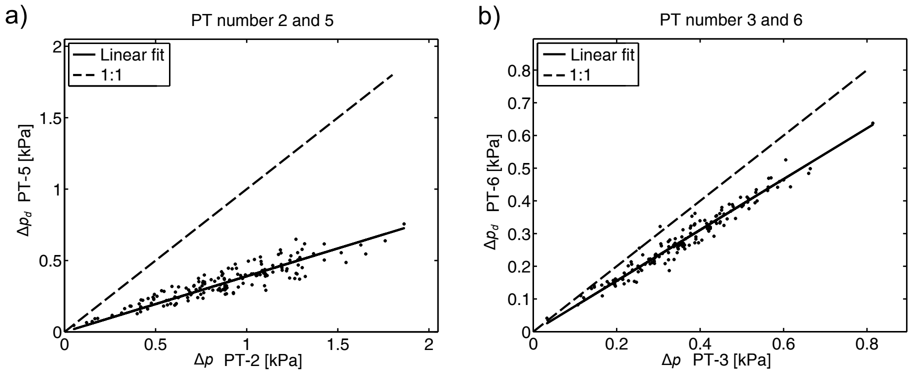

Figure 3.8: Damping of the pressure wave inside the bank during the experiment *Pinbank54*, measured by a pair of PTs located at the same depth. PTs 2 and 5 are located 13 cm below the bank surface a), PTs 3 and 6, 20 cm below bank surface b). See Figure 3.3c for PT location.

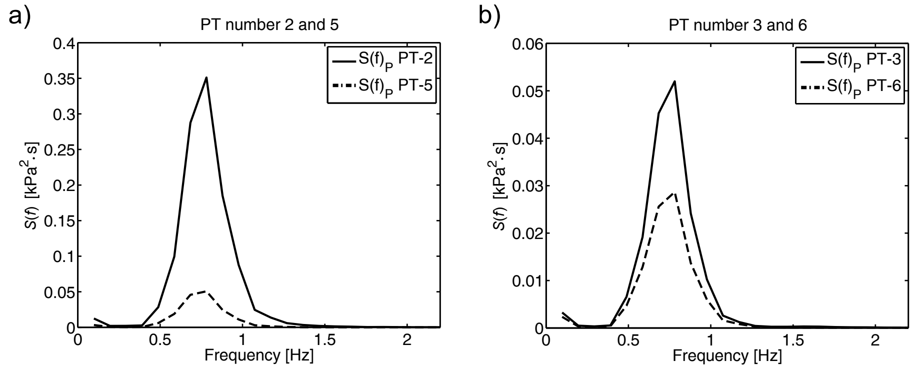

Figure 3.9: Damping of the pressure wave spectrum inside the bank during the experiment *Pinbank54* for PTs 2 and 5, located 13 cm below the bank surface a), and PTs 3 and 6, located 20 cm below the bank surface b).

Several mass failures were observed during the experiments which are similar to the failure processes described in Figure 3.2. A description of the characteristics of observed failures is reported below.

During the experiment *Pinbank54*, a toppling failure of the top block occurred in the first minute of the experiment. A tension crack appeared on the top of the bank as a consequence of the stress induced on the soil matrix by the wave action. Then the failure for toppling occurred. Roughly two minutes after the beginning of the experiment, new cracks formed on the top of the bank in the interior marsh. Removal of very small pieces of soil from the edge of the physical model occurred around $1'55''$ into the experiment, while at time $2'55''$ another failure of a small piece of soil occurred mostly on the right side of the frontal part of the bank. The experiment *Pinbank62* started from the final configuration of the previous one. During the experiments tension cracks became wider but no mass failure were observed.

During the experiments *Pinbank40* and *Pinbank32*, no mass failures occurred. Also in this case tension cracks on the top of the bank became wider, and they were surveyed at the end of the *Pbank32* experiment.

The pressure field inside the bank was also measured during *Pfailbank54* experiment, when several mass failures occurred. The initial configuration was characterized by wide tension cracks, and an unstable block in the frontal portion of the bank. After $45''$ from the beginning of the experiment the tension crack was several centimetres wide and the block started to oscillate. Failure was observed at time $55''$. After $1'10''$ into the experiment a second toppling failure, more rapid then the previous one, was observed. After few seconds, a third failure occurred on the right side of the bank.

During the experiment wave overtopping was a common process and cracks were frequently filled with water. This configuration led to an imbalanced system of forces in correspondence of the wave trough. In such a configuration, the water inside the crack could push the block toward the channel without encountering any resistance from soil or fluid. This was identified as one of the most significant processes leading to the failure of a block. Toppling failures described above will be used to test the proposed model in Section 3.5.1.

Starting from $3'$ into the *Pfailbank54* experiment, the upper part of the bank was interested by intense turbulence processes due to the effect of impacting waves. The removal of small pieces of soil (mass erosion) and single particles (surface erosion) occurred frequently and lasted until the end of the experiment. Due to the erosion process the exterior PT (number 1) was removed.

In Appendix A the time series of pressure measurements during the first two minutes of the *Pfailbank54* experiment are reported. This aspect is not specifically addressed within the present work since more data would be necessary to characterize the relation between pore water pressure and failure. Indeed, a model describing the coupled behaviour of the liquid, gas and solid phases under periodic loading would required in order to interpret the experimental data.

In Table 3.2 the dimensions of the slumped blocks are reported.

Table 3.2: Dimension (in cm) of the collapsed blocks observed in the experiments.

Experiment Label	d_b	l_b	L_b
U4.1HW [*Francalanci* et al., 2013]	13	30	50
	22	35	50
Pfailbank54	15	30	50
	10	21	40

3.5 Toppling model validation, results and discussion

First, the results of the model developed in Section 3.3 for the simulation of toppling failure events are compared with those obtained from laboratory experiments. Then, a critical analysis of the obtained results is carried out.

3.5.1 Model validation against laboratory experiments

In order to test the ability of the model to identify the incipient failure of an unstable block, four mass failure events were selected to be analysed. The collapsed blocks were approximately prismatic and large enough to be well described by the model. Simulations of toppling failure were conducted for these four events: one observed during the experimental campaign carried out by *Francalanci* et al. [2013], after around 30 s from the beginning of the experiment *U4.1HW*; the remaining three mass failure events observed during the experiment *Pfailbank54*.

The results of the simulations are plotted in Figure 3.10 and 3.11. The values of the empirical and theoretical parameters adopted for the simulations are reported in Table 3.3.

The value of cohesion c_u, representing the tensile strength of the soil, the value of soil wet density ρ_s, and the value of void ratio e_0 chosen to calculate the shear modulus through Equations A.7 and A.8 are taken from the results of the geotechnical analysis of a sample collected in the field (see *Francalanci* et al. [2013]). The values for the same quantities mentioned above, obtained from the sample collected by *Francalanci* et al. [2013] at the end of the experiment *U4.1HW*, were not representative of soil characteristics because the sample experienced a very high water content. For this reason they were not used in the present work.

Figures 3.10a and 3.11a show the time series of water displacement η_i corresponding to the incident wave component. The time and the duration were recorded for each failure event and are reported in Figures 3.10a and 3.11a. In

Table 3.3: Values of empirical and theoretical parameters employed in the computations.

Empirical Parameters	**Value**	**Unit**
b_h	60	cm
ρ_s	1700	kg/m^3
e_0	1.296	-
c_u	8.0	kPa
h	54	cm
Theoretical Parameters	**Value**	**Unit**
φ_0	0	rad
Crack's degree of filling	0.9	-
C_φ tuned by the author	$5 \cdot 10^3$	-

Figures 3.10b and 3.10c and 3.11b–3.11g, the time evolution of the most significant variables of the model is shown: the wave force on the unstable block F_w, the response angle φ with respect to time and the time evolution of the stress σ_s at points A and B of the failure surface (Figure 3.5b).

It is assumed that mass failure occurs when the tensile strength of the material is exceeded in at least one point of the failure surface. The mass failure of experiment *U4.1HW* occurred around $30''$ after the beginning of the experiment. The wave group responsible for the failure is clearly recognizable, and the maximum tensile stress exerted on point A of the failure surface is reached at wave trough. Furthermore, it is possible to observe that the model is able to capture, for all analysed cases, the wave train leading to block collapse, except for the first failure of the experiment *Pfailbank54* (Figure 3.11a and 3.11c). In such a case, the value of d_b (22 cm) is higher than for the other blocks, and this limitation of the model could be explained by the need to introduce a progressive failure mechanism (see Section 3.5.2). For the second and third failures of experiment *Pfailbank54* (Figure 3.11a, 3.11e and 3.11g), the wave groups responsible for failure are identified by the model. For the third one, a wave group induced the stress to reach a value significantly close to the tensile strength threshold before the occurrence of the failure.

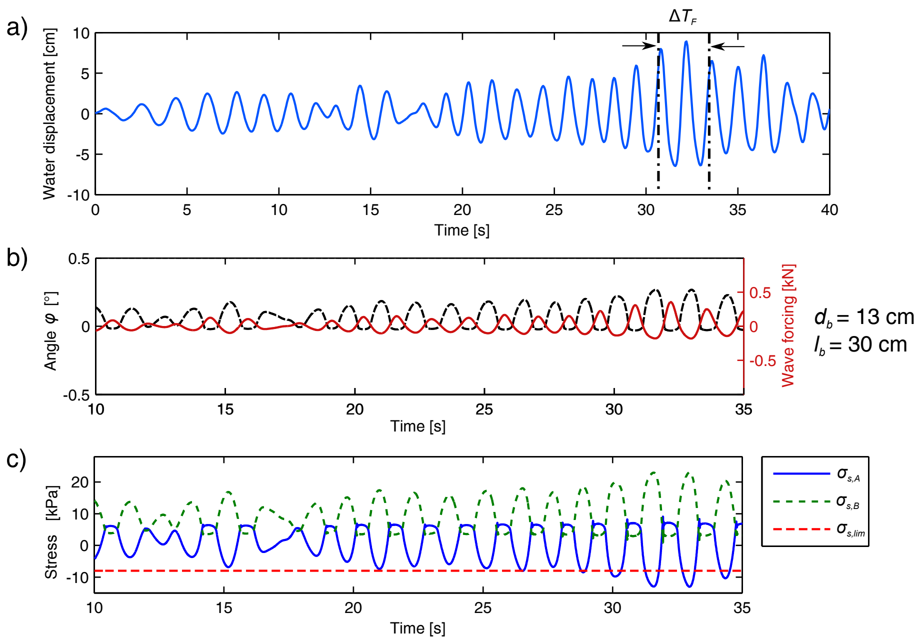

Figure 3.10: Results from the model test on the experiment *U4.1HW*, [*Francalanci* et al., 2013]. Block height and length are, respectively, 30 cm and 11 cm. a) Water surface elevation η_i and time interval at which the failure occurs (light blue continuous line and black dash-dotted line) and the duration of the failure ΔT_F. b) Time evolution of the angle φ (black dashed line) and of the wave force F_w (dark red line). c) Time evolution of the stress σ_s at the inner point (blue continuous line) and at the outer point of the failure surface (green dashed line) and limit tensile strength (red dashed line).

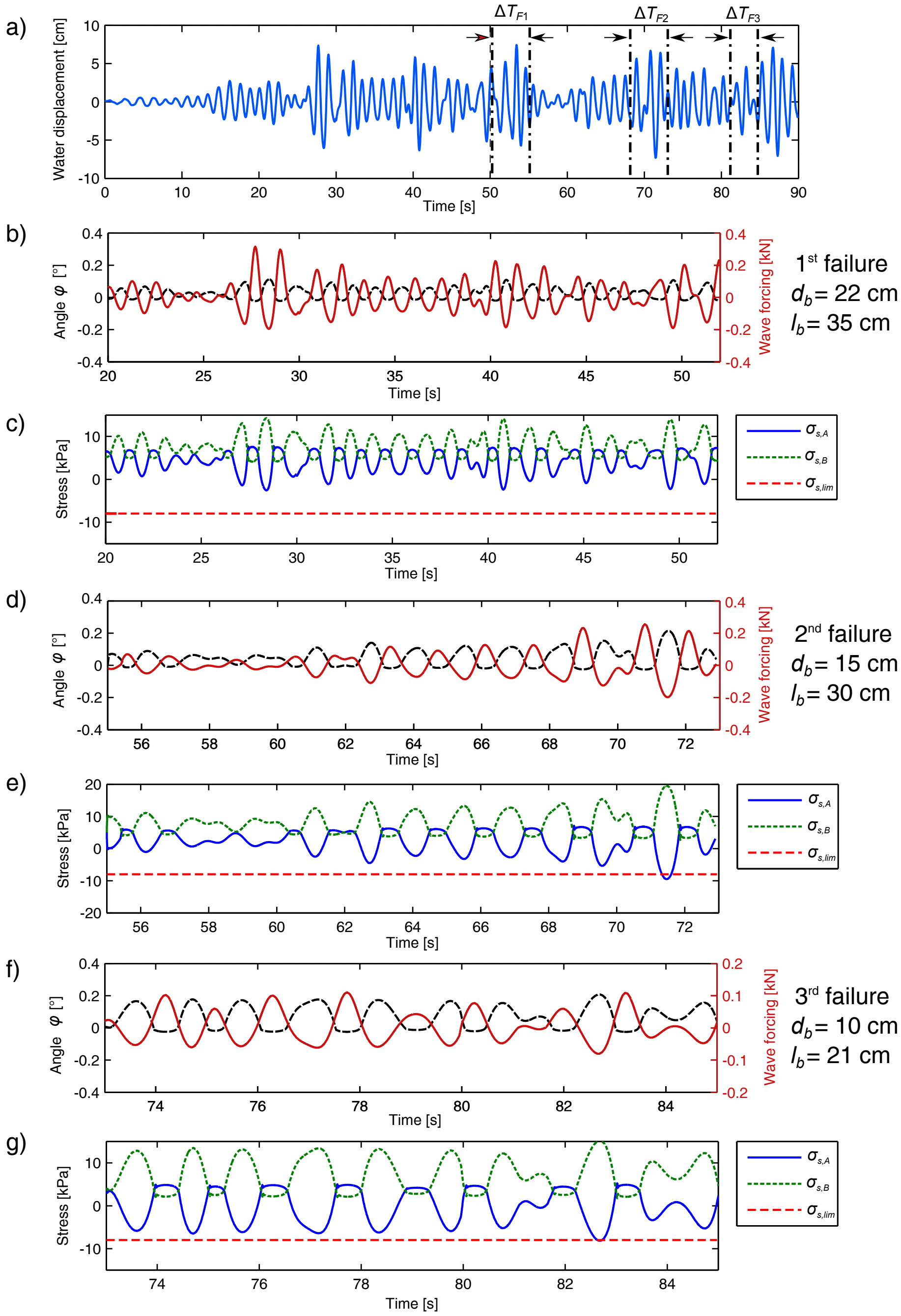

Figure 3.11: Results from the model test on the experiment *Pfailbank54*. a) Water displacement η_i (light blue continuous line) and time interval in which failure occurred (black dashed lines). $\Delta T_{F,i}$ represents the duration of the i-th failure. b), d), and f) Time evolution of the angle φ (black dashed line) and of the wave hydrodynamic forcing (dark red line). c), e), and g) Time evolution of the stress at the inner point (blue continuous line) and at the outer point of the failure surface (green dashed line) and limit tensile strength (red dashed line).

3.5.2 Critical discussion

In this section the following relevant issues are discussed: (i) effect of water in cracks on toppling failure and dynamic response of the system; (ii) conditions leading to block instability; (iii) formation of tension cracks, and (iv) effect of vegetation on toppling failure. Finally, concluding remarks on the input parameters and data for the topping failure model will be provided.

The presence of tension crack is necessary to trigger the toppling failure mechanism. This was extensively documented by laboratory experiments. In all observed cases, the cracks were filled with water at the moment of failure and wave overtopping of the marsh bank was the main source for water filling the cracks. It is possible to argue that the presence of water inside the crack is crucial in promoting the failure on an unstable block. Indeed, the model prescribes that failure can only occur when the system of forces acting on the block leads to an excess of tensile stress on the failure surface, and this happens more frequently at wave trough when the crack is filled with water. In such a case, the block can be pushed enough toward the channel to reach the tensile stress limit. At wave crest, the maximum force is exerted on the bank and the block is constrained to not oscillate counterclockwise due to the presence of water and of the stable bank behind it. This effect (constraint to oscillation) is implemented in the model by increasing the spring stiffness when the angle φ tends to reach negative values (see Appendix A). Physically, it means that the block can rotate counterclockwise until it roughly reaches its initial configuration. At this point, the further small counterclockwise rotation induced by the wave provides elastic potential to the system that is subsequently released at wave trough when the block is free to rotate clockwise. This dynamic effect appears to have a substantial effect on the value of the maximum tensile stress acting on the failure surface.

To analyse the effect of water filling the crack and the dynamic response of the system, the model was run for a generic geometric configuration ($b_h = 80$ cm, $d_b = 25$ cm, $l_b = 45$ cm, and $h = 70$ cm), considering the cases of crack filled or not filled with water, with a regular wave forcing $H = 14$ cm and $T = 1.5$ s (Figure 3.12). Furthermore, to stress the dynamic character of the response of the system, a simulation using a simplified static approach was also run. With this approach, the response of the system to a fixed water level, set equal to the lowest value reached at wave trough during the dynamic case, is evaluated.

The stress for the static case $\sigma^{st}_{s,A}$, acting in point A of the failure surface, is reported in Figure 3.12. It is possible to observe that the stress clearly reaches higher values when the crack is filled with water. Point A is subject alternately to positive and negative stress whereas point B is always compressed. When the crack was not fully filled with water, both points A and B were compressed for the most part of the simulation due to the weight W_b of the block itself. Negative stresses (traction) at point A are reached at the wave trough, and they are significantly smaller (in absolute value) with respect to the negative stresses reached during the simulation with the filled crack. It is important to point out that in both cases, the dynamic response of the system strongly affects the stress distribution on the failure surface, and that the calculation on the basis of the static response of the system would have led to different results.

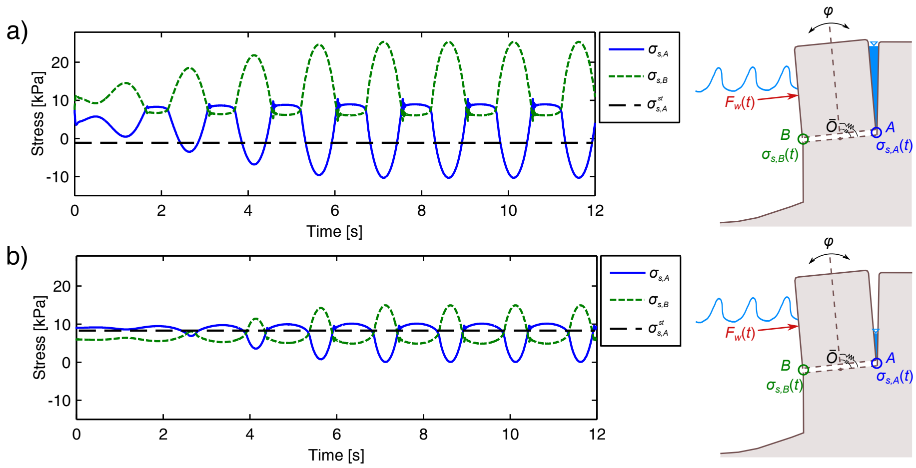

Figure 3.12: Effect of water in cracks on toppling failure and dynamic response of the system: a) crack filled with water or b) crack not filled with water. The blue continuous line represents the time evolution of the stress at the bottom of the tension crack in the inner point of the failure surface. The green dashed line represents the stress at the external point of the failure surface. The black dashed line represents the stress at the bottom of the tension crack in the inner point of the failure surface obtained by a static approach.

With reference to the second point, observations in the laboratory suggest that bank overtopping is related to the least stable condition for block stability. During experiments *Pinbank40* and *Pinbank32*, the waves did not overtop the bank, and the most reliable hypothesis is that the water level inside the crack was equal to the external mean water level. During *Pinbank54* and *Pfailbank54* experiments, the wave crest often exceeded the top of the bank leading to a complete filling of the crack. For the model runs, this effect is reproduced assuming that once overtopping occurs, the degree of filling reaches a constant value equal to 0.9. This configuration implies the mean water levels inside and outside the crack are different. As a consequence, the higher the difference, the higher is the possibility that failure occurs at wave through. On the other hand, it is important to note that the complete filling of the crack occurs when waves are high enough to overtop the bank. The relative bank freeboard b_F is then used to parametrize the problem:

$$b_F = \frac{b_h - h}{H/2} \tag{3.10}$$

where b_h is the bank height and $H = H_i + H_r$ is the wave height at the bank edge, assuming a reflection coefficient K_r equal to 0.75. In the present case, the water depth h corresponds both to the MSL and the MWL because the floor of the channel is used as reference frame and wave setup is neglected. The maximum values of tensile stress exerted on the failure surface are plotted against relative freeboard b_F for different depths of the tension crack l_b in Figure 3.13. The characteristics of the simulations are here summarized: incident wave height $H_i = 0.14$ m, $K_r = 0.75$, $T = 1.5$ s, $b_h = 0.8$ m, $d_b = 0.2$ m, and $L_b = 0.5$ m. Three values of l_b were tested, 0.40 m, 0.45 m and 0.50 m. It is possible to observe that higher values of tensile stress are reached when b_F is close to 1, while they decrease rapidly when b_F increases above 1. Negative values of b_F, imply that the bank is completely flooded ($b_h < h$). In such a case the stress tends to decrease and the configuration becomes less critical for bank stability. Hence, for a specific bank and wave height, the most critical condition for bank stability will be when b_F is a little smaller than 1. This corresponds to a configuration in which the water depth is at the minimum value that allows overtopping, and as a consequence, the filling of the crack.

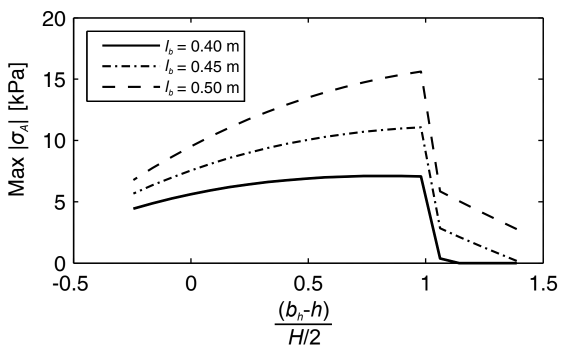

Figure 3.13: Maximum values of the tensile stress exerted on the failure surface against relative bank freebord b_F by varying water depth h in front of the bank for different depths of the tension crack l_b. The continuous line corresponds to $l_b = 0.40$ m, the dash-dotted line to $l_b = 0.45$ m, and the dashed line to $l_b = 0.50$ m.

The presence of cracks is crucial for the retreat of a salt marsh bank. Therefore, an improved understanding of the associated mechanisms is required. Several mechanisms for crack formation have been proposed by different authors: desiccation processes across seasonal variation [*Allen*, 1989; *Morris* et al., 1992] and cyclic oscillation of mean and effective stresses due to tide [*Cola* et al., 2008]. Both mechanisms act at large time scale, and are associated with filtration processes. Nevertheless, in the experimental study, the formation of vertical cracks occurred for the test series with tide only as well as for those with waves superimposed to tide. Indeed, crack formation was observed throughout the whole retreat process, as a trigger for mass failures. Wave-induced loads seem capable to weaken a portion of the bank leading to the formation of a crack. A similar process was proposed by *Adams* et al. [2005] for rocky cliffs in coastal areas. This mechanism acts at a shorter temporal scale, and it does not directly involve filtration processes since muddy banks have generally low-permeability coefficients. Further investigations on the process of formation of tension cracks due to wave impact, might start from the approach proposed by *Adams* et al. [2005], adapted to cohesive banks.

Finally, the role played by vegetation in the mass failure processes is still an open issue. On one hand, vegetation can possibly increase the porosity of the soil and the filtration velocity, possibly reducing soil resistance; on the other hand, the presence of the root mat can induce an additional cohesion to the soil matrix reducing the depth of the cracks and their frequency of occurrence. Furthermore, it was shown that vegetation can delay the failure of the vegetated clods [*Francalanci* et al., 2013]. When included in the toppling model, the effect of vegetation may result in a delay of the mass failure, but a more detailed description of the root mat structure and of the soil stress characteristic would be needed. It is important to stress that in the toppling failure model, the failure process is assumed to occur instantaneously once a specific threshold of stress is exceeded. However, the inclusion of the vegetation would require a progressive failure mechanism, due to the progressive detachment of the block of soil from the failure surface induced by the cumulative effect of waves. Indeed, even if the extension failure surface would be progressively reduced by the effect of waves, root mat may continue to offer a resistance against the mass failure. Furthermore, different typologies of plants may diversely affect the failure process since the extent of the rootmat can have a control on the depth of the formation of tension cracks and, as a consequence, on the dimensions of the block subject to failure.

In general, the model represents a first attempt to investigate the main physical processes responsible for toppling failure in cohesive banks. Indeed, many parameters have been assigned from experimental studies or from theoretical analysis as input parameters for the simulations. It is important to note that the following parameters would need a further investigation: the void ratio e_0, the shear modulus G, the wet soil density ρ_s, and the cohesion c_u. Indeed, they can be affected by uncertainties from laboratory analysis and sample collection. Furthermore, the dimensions of the cracks and blocks as employed in the simulations were measured approximately due to the presence of water in the channel and due to irregularities in the geometry of the blocks.

3.6 Summary and concluding remarks

In this chapter, a new mathematical model for the description of the toppling failure of a salt marsh bank induced by wind wave forcing is presented. The model is developed based on laboratory observations and validated against experimental results. The experiments were carried out in a wave flume in which two physical models were built in order to measure the hydrodynamic pressures on the front face of a salt marsh bank and the transmission of these pressures inside the bank.

The model describes the response of an unstable soil block with a tension crack to wind-induced waves. Indeed, experimental observations showed that tension cracks are crucial in triggering mass failures. Furthermore, experimental data were employed to determine several empirical parameters used as model input and also provided some test cases for the toppling failures under given hydrodynamic conditions. The hydrodynamic forcing is described wave by wave by means of linear wave theory. A correction factor (set equal to 1.75), determined from experimental results, is applied to the wave forcing to implicitly account for the potential effect of nonlinearities and wave reflection. The testing of the model against experimental data showed that the model is able to predict the toppling failure and to identify the group of waves responsible for the final detachment of the unstable blocks in three of the four monitored cases.

Furthermore, the simulations have demonstrated that the presence of water inside the tension crack, together with a lower water level in front of the bank, are the most unfavorable conditions for bank stability.

Finally, bank failures are strongly affected by the dynamic response of the system. From the results, it is possible to argue that inertial effects, and the elastic potential energy accumulated by the system during compression (wave crest at the bank face), and released at the wave trough, lead to higher stresses on the failure surface. Indeed, a simple static model characterized by an instantaneous response of the system to a given water level would lead to smaller stresses and a more stable condition.

The present model represents a first tool for predicting the stability of cohesive banks prone to mass failure by wind-induced waves, and also provides an improved insight into the mass failure mechanism.

Future developments of the present model might consist in the following additional aspects which need to be considered: effect of vegetation on bank stability, triggering mechanism for tension crack formation, and 3-D geometry of the unstable soil blocks, including the effect of the lateral resisting forces.

Chapter 4

Field Measurement Activity in the Lagoon of Venice

Present chapter describes the field monitoring campaign carried out at a salt marsh of the Lagoon of Venice and the development of a simple mathematical model to describe the effect of cantilever failure on the cumulative retreat of the bank. The monitoring period started in November 2013 up to April 2015. The main objectives of this part of the research can be summarized as follow:

- the determination of a relationship (if present) between wave energy flux W and volumetric erosion rate per unit length of the marsh edge R_{sc} at the time scale of months;
- the identification of a wave power threshold for the onset of erosion;
- the quantification of the different contributions of mass failures and surface erosion to the overall bank retreat;
- the explanation of the mechanism leading to the formation of cantilever profiles and the estimation of its effect on cumulative bank retreat by means of a simple mathematical model.

In the first section the monitored area is described together with the erosive trend observed in the last decades. Subsequent section contains the field measurement setup and the employed methodologies to analyse collected data. Then, the results of data analysis are presented and discussed. Output from the discussion laid the basis for the development of a mathematical model describing the effect of cantilever failures on bank retreat. Finally, conclusions are drawn and future developments are proposed.

4.1 Monitored area and erosive trend

The salt marsh surveyed in the present study is located in the north part of the Lagoon of Venice, west of Sant'Erasmo island (Figure 4.1a).

Salt marshes in this area have bank heights in the range 0.3–0.8 m (Figure 4.1c and Figure 4.2). Some portions of the marsh boundary are quite irregular and the shoreline is exposed to north-east, north-west and south-east directions, depending on the orientation of the banks. The shoreline is characterized by steep slope cliffs (Figure 4.1c and Figure 4.2), covered by vegetation, whereas the gullies generally show a gentle profile without vegetation, except for really narrow incisions dissecting the marsh which exhibit a sharp variation between mudflat and marsh top. The top of the marsh (identified by GPS measurements) is approximately located 25 cm above the mean sea level (MSL) that is, since 2009 to date, about 26 cm above the reference level of Punta Salute (PS). PS is used as zero reference for the water level measurements from the permanent stations managed by the Tidal Center of the Municipality of Venice[1].

North-east is the direction of the dominant wind "Bora", that is the most frequent wind from October to late spring [*Cushman-Roisin* et al., 2013], and leads to the most adverse storm surges. Wind called "Scirocco" blows from south-east and dominates the summer season, but it usually does not exceed 5 m/s (Figure 4.1b). However, during summer, occasional short storm surges are characterized by north-west direction winds which can easily reach 15–20 m/s.

The marsh border has considerably retreated during the last 30 years, as documented in Figure 4.3. The analysis of aerial photographs was carried out by comparing different pictures at subsequent times (1978 and 2010). The vegetated front, defined as the interface between vegetated and unvegetated areas, was identified as the retreating boundary of the scarp. Photographs of the area are available on the GeoPortale IDT[2] provided by Regione Veneto. Due to the relatively low quality of these pictures, the comparison between images separated by a short time span (2–4 years) would lead to retreat estimates of the same order of magnitude of the pixel size. For this reason, only photographs of 1978 and 2010 were compared.

Alternative sites examined for the monitoring activity were located in the south part of the lagoon, but even if subject to larger fetches and, hence, to potentially stronger storm surges, they were excluded because they have recently been protected by artificial revetments. Furthermore, instrumentation in the south part of the lagoon is more likely subject to possible damages due to the higher presence of small fish-boats.

Figure 4.3 shows that the marsh surface loss depends not only on the border

[1] Web page URL: `http://www.comune.venezia.it/flex/cm/pages/ServeBLOB.php/L/IT/IDPagina/1748`

[2] Web page URL: http://idt.regione.veneto.it/app/metacatalog/

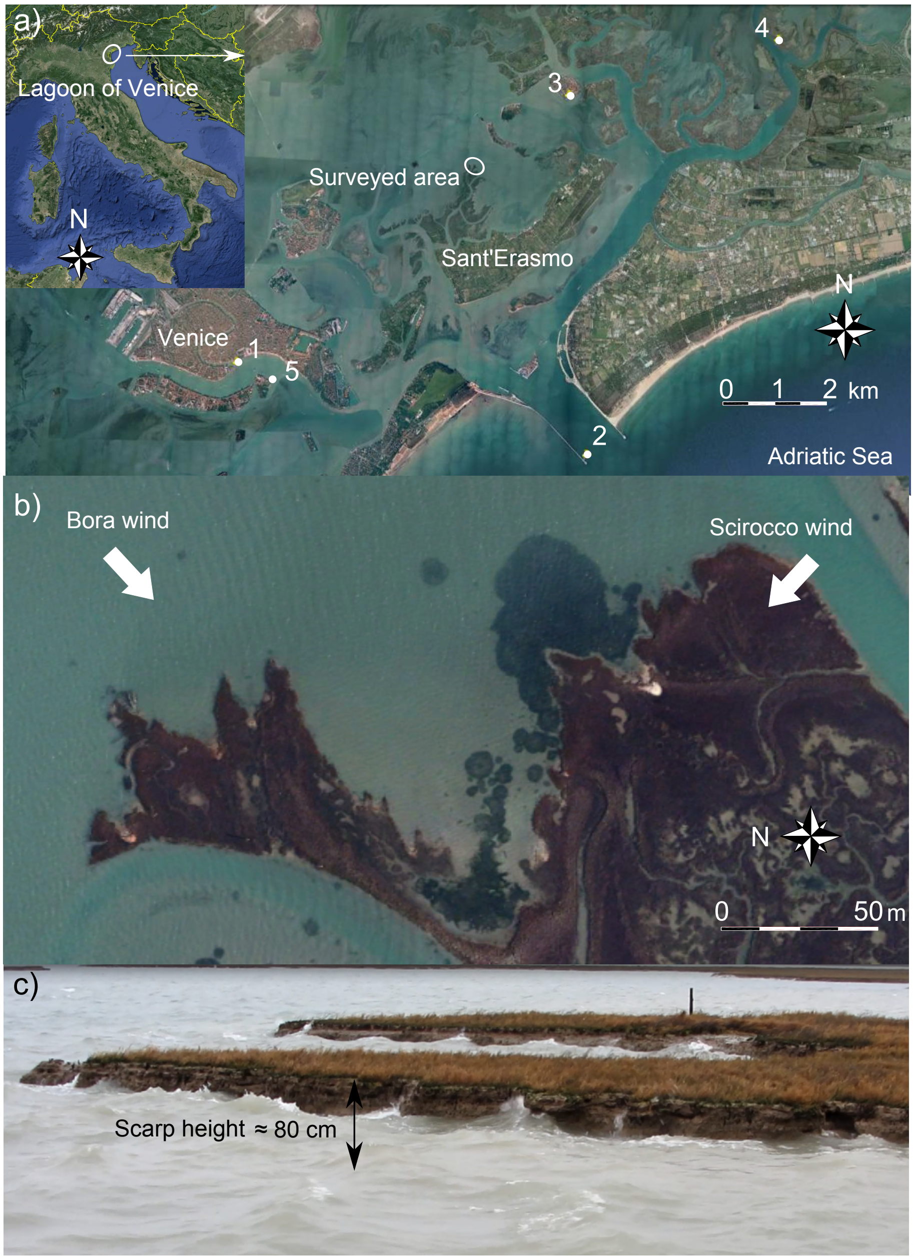

Figure 4.1: a) Locations of the investigated salt marsh (encircled) and of the fixed monitoring stations, managed by the Tide Center of the Municipality of Venice: 1, Punta Salute; 2, Diga Sud Lido; 3, Burano; 4, Laguna Nord Saline; 5, San Giorgio. b) Enlarged view of the monitored marsh, with indicated Bora and Scirocco wind directions. c) View of the salt marsh border subject to wave forcing during November 2013.

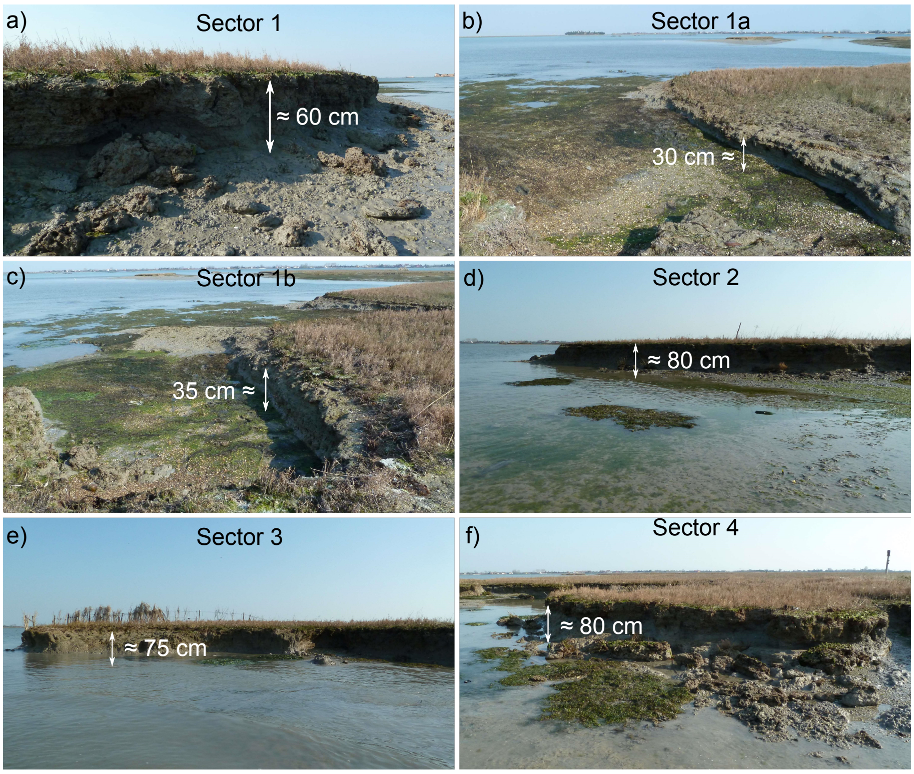

Figure 4.2: Views of the marsh edge in the surveyed sectors, with indicated local bank heights.

orientation but also on the location within the marsh. This peculiar pattern is likely due to the coupled effect of wind wave and boat waves. Indeed, the northernmost point, associated to the highest erosion, is subject not only to waves originated by Bora winds and sporadic but intense north-west winds, but also to waves induced by boats travelling from Venice and Murano to Burano. Conversely, the salt marsh banks facing east direction are adjacent to an area with a low boat traffic and, hence, can be directly affected only by Bora wind waves.

In order to characterize the various erosive patterns at time scales of months, 6 different sectors to be analysed were identified on the salt marsh (Figure 4.2 and 4.3). They were recognized on the basis of the different orientations and erosive trends. All sectors tend to be exposed to Bora wind. Sectors from 1 and 2 are less exposed to boat waves and are only partially affected by summer storm surges (coming from north-west). Sector 3, due to its orientation, is mainly reached by north-east waves almost parallel to the boundary, and it might show a different behavior with respect to other sectors. Sector 1 is the only one directly exposed to light Scirocco winds and it is of interest to verify if such weak forcing can also affect the erosive trend.

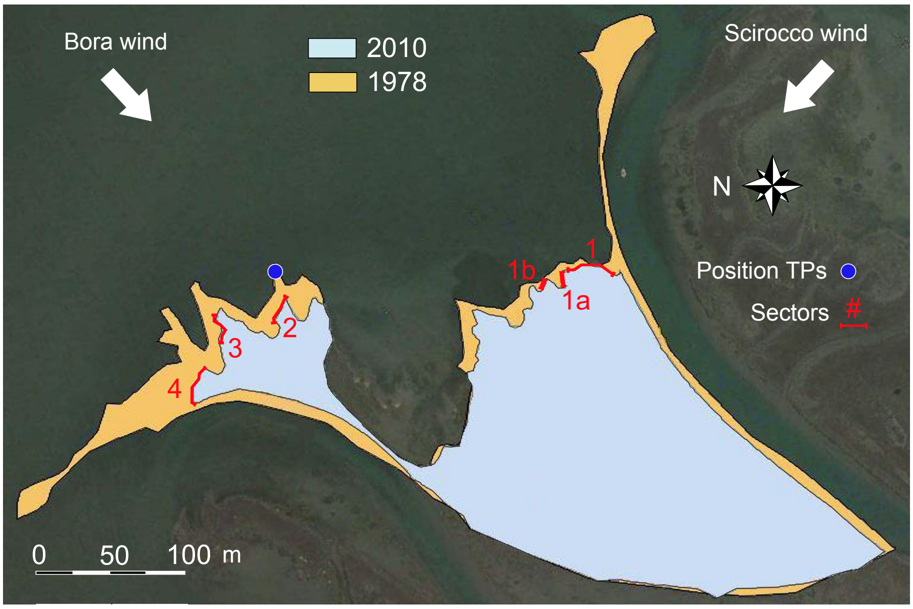

Figure 4.3: Observed retreat area estimated through comparison of aerial photographs collected in 1978 and 2010 and localization of the six sectors (in red) where the erosion pins have been deployed. A blue dot identifies the deployment location of the pressure transducers during wave height measurement surveys.

Figure 4.2 illustrates a view of the scarp features characterizing each sector. The main retreat mechanism has been found to be the continuous erosion (i.e. removal of sediment particles or small lumps of soil with sizes of the order of cm), alternated to mass failures, mostly of cantilever type. The entity and frequency of mass failures change according to the sector. At the toe of the lowest level edges (sectors 1a and 1b in Figure 4.2b and 4.2c) collapsed blocks were rarely observed. This can be ascribed to the fact that cantilever profiles tend to develop more slowly, due to the lower height of the bank (Figure 4.2b, c) which is less prone to wave attack, and consequently slumped blocks are small enough to be rapidly eroded by the flow. Sectors with higher bank level show blocks of different dimensions at the toe (Figure 4.2a, d, e and f). In general sector 4 is subject to more frequent and larger cantilever failures than the others, whereas sector 3, although close to it, is not regularly affected by this type of erosion events. Patches of pioneer vegetation are generally present on the mudflats adjacent to all sectors.

4.2 Field setup and methodologies

The aim of the present field measurement activity is to estimate the wave forcing impinging on the marsh edge during adverse storm events and correlate it to local erosion rates.

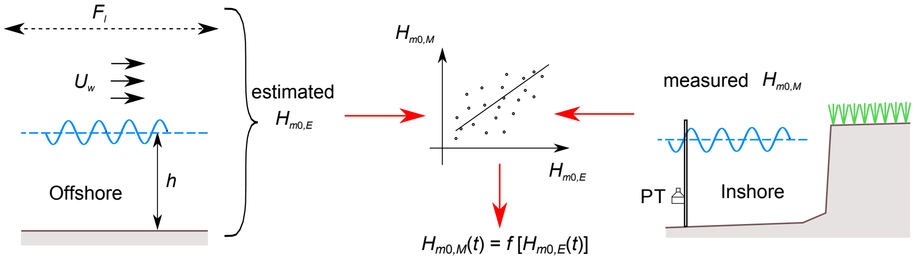

Figure 4.4: Sketch representing the procedure employed to estimate wave forcing at the marsh scarp. A functional relation is determined between the zero-th moment wave height measured inshore, $H_{m0,M}$ and $H_{m0,E}$ estimated through Equation 4.7 (on the basis of offshore wind velocities and water depths provided by the monitoring stations shown in Figure 1). PT: pressure transducer, F_l: fetch, U_w: wind velocity, and h: offshore water depth.

Occasional measurements of wave height from pressure gauges close to the marsh bank and estimation of wave climate through hourly data of wind, fetch and water depth are used to extrapolate a relation between wave climate estimated offshore $H_{m0,E}$ and measured inshore $H_{m0,M}$ (Figure 4.4). In this way it is possible to evaluate continuously the inshore forcing from offshore wave climate, thus avoiding a continuous deployment of instrumentation in the field. Indeed, pressure gauge measurements are difficult to carry out: they need the deployment of electronic instruments in the field in presence of significant tidal excursion and wind waves. Moreover, the monitored marsh is reachable only by boat.

In order to link offshore and inshore wave climate, the latter was measured for three storm events occurred on 18, 21 and 28 February 2014. Wind, fetch and water depth data needed to estimate the offshore wave climate, were provided hourly by 5 permanent stations, located in the north part of the Lagoon of Venice, close to the northernmost inlet (Figure 4.1a).

Erosion rates were monitored since November 2013 and 17 surveys, identifying 16 different time intervals, were carried out till April 2015 (Table 4.1).

4.2.1 Wave climate from pressure gauges ($H_{m0,M}$)

Three pressure transducers (PT) Series 46x, produced by Keller Instruments, were used to measure inshore wave climate. The resolution of the sensors is 0.1 mbar and the range of measurement is 0.0–100.0 mbar. These sensors were located about 7–8 m from the scarp of the marsh edge (Figure 4.3 and 4.4), at a distance of 15 cm from the bottom of the tidal flat next to the marsh. The transducer membrane was arranged face down to prevent that sediment particle might settle on it and to avoid the dynamic pressure effect generated by the component of the velocity normal to the sensor face [*Cavaleri*, 1980].

Table 4.1: Summary of the field surveys carried out in the monitored marsh. The first column reports the ordering number; the second column reports the time interval elapsed between two consecutive surveys, and the third column the dates of the surveys.

Nr.	ΔT (days)	Dates
1	81	29 November 2013 - 17 February 2014
2	10	18 February 2014 - 28 February 2014
3	6	1 March 2014 - 6 March 2014
4	54	7 March 2014 - 29 April 2014
5	27	30 April 2014 - 26 May 2014
6	29	27 May 2014 - 23 June 2014
7	27	24 June 2014 - 20 July 2014
8	29	21 July 2014 - 18 August 2014
9	30	19 August 2014 - 17 September 2014
10	30	18 September 2014 - 18 October 2014
11	39	19 October 2014 - 26 November 2014
12	21	27 November 2014 - 17 December 2014
13	33	18 December 2015 - 20 January 2015
14	31	21 January 2015 - 20 February 2015
15	26	21 February 2015 - 18 March 2015
16	28	19 March 2015 - 15 April 2015

Data were collected by a data logger located, together with its batteries, inside a waterproof caisson raised with respect to the marsh surface and secured to the ground. The Sampling rate was set to 6 Hz; 17 minutes of recording (1 burst) started every 1.5 hours. Overall, a time period of roughly 87 hours was monitored. Sampling rate, number of bursts and duration were selected in order to find a balance between the needs to characterize the wave field and the storage capacity of the data logger. Table 4.2 provides a summary of the measurements.

Table 4.2: Summary of the field surveys carried out to measure the inshore wave climate in front of the marsh during three storm surges.

Start time		End time		Duration (hours)	Nr. of bursts (-)
Date	Time	Date	Time		
18/02/14	18:00	20/02/14	2:00	32	22
21/02/14	16:30	22/02/14	17:00	24.5	17
28/02/14	16:30	01/03/14	23:00	30.3	21

Several authors recommend to use pressure transducers to measure wave climate both in intermediate and shallow water [*Lee* and *Wang*, 1984; *Bird*, 1993]. To recover wave height from pressure data, linear wave theory [*Bishop* and *Donelan*, 1987; *Tsai* et al., 2005] or higher order theories with non-linear terms [*Lee* and *Wang*, 1984] can be used. It was pointed out that the use of linear theory may lead to errors in wave estimation if strong currents are present [*Jones* and *Monismith*, 2007], in the present case, however, PTs are quite far from tidal channels (Figure 4.3) and adjacent to a wide tidal flat where current velocities are likely low.

For the above reasons, the linear wave theory is applied to recover the free surface displacement from pressure measurements [*Dean* and *Dalrymple*, 1991]. The relation between the spectral density distributions, $S_{\eta\eta}$ and S_{pp}, respectively related to free surface displacement $\eta(t)$ and pressure head $p(z,t)$ is:

$$S_{\eta\eta}(f) = \frac{1}{K_p^2(f,z)} S_{pp}(f,z) \tag{4.1}$$

where f is the frequency, z is the elevation with respect to the mean water level and $K_p(k,z)$ is the pressure response factor, defined as [*Dean* and *Dalrymple*, 1991]:

$$K_p(k,z) = \frac{\cosh[k(h+z)]}{\cosh(kh)}. \tag{4.2}$$

Here h is the mean water depth, and $h+z$ corresponds to the distance of the PT from the bottom, k is the wave number determined from the dispersion relation $\sigma^2 = gk\tanh(kh)$, with σ the wave frequency and g the acceleration of gravity. The value of the significant wave height is obtained from the relation [*Dean* and *Dalrymple*, 1991]:

$$H_{m0,M} = 4\sqrt{m_0} \tag{4.3}$$

where m_0 is the zero moment of $S_{\eta\eta}(f)$.

To obtain $S_{pp}(f)$ from collected data, the following procedure is carried out. Rough data time series (one burst) of pressure head measurements, denoted with $\bar{x}_\mathrm{r}$, are initially filtered to remove spikes and to obtain a new time series of validated data points to be employed for the determination of $S_{pp}(f)$. First, a five points moving average is applied to $\bar{x}_\mathrm{r}$, obtaining $\bar{x}_\mathrm{a}$. Then, denoting by $\sigma_{\Delta x}$ the standard deviation of the vector $\bar{x}_\mathrm{r} - \bar{x}_\mathrm{a}$, the k-th value is considered as a spike and is removed if $|x_{\mathrm{r},k} - x_{\mathrm{a},k}| \geq 3\sigma_{\Delta x}$. Removed spikes for each data series resulted in around 0.1–0.2 % of the total amount of data. A spectral analysis on each filtered time series was then carried out using the modified Welch method [*Welch*, 1967]. Each record was detrended and divided into segments of 128 data points, overlapping by 50 % and Hamming windowed. Finally, a FFT (Fast Fourier Transform) [*Cooley* and *Tukey*, 1965] algorithm was applied to each segment and the resulting spectra were averaged to obtain the pressure head density spectrum $S_{pp}(f)$ representative of each burst.

The determination of the spectral density $S_{\eta\eta}(f)$ from $S_{pp}(f)$ is not straightforward, K_p tends to reach too high values with increasing wave frequency and submergence of the sensor. In order to obtain a reliable estimation of the spectral density, Equation 4.1 was obtained for $f \in [0, f_c]$, where f_c is a cut-off frequency [*Jones* and *Monismith*, 2007], while the tail of the spectrum was extrapolated by assuming that it can be approximated as f^{-5} [*Wolf*, 1997]. For the cut-off frequency, f_c was chosen as the the minimum value among those proposed in literature:

$$f_c = \min \begin{cases} f_{c,n} \mid K_p^2(f_{c,n}, z) = 0.01 & [\textit{Tucker and Pitt}, 2001] \\ f_{c,n} \mid \frac{S_{pp}(f_{c,n})}{W_n} = a_1 & [\textit{Jones and Monismith}, 2007] \\ a_2 \cdot f_p & [\textit{Jones and Monismith}, 2007] \\ f_T. & \end{cases} \tag{4.4}$$

The noise floor of the instrument W_n, was computed as:

$$Res = \sqrt{\frac{f_s W_n}{2}} \tag{4.5}$$

with f_s the sampling frequency and *Res* the resolution of the pressure gauge (expressed in m). The constants a_1 and a_2 have been set equal to 12 and 1.1 respectively. Moreover, f_p is the peak frequency of the pressure head density spectrum while the frequency f_T has been determined on the basis of the linear dispersion relation (see Equation 4.6). f_T represents the highest frequency at which the pressure fluctuation induced by a travelling wave can be detected at a distance d_{PT} from the mean free surface (i.e., where the PTs are placed):

$$f_T = \frac{1}{2\pi}\sqrt{g\frac{\pi}{d_{\mathrm{PT}}}\tanh\left(\frac{\pi h}{d_{\mathrm{PT}}}\right)}. \tag{4.6}$$

4.2.2 Wave climate from wind, fetch and depth data ($H_{m0,E}$)

The offshore wave climate was determined using the wave forecast model proposed by *Young* and *Verhagen* [1996] and further improved by *Breugem* and *Holthuijsen* [2007]. This model was specifically developed to estimate the wave height for a not fully developed sea in shallow water environments with limited fetches. The relationships employed to obtain significant wave height $H_{m0,E}$ and the peak period T_p are:

$$\frac{gH_{m0,E}}{U_w^2} = 0.240\left\{\tanh A_1 \tanh\left[\frac{B_1}{\tanh A_1}\right]\right\}^{0.572} \tag{4.7}$$

where $A_1 = 0.343(gh/U_w^2)^{1.14}$, $B_1 = 4.41 \cdot 10^{-4}(gF/U_w^2)^{0.79}$, and:

$$\frac{gT_p}{U_w} = 7.690\left\{\tanh A_2 \tanh\left[\frac{B_2}{\tanh A_2}\right]\right\}^{0.187} \tag{4.8}$$

with $A_2 = 0.10(gh/U_w^2)^{2.01}$, $B_2 = 2.77 \cdot 10^{-7}(gF/U_w^2)^{1.45}$. Here h, F_l and U_w are the average water depth, the fetch length and the wind speed offshore the considered marsh.

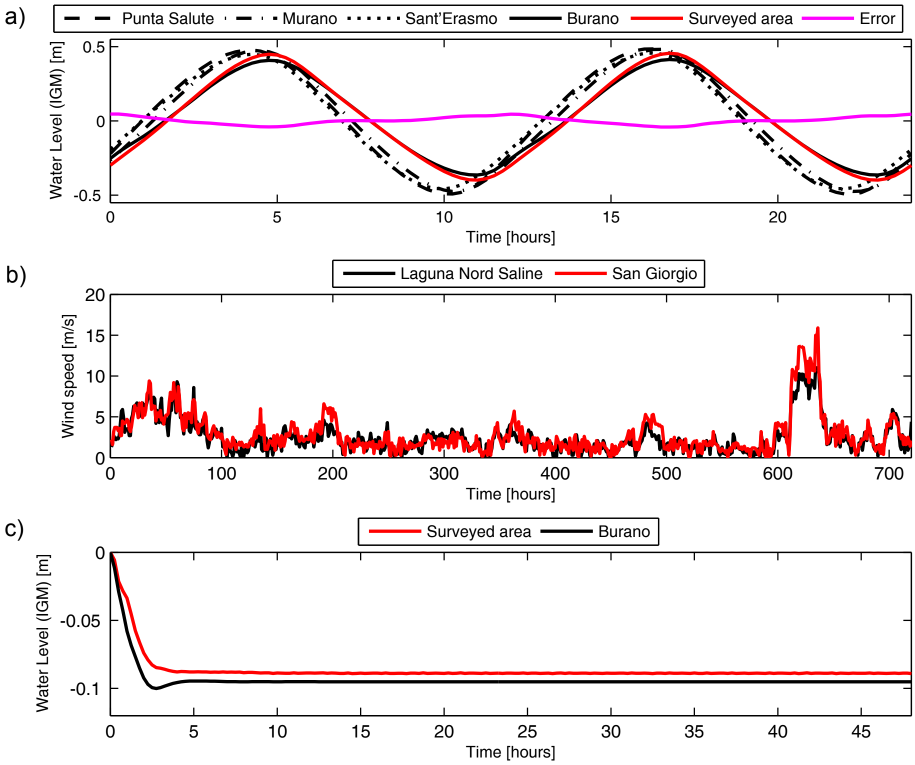

Figure 4.5: a) Time evolution of water levels computed through a finite element numerical model solving the de Saint Venant Shallow Water Equations. Water levels are referred to the reference level I.G.M. (Genova, 1942). Each line represents the time evolution of the water level at a specific location: black dashed line, Punta Salute; black dash-dotted line, Murano; black dotted line, Sant'Erasmo; black line, Burano; red line, surveyed area. Moreover, the magenta line represents the difference between the water level at Burano and nearby the monitored area. b) Comparison between the time history of wind speed observed at Laguna Nord Saline (black line) and San Giorgio (red line) monitoring stations. c) Comparison between computed water level setup induced by "Bora" wind at Burano (black line) and nearby the monitored area (red line).

For the calculations, the direction of wave propagation was assumed to adapt instantaneously to the wind direction $\theta_w(t)$. It is important to note that both the fetch and the water depth vary with wind direction $\theta_w(t)$ only. Indeed, the water depth is computed as $h(t) = \eta(t) - z_b(\theta_w(t))$, with $\eta(t)$ and $z_b(\theta(t))$, respectively the water surface elevation and the bed elevation with respect to Punta Salute. $z_b(\theta(t))$ is space averaged along each direction. Since the morphology of the investigated area is quite irregular, the values of effective fetches to be employed in the calculation was determined through the relation proposed by *Saville* [1954]:

$$F_l(\theta_k) = \frac{\sum_{s=-45}^{45} F_l(\theta_{k+s}) \cos^2\left(s\frac{\pi}{180}\right)}{\sum_{s=-45}^{45} \cos\left(s\frac{\pi}{180}\right)} \tag{4.9}$$

where $F_l(\theta_k)$ is the fetch length associated to the k-th wind direction.

Particular attention has been devoted to the choice of the water surface elevation η used to calculate the water depth $h(t)$. Hourly values of $\eta(t)$ are provided by Burano measurement station (Figure 4.1a). Even if the station is located at a distance of about 2.2 km from the monitored marsh, a quasi-steady propagation of the tidal wave was assumed [*Toffolon* and *Lanzoni*, 2010]. This assumption is supported not only by the relatively small distance between the two sites and the microtidal character of tide, but also by the analysis of the flow field in the north part of the Lagoon of Venice by means of a numerical model solving the Shallow Water de Saint Venant Equations, with particular attention to flooding and drying processes [*Defina*, 2000; *Carniello* et al., 2005].

Figure 4.5a shows the temporal evolution of the water levels computed by assuming at the inlets of the lagoon a semidiurnal tide described by the equation: $\eta_{in}(t) = A_{tide}/2\sin(\omega_{tide}t) + \Delta h_{MSL}$, with amplitude $A_{tide} = 1$ m, frequency $\omega_{tide} = 1.45 \cdot 10^{-4}$ rad/s (equivalent to a period of 12 hours) and mean sea level with respect to IGM reference (Genova, 1942) $\Delta h_{MSL} = 0.065$ m. The simulated conditions are among the most critical in term of water level difference between the Burano station and the monitored area. The considered tidal amplitude, in fact, is on average exceeded once a year. Nevertheless, the difference in water levels reaches maximum values of about 2–3 cm related to the crest and trough of the tidal wave, namely when the marsh is completely submerged or when the low water level prevents waves from reaching the marsh boundary. As a consequence, the error associated with the assumption of a quasi-steady propagation of the tidal wave does not affect significantly the estimate of wave height that promotes marsh erosion.

The wind data employed in Equations 4.7 and 4.8 were collected at the monitoring stations of Laguna Nord Saline and San Giorgio (Figure 4.5a). The investigated marsh is located between these two stations, along the direction of the "Bora" wind. Average values of wind velocities measured at the two stations have thus been used. Figure 4.5b shows two examples of temporal sequences of hourly wind data provided by the two measurement stations. It clearly appears that the two data sets almost overlap.

Wind induced setup may also influence the difference in water level at the investigated area and at the monitoring station of Burano where the water levels are measured. To estimate this effect, a numerical simulation was carried out, in which water level in the lagoon is forced by a north-east wind of 12 m/s. Figure 4.5c shows that the maximum difference of the water levels between Burano and the monitored area, is around 1 cm. Hence, the water levels measured at the Burano station allow a robust estimation (through Equations 4.7 and 4.8) of the offshore wave climate $H_{m0,E}$, in front of the investigated salt marsh.

4.2.3 Erosion rates

Erosion was measured by means of erosion pins placed horizontally at different heights along the bank scarp and, at different position of the marsh shoreline, spaced laterally about 2 meters (Figure 6a and 6b).

Table 4.3: Number of deployed pins per each sector in which the marsh edge has been divided according to the mean edge orientation and the possible influence of boat-induced waves.

Sector 1	Sector 1a	Sector 1b	Sector 2	Sector 3	Sector 4
18	3	3	7	14	20

Table 4.3 summarizes the number of pins employed per each sector. The erosion length, L_{er} (Figure 4.7), has been defined as the local retreat for each pin (expressed in cm) with respect to the previous survey, and, therefore, measures the extent of erosion occurred within the time span between two consecutive surveys. When the observed retreat length resulted in the range 0.0–1.0 cm, L_{er} was set equal to 0.5 cm.

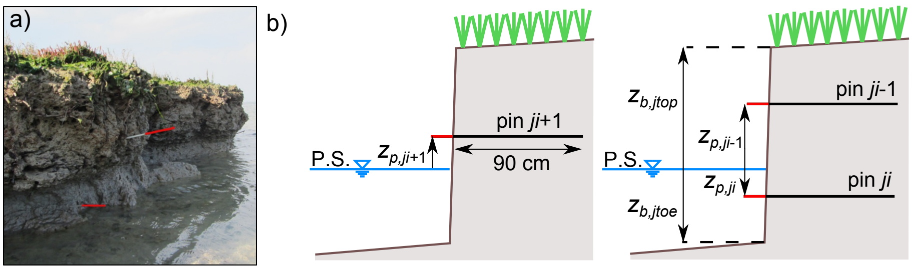

Figure 4.6: a) View of two erosion pins located on the same vertical line for the j-th sector. b) Sketch representing the possible placement of erosion pins: $z_{p,ji}$, $z_{b,jtoe}$ and $z_{b,jtop}$ are, respectively, the elevations of the i-th pin, the bank toe and the bank top with respect to the reference level of Punta Salute (measurements are obtained by means of an electronic distance sensor).

All the times a mass failure occurred and the pin remained inserted in the slumped block, the eroded length was set equal to the width of the block. The pin was then reinserted in the marsh bank according to the selected elevation. The positions of the bank top, bank toe and pin elevation with respect to Punta Salute were determined through an electronic distance transducer (model Wild/Leica 2002, accuracy 1 mm + 1 ppm), after a datum point on the salt marsh was identified through GPS measurements.

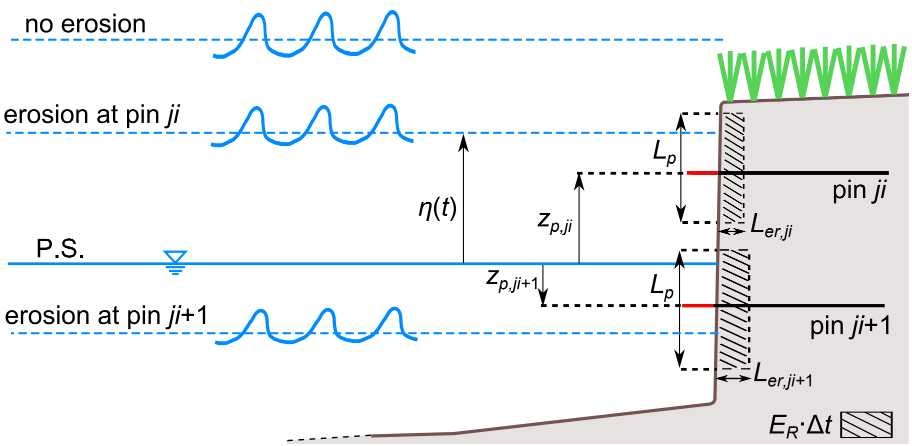

Figure 4.7: Sketch of the procedure employed to compute the eroded area and the erosion rates for the j-th sector. $z_{p,ji}$ and $z_{p,ji+1}$ are the elevations of the pins ji and $ji+1$ with respect to the reference level of Punta Salute (P.S.); L_p is the bank thickness subject to erosion associated to each pin; η is the water level with respect to Punta Salute; $L_{er,ji}$ and $L_{er,ji+1}$ are the erosion lengths measured at pins ji and $ji+1$ respectively; the black dashed area represents the volumetric erosion per unit length of the marsh boundary (m^3/m).

The erosion rates $R_{sc,ji}$, expressed in m^2/yr, were evaluated by considering a vertical section of the bank, containing at least one pin (Figure 4.7). First, the eroded cross sectional area is calculated as $L_{er,ji} \cdot L_p$ (black dashed portion in Figure 4.7); then the erosion rate is estimated by dividing this area by the time interval Δt during which erosion occurred, due to the action of the waves striking the portion of the marsh bank associated to the considered pin. The time interval Δt_{ji} (hours), associated to the i-th pin located in the j-th sector, is determined through the relation:

$$\Delta t_{ji} = \int\limits_{\Delta T} g^{\eta}_{ji} \cdot g^{\theta}_{j} \cdot g^{P_w} \, d\tau \tag{4.10}$$

where ΔT (hours) is the time span between two consecutive surveys, and the generalized functions g^{η}_{ji}, g^{θ}_{j}, g^{P_w} account for the time intervals during which the pins are subjected to the wave action. In particular,

$$g^{\eta}_{ji} = \begin{cases} 1 & \text{if } z_{ji} - L_p^{\text{down}} \leq \eta(t) \leq z_{ji} + L_p^{\text{up}} \\ 0 & \text{otherwise} \end{cases} \tag{4.11}$$

with $L_p = L_p^{\text{down}} + L_p^{\text{up}}$ ($L_p^{\text{down}} = L_p^{\text{up}} = 15$ cm) the vertical extension of the slice of bank around a given pin over which the waves exert their erosive action;

$$g^{\theta}_{j} = \begin{cases} 1 & \text{if } \theta(t) \in \Delta\theta_j \\ 0 & \text{otherwise} \end{cases} \tag{4.12}$$

where $\Delta\theta_j$ is the wind directions range potentially influencing the j-th sector where the pin is located;

$$g^W = \begin{cases} 1 & W > 0 \\ 0 & \text{otherwise} \end{cases} \tag{4.13}$$

where W is the hourly wave energy flux (see Section 4.2.4).

The erosion rate $R_{sc,j}$ (m^2/yr) associated to the j-th sector is computed as:

$$R_{sc,j} = \frac{1}{N_{p,j}} \sum_{i=1}^{N_{p,j}} \frac{24 \cdot 365}{\Delta t_{ji}} L_{er,ji} L_p \tag{4.14}$$

with $N_{p,j}$ the number of pins placed in the j-th sector.

4.2.4 Wave energy flux

Wave energy flux is determined by linear wave theory as:

$$W = E \cdot c_p \cdot n \tag{4.15}$$

in which:

$$E = \frac{1}{16} \rho g H_{m0}^2 \tag{4.16}$$

ρ is the water density, c_p is the phase velocity, $n = \frac{1}{2}[1 + \frac{2kh}{\sinh(2kh)}]$ and k is the wave number associated with the peak wave frequency $\sigma_p = \frac{2\pi}{T_p}$. The significant wave height H_{m0} impinging the marsh bank is determined on the basis of the functional relation obtained by a linear regression between the significant inshore wave height $H_{m0,M}$, measured in front of the marsh during three storm surges, and the corresponding estimated wave height $H_{m0,E}$, predicted by the model of *Breugem* and *Holthuijsen* [2007] (see Section 4.3). Wave power is calculated hourly from the values of $H_{m0,E}$ and T_p on the basis of hourly data provided by various measurement stations within the lagoon of Venice (Figure 4.1a). The "effective" wave energy flux striking the j-th sector for a specific interval of time ΔT is obtained from:

$$W_j = \frac{1}{N_{p,j}} \sum_{i=1}^{N_{p,j}} \left[\frac{1}{\Delta t_{ji}} \int_{\Delta T} W(\tau) \cos(\theta - \theta_{n,j}) \cdot g_{ji}^{\eta} \cdot g_j^{\theta} \cdot g^{P_w} \, d\tau \right] \tag{4.17}$$

with $\theta - \theta_n$ the angle that wind direction forms with the normal to the average orientation of the j-th sector.

4.3 Results

4.3.1 Wave power and erosion rate

The measurement of wave climate close to the edge of the marsh during three storm surges allowed the definition of a functional relation between the measured and estimated values of the significant wave height $H_{m0,M}$ and $H_{m0,E}$ through the calibration of relations 4.7 and 4.8 [*Breugem* and *Holthuijsen*, 2007]. This calibration requires that the values of $H_{m0,M}$ and $H_{m0,E}$ refer to the same temporal frame. Since measured values have been collected every 1.5 hours while estimated values are computed at intervals of 1.0 hour, input data to Equations 4.7 and 4.8 are linearly interpolated at the time instants corresponding to measured wave heights. Figure 4.8 shows the scatter plot of estimated and measured wave heights.

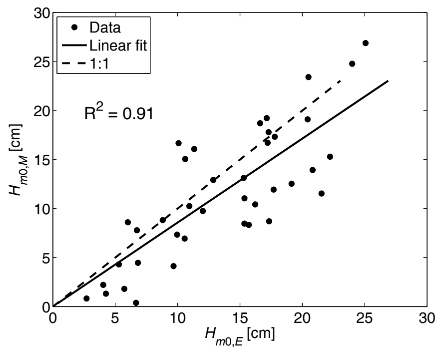

Figure 4.8: Relation between measured wave height $H_{m0,M}$ and estimated wave height $H_{m0,E}$. Black circles represent the scatter plot between $H_{m0,M}$ and $H_{m0,E}$. Black continuous line is the linear regression of $H_{m0,M}$ on $H_{m0,E}$. Black dashed line is the 1:1 line..

Linear regression among data yields:

$$H_{m0,M} = 0.87 H_{m0,E}. \tag{4.18}$$

with a correlation coefficient $R^2 = 0.91$. This relation is then used to determine the wave energy flux through Equation 4.17.

The cumulative average retreat per sector, expressed in (cm), is depicted in Figure 4.9. To calculate this, in case the mass failures are not accounted for, the erosion pin interested by the failure was removed from the calculation. Sector 4 was subject to the highest retreat, which strongly increases when also mass failures are included. Indeed, in such a case, the final retreat almost doubles for sectors 2 and 4. The time span covered during the surveys is roughly one year and the yearly retreat range ranges from 18 to 80 cm/yr.

Figures 4.10 and 4.11 show the scatter plot of W_j versus $R_{sc,j}$ for the various sectors in which the marsh edge has been subdivided, by either excluding or

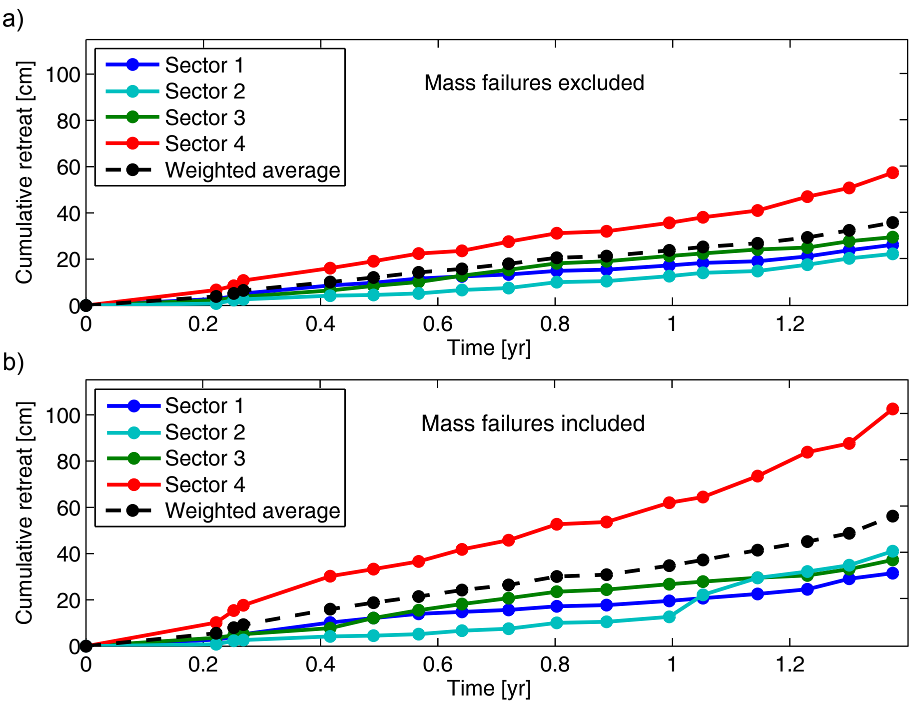

Figure 4.9: Cumulative average retreat (in cm) observed in sectors 1, 2, 3 and 4 and average retreat weighted on the number of pins per each sector, by either considering (a) or excluding (b) mass failures.

including mass failures from the analysis. This means that, in the first case, the erosion length associated to a specific interval is not considered in the mean erosion of the sector when the mass failure is present. Conversely, for the analysis including mass failures, the average erosion at a sector for a specific interval is calculated accounting also for the dimension of the failed block. In both cases field surveys number 2 and 3 were removed from the analysis because of the small interval of time ΔT elapsed between two consecutive surveys; similarly, records 1 and 4 are not considered because of too long ΔT. Note that sectors 1a and 1b, owing their peculiarities discussed in Section 4.3.2, do not show a clear correlation between wave energy flux and erosion rate and, hence, the related scatter plots are not reported in Figures 4.10 and 4.11.

The analysis carried out excluding mass failure events (Figure 4.10), indicates a relatively high correlation ($R^2 = 0.73$–0.77) for sectors 1–3, with an almost linear trend exhibiting slightly different values of the slope and intercept with the x-axis. The lower correlation ($R^2 = 0.54$) for sector 4 (Figure 4.10d) is likely due to the high occurrence frequency of mass failures in this sector. Possibly, blocks slumped at the beginning of an observation interval (and hence not completely removed when the subsequent field survey was carried out), provided a defence for the bank against wave attack. Indeed, the value of the

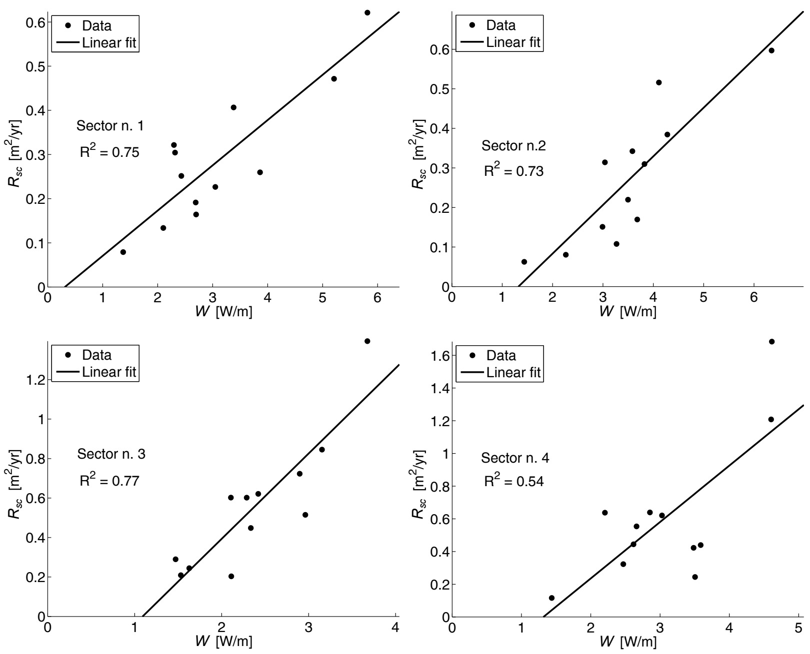

Figure 4.10: Scatter plots between wave energy flux, W_j, and erosion rate, R_{sc}, observed in sectors 1, 2, 3, 4. Mass failures are not considered in the determination of erosion rates. Black continuous lines represent the linear regression among data (black dots).

correlation coefficient is quite similar to those reported in Figure 4.11, where the scatter plots include also data with mass failures. In particular, the correlation coefficient is quite low for sector 2. The lower correlations observed when failure events are accounted for, can be explained by recalling that this type of erosion is not immediately correlated to the wave energy flux at the time scale of months. Indeed, a period characterized by intense wave forcing, preparing bank morphology to a mass failure, can be followed by a more calm period during which the failure occurs. If the field surveys identify such periods as two different intervals, a poor correlation is clearly found between wave energy flux and erosion rates. A recognizable, although weak, linear trend, can be observed even including mass failures, provided their frequency is relatively high. In this case, slumping events tend to increase globally the erosion rates (Figures 4.11c and d) with respect to the case they are not accounted for in the determination of the erosion rate (Figures 4.10c and d).

Figure 4.12 compares the trends obtained by either including or excluding mass failures from the analysis. In general, block slumping leads to a strong increase of the average erosion rates in each sector. In addition, the insert in Figure 4.12 suggests the existence, at least for three of the four sectors analysed, of a threshold value of the average wave power for erosion to occur, ranging

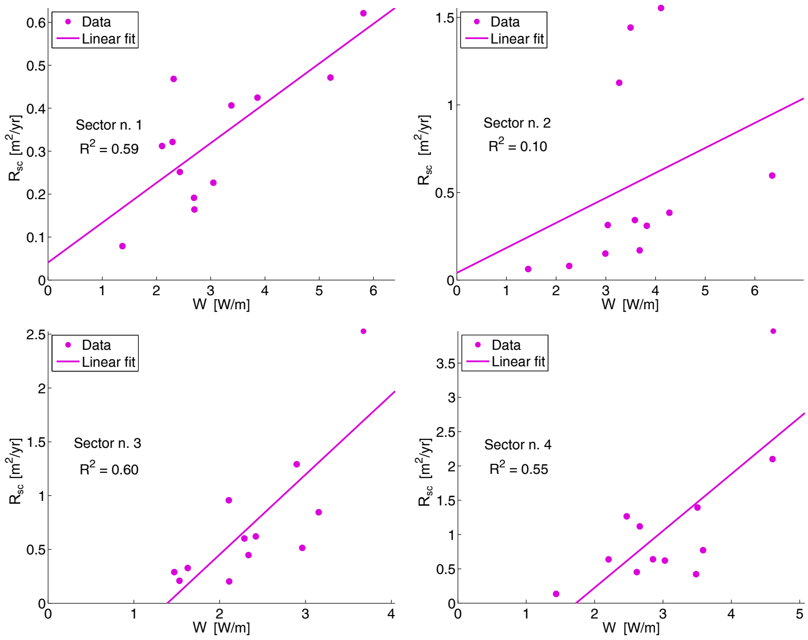

Figure 4.11: Scatter plots between wave energy flux, W_j, and erosion rate, R_{sc}, observed in sector 1, 2, 3, 4. Mass failures are included in the determination of erosion rates. Magenta continuous lines represent the linear regression among data (magenta dots).

about 1–2 W/m.

The effect of wave attack at different levels along the scarp of the salt marsh edge is investigated in Figure 4.13. The average of the ratios of erosion rates $R_{sc,ji}$ was compared to the average wave energy flux W_{ji} among groups of pins located at the same elevation range k (Figure 4.13a) with respect to the bank toe. In particular, four different elevation ranges have been considered along the bank scarp normalized with its overall height (Figure 4.13a). The ratio m_k for the k-th range is determined as:

$$m_k = \frac{1}{N_k} \sum_{i \in \text{range}(k)} \frac{R_{sc,ji}}{W_{ji}}. \tag{4.19}$$

Figure 4.13b shows the values attained by m_k by either considering or excluding mass failures. In general m_k tends to increase in the lower portion of the bank scarp. This result implies that a given value of the wave power promotes a higher erosion rate at the toe of the bank with respect to the top. Mass failure events, however, tend to increase m_k also in the upper part of the bank, determining an higher standard deviation, as a consequence of the reduced correlation between wave energy flux and erosion rates discussed above.

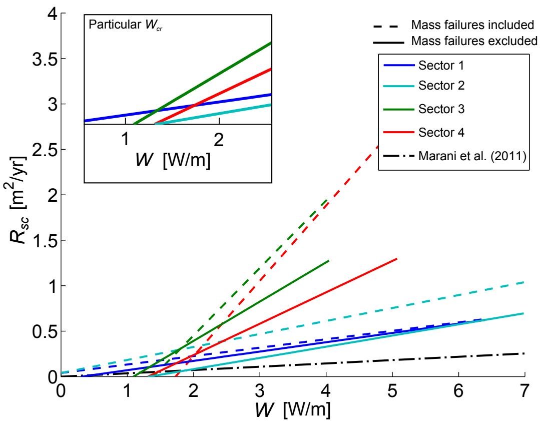

Figure 4.12: Linear trends between wave energy flux W and erosion rate R_{sc} for sectors 1, 2, 3 and 4 (blue, black, red and magenta lines) in case mass failure are either excluded (continuous line) or included (dashed line) in the analysis. The linear trend proposed by *Marani* et al. [2011] is also reported (black dashed line). This trend has been reported on the basis of a global analysis of the marsh retreat within the Lagoon of Venice, carried out at the time scale of decades of years.

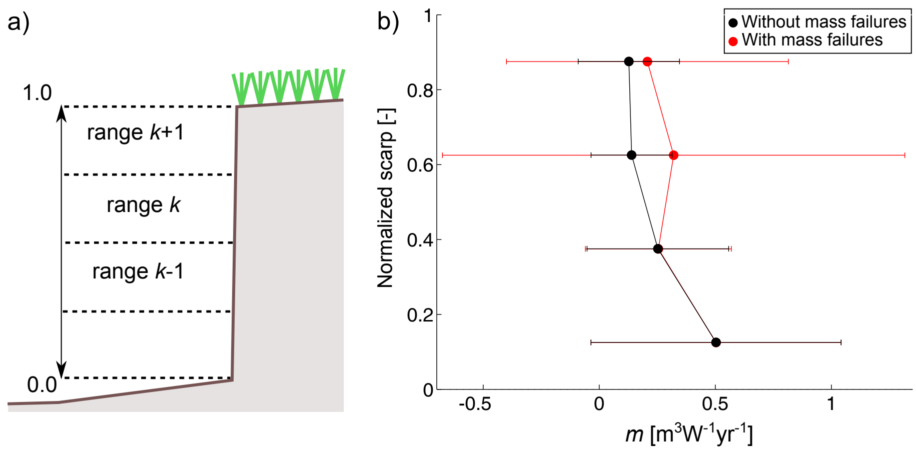

Figure 4.13: a) Sketch of the framework employed to determine the average ratio m of erosion rate to wave energy flux for pins located within the same elevation range along the scarp. b) Plot of the m by either considering (red dots) or excluding (black dots) mass failures. Error bars correspond to one standard deviation.

4.3.2 Critical discussion

The results of the field measurement campaign are discussed below, with particular reference to the erosive effect of mass failures, possible contribution to erosion of boat-induced waves, as well as the influence of the time and spatial scales on the relationship between wave energy flux W and erosion rate R_{sc}.

Figures 4.10 and 4.11 show the behaviour of only four of the six surveyed sectors (i.e., sectors 1, 2, 3 and 4). Sectors 1a and 1b are, in fact, characterized by a lack of correlation between erosion rate and wave energy flux. This result can be firstly explained by too small number (three) of erosion pins used to characterize the erosive trend in these sectors. Indeed, the height of marsh banks in such sectors is really small (around 30–40 cm). Furthermore, the bathymetry of the area up to 20–30 m in front of the salt marsh bank implies really shallow depths until the bank is submerged, thus leading to a small wave energy flux. In other words, the wave energy flux reaching the bank, due to the influence of the local morphology, can be much smaller than the wave power determined from bathymetric data characterizing the offshore mudflats. This strong difference between inshore and offshore bathymetry was not affecting the other salt marsh sectors. In addition, the orientation of the boundary of sectors 1a and 1b makes them particularly protected and a restricted wind directions span can directly affects the marsh edge.

As already pointed out, sector 4 shows the lowest value of the correlation factor R^2. This result can be attributed to the high frequency of mass failures in this sector: slumped blocks, before their complete removal, act as a partial defence barrier against wave attack. As a consequence, high values of the wave energy flux may not be correlated to high erosion rates. This is partially in agreement with the results obtained by *Leonardi* and *Fagherazzi* [2014], which show the difficulty to predict failure events for sites exposed to low wave forcing. Indeed, wave energy fluxes reaching the monitored marsh are relatively low with respect to the values of wave power considered by *Leonardi* and *Fagherazzi* [2014]. This is due to the larger fetches associated to the analysed area (Plum Island Sound, Massachusetts, and Virginia Coast Reserve, Virginia, USA) with respect to the monitored marsh in the Lagoon of Venice.

It is possible to argue that the occurrence of many occasional mass failures is responsible of the low correlation among data shown in Figure 4.11 for sector 2. For sectors 3 and 4 a linear trend is still recognizable, since mass failures occurred only once for each time interval between two consecutive surveys. Failure events involved blocks with size in the direction orthogonal to the bank edge in the range of 40–70 cm, increasing considerably the average erosion rate associated to the specific interval.

The relation between W and R_{sc} might be also affected by the presence of boat-induced waves. In the analysis, it is implicitly assumed that the wave energy flux causing erosion is only due to wind waves. Nevertheless, sectors 4 and 3 are potentially subject to boat waves coming from west and north-west directions. This might be one reason for the higher erosion rates exhibited by sectors 3 and 4 with respect to the sectors 1 and 2 (Figure 4.12). Unfortunately, none of the monitored time intervals was characterized by negligible wind-wave forcing, thus making it impossible to quantify the effect of boat-waves only. A further possible explanation for the higher erosive trends observed in sectors 3 and 4, as compared to sectors 1 and 2, is related to the presence of a shallower mudflat just in front of the latter sectors. As a consequence, the wave power, estimated with a spatially averaged value for offshore water depth in front of the sector, turns out to be partially reduced as it reaches the bank. The wave energy flux is then somehow slightly overestimated.

The data reported in Figures 4.10 and 4.11 are characterized by values of the intercepts of regression lines with the abscissa in the range 1–2 W/m, except for sector 1. This result suggests the existence of a threshold for the onset of erosion, W_{cr}, due to wave impact. It seems then that particle aggregates are likely detached from the bank also for a relatively low average wave energy flux. However, it is important to stress that W_{cr} is based on monthly averaged values of the wave energy flux and it does not represent an instantaneous quantity. This value of the erosion threshold is similar to that suggested by *Mariotti* and *Fagherazzi* [2010] (equal to 3 W/m) at least for the time scale involved in the present study. However, it is possible that at lower time scales the erosion threshold might be different due to the different averaging interval employed to determine the wave energy flux. In other words, the sampling interval can affect the determination of the erosion rate; moreover, it can also influence the rate of sediment transport [*Singh* et al., 2009]. The fact that sector 1 does not exhibit such a threshold may be explained by its location near the inlet of a deep tidal channel. Current induced shear stresses can provide a significant additional forcing inducing erosion even in the absence of surface waves.

It is worth to stress that our analysis focused specifically on a monthly time scale for the determination of the relation between wave power and erosion rate. Comparison of present results with those obtained by *Marani* et al. [2011] (Figure 4.12), on the basis of a time scale of the order of decades, suggests that the rates of erosion emerging from our datasets are higher. The main reason for this difference can be associated with the different time scales considered in the analyses. The erosion rates obtained by *Marani* et al. [2011] have been estimated by considering several sites in the lagoon of Venice and comparing aerial photos acquired in 1970, 1995 and 2004. An average retreat was found by comparison, which was then multiplied by the bank eight to recover a volumetric erosion per unit length of the marsh boundary (m^3/m), with the same dimension of $R_{sc} \cdot \Delta t$. The determination of the time span during which the erosion occurred, included all the water levels except when the marsh was submerged. This means, in order to determine the erosion rate, they divided the eroded volume per unit length (m^3/m) by a larger Δt, in proportion, with respect to our study, possibly leading to lower average erosion rates. This result is not surprising and is similar to the results obtained by *Singh* et al. [2009] in case of bedload transport, where the authors showed the scale dependence of sediment transport on sampling rate.

Figure 4.12b suggests that the lower portion of the marsh bank is more prone to erosion than the higher part. This behaviour may have a twofold explanation. On the one hand, the presence of the root mat due to the vegetated cover, can increase the resistance to erosion of the upper part of the bank [*Van Eerdt*, 1985a; *Chen* et al., 2012; *Tuan* and *Oumeraci*, 2012]. On the other hand, the effect of wave forcing on bank scarp might be differently affected by wave hydrodynamics. Let us assume, for the sake of simplicity, an equivalent wave energy flux impinging the top and the toe of the bank. This ideal case neglects the effect of lower average water depth, which reduces the wave height reaching the bank, all other things being equal. When the mean water level reaches the bank top, wave energy is partially reflected and wave breaking does not necessarily occurs. Conversely, when the mean water level is around the lower part of the bank scarp, waves generally break before impacting the bank, leading to a higher turbulence intensity and negligible wave reflection. Consequently, it is possible to argue that the erosive power of the waves is much larger with respect to that characterizing the partially reflective wave pattern occurring for higher mean water levels. In any case, erosion appears to be much stronger at the lower part of the scarp, thus explaining the prevalence of a cantilever type profiles which, in turn, promote mass failure events.

A specific discussion is required regarding the adopted methodologies to collect erosion and wave climate data. Erosion was measured by means of erosion pins located horizontally on the bank and it was necessary to accurately read the eroded material on the rigid rod. Electronic devices like photo-electronic erosion pins (PEEP) would have been more appropriate but a cost of an increased complexity to be managed, whereas the use of laser scanner to survey all the area would not allow frequent surveys. A possible improvement would be the use of a larger number of erosion pins together with a statistical analysis of the measurement errors. This would lead to a range of expected erosion rates in order to better estimate the magnitude of the process. Wave climate was measured occasionally and the wave height during all the measurement period was extrapolate through an empirical relation. The use of a wave generation and propagation model does not seem suitable for the really short fetches and the most appropriate choice would be the deployment of a permanent measurement station in the field.

4.3.3 Modelling the effect of cantilever failures on cumulative bank retreat

Inspired by the different erosional behaviours of the sectors and by the non-uniform erodibility of the bank scarp, a simple mathematical model describing the retreat mechanism of the salt marsh edge is developed.

The model is based on the different bank erodibilities along the vertical direction of the scarp, of height b_h. A simple cross-shore profile, as depicted in Figure 4.14, is considered. The bank is divided in an upper and a lower part characterized by the erodibilities m_{top} and m_{toe} and the lower part is located at an elevation $\hat{d}$ from the adjacent mudflat. The bank is subject to continuous wave forcing modulated by the tide (approximate to a semidiurnal tide with period T_{tide} equal to 12 hours). The upper part is eroded when the water surface elevation with respect to the toe of the bank $\hat{\eta}$ falls between $z_{b,avg}$ and $z_{b,avg} + \Delta L_{top}$, whereas the lower part is eroded when water level falls between $z_{b,avg} - \Delta L_{toe}$ and $z_{b,avg}$, furthermore, $\Delta L_{toe} = \Delta L_{top} = b_h/2$ (see Figure 4.14). $z_{b,avg}$ is the elevation of the horizontal surface which separates the upper and the lower part of the bank. x_{top} and x_{toe} indicate the positions of the upper and lower portion of the scarp in transverse direction, respectively, and $x_{avg} = \frac{1}{2}(x_{top} + x_{toe})$. To test the effect of the continuous wave forcing, two different values of wave height are investigated ($H_{rms} = 10$ cm and $H_{rms} = 20$ cm). Wave energy flux W is computed by linear theory and the retreat is due only to wave impact, indeed, the effect of shear erosion is neglected. The cumulative retreats of the two portions of the bank are calculated as:

$$x_{top}(t + \Delta t) = x_{top}(t) + \frac{m_{top} W}{\Delta L_{top}} \Delta t \tag{4.20a}$$

$$x_{toe}(t + \Delta t) = x_{toe}(t) + \frac{m_{toe} W}{\Delta L_{toe}} \Delta t. \tag{4.20b}$$

Different simulations are run changing the ratio m_{toe}/m_{top}. With reference to Figure 4.14, the other parameters kept fixed for the simulations are listed below: $H_{rms} = 10, 20$ cm; $T = 1.5$ s; $A_{tide} = 1$ m; $T_{tide} = 12$ hours; $b_h = 0.8$ m; $\hat{d} = 0.4$ m.

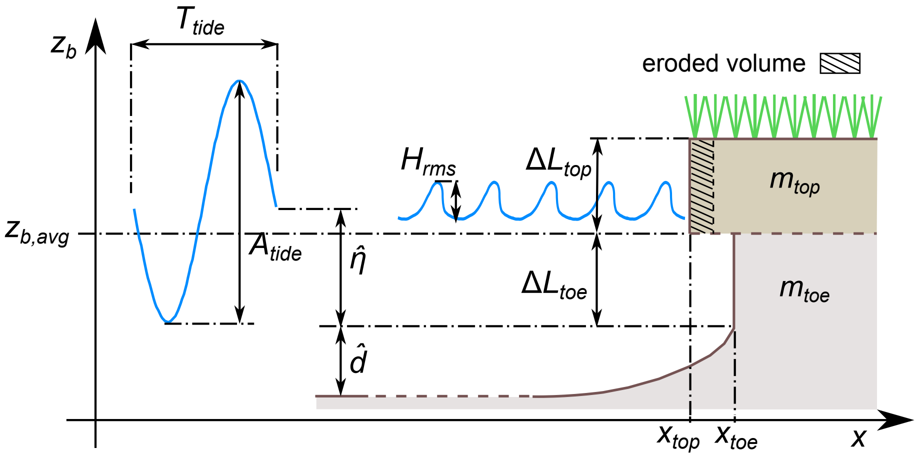

Figure 4.14: Sketch of the bank retreat model due to cantilever failures.

During the simulations, x_{toe} and x_{top} retreat at different rates. When $x_{top} - x_{toe}$ exceeds a given threshold s_{max}, here assumed equal to 0.5 m, then mass failure occurs. The value of s_{max} is chosen to be representative of the length of the slumped blocks observed in the field. Once mass failure occurs, the value of x_{toe} is increased of 0.5 times the length of the failed block as proposed by *Gabet* [1998]. This assumption is made in order to consider both that the slumped blocks can be more easily eroded, and they provide only a limited protection to the bank toe.

Figure 4.15 reports the ratio between the cumulative lateral retreat x_{avg} and $x_{avg,eq}$, as a function of the ratio m_{toe}/m_{top} after around 730 tidal cycles (i.e. one year). The value of the equivalent cumulative lateral retreat $x_{avg,eq}$ is obtained by running the model considering a uniform value for the scarp erodibility, equal to the average between m_{top} and m_{toe}. Circles and crosses in different colours represent the output of the model in case m_{toe} and m_{top} are referred to sectors 1, 2 and 4. Sector 3 was excluded due to the limited number of erosion pins installed on the lower portion of the bank.

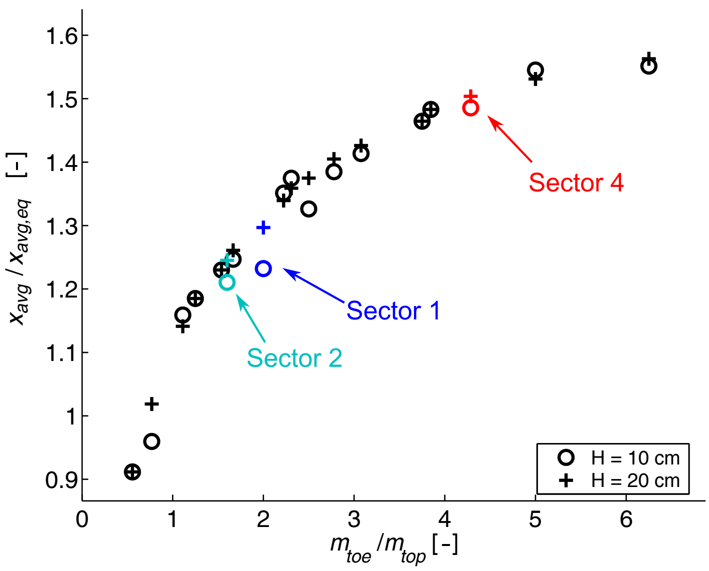

Figure 4.15: Ratio of the cumulative retreat x_{avg} to the equivalent cumulative retreat $x_{avg,eq}$ as a function of the ratio m_{toe}/m_{top}, after 730 tidal cycle (black circles: $H_{rms} = 0.10$ m; black crosses: $H_{rms} = 0.20$ m). Colored markers are associated to values of m_{top} and m_{toe} of sector 1 (blue), sector 2 (light blue) and sector 4 (red).

Results show that increasing the difference of erodibility along the scarp of the salt marsh, lead to an increase of cumulative lateral retreat with respect to the equivalent case in which erodibility is uniformly distributed along the vertical profile. The process of cantilever formation and subsequent failure may increase up to the 60% the cumulative lateral retreat, provided that the simulation lasts the time necessary to mass failure events to occur. For $H = 10$

cm, the trend seems more scattered. This can be ascribed to the fact that during the same time interval, less mass failures occurred. In particular, those banks with larger values of the ratio m_{toe} to m_{top}, display a greater retreat since mass failures may occur more often.

The results of the model can explain in part why the sector 4 experienced a higher cumulative retreat with respect to the others. Even if the average erodibility (i.e. the ration between erosion rate and wave power) of sector 4 is higher than sector 1 and 2, this effect is further emphasized due to a higher ratio m_{toe} to m_{top}.

Present finding, even if obtained by a simplified model, may have several implications on the lateral evolution of salt-marshes. Banks with a relative more erodible toe layer are potentially subject to higher retreats due to effect of mass failures (in this case of cantilever type). Furthermore, different vertical erodibility may be due to the presence of vegetation which increases the cohesion of the top layer of soil via the root system, this suggests that vegetation does not necessarily guarantee the lateral stability of salt marshes. Indeed, while vegetation can have a positive role to locally decrease the proneness to erosion [*Howes et al.*, 2010; *Chen et al.*, 2012; *Tuan and Oumeraci*, 2012], present results suggest that vegetation by itself may be not sufficient to ensure, globally, a reduction of lateral erosion.

4.4 Summary and concluding remarks

Field measurements have been carried out in a salt marsh located in the northern part of the Venice Lagoon in order to investigate the effects of wind waves on the retreat mechanism of the marsh edge and a simple mathematical model to interpret field data has been developed. Wave height measurements coupled with inshore wave climate estimates based on offshore wind, fetch and depth data were employed to relate the wave forcing at the monitored marsh to the bank erosion rate.

Global average retreat rates, reaching up to 70–80 cm/yr, are usually different among sectors due to the different wind exposure, the local bathymetric features and the possible influence of boat-induced waves and the localized dynamics controlled by the non-uniform erodibility of the scarp. The effect of occasional mass failures can almost double the average retreat rate for a specific sector. Indeed, the sector which experienced the major number of failures, is associated to high erosion rate and the highest cumulative global retreat

A clear correlation between wave energy flux and erosion rate, at short (monthly) temporal scales, can be found when mass failure events are excluded from the analysis. Including mass failure events, leads to a linear correlation between wave energy flux and erosion rate only if episodes of mass collapse are frequent. In general, the slumping of unstable blocks is, in fact, not necessarily correlated to the instantaneous wave forcing. An unstable bank configuration is usually enhanced by adverse wave attack, but the final mass failure may occur later on, during a more calm period. Values of erosion rates are generally higher than those obtained when averaging over much larger time intervals. The problem associated with the choice of a suitable sampling time turns out to be similar to that emerging in bedload transport, whereby mean sediment transport appears to be dependent on the sampling time.

The formation of cantilever profiles, generally present in the field, can be explained by the higher propensity to erosion of the lower part of the bank scarp with respect to the top. This result is likely due to the presence of the root mat in the upper bank portion as well as to the local characteristics of the flow field. Partial wave reflection and the reduced occurrence of wave breaking when the water level is around that of the bank top lead to a lower erosion potential.

A simple mathematical model, based on the differential proneness to erosion of the scarp of the salt marsh, showed that a great erodibility of the toe layer of the bank, under certain conditions, may lead to higher cumulative retreat, as compared to the equivalent case in which erodibility is uniformly distributed along the vertical profile. A stronger top layer might promote the formation of cantilever profiles, which in turn may lead to more frequent mass failure events.

Clearly, the obtained results are not exhaustive. Various aspects of the erosive process acting on the marsh edge merits to be further investigated. The effect of a single storm surge on bank morphology should be assessed through surveys carried out immediately before and after a strong storm event. The role of soil composition should also be investigated by means of soil samples collected at different locations on the monitored marsh. Role of boat-induced waves should be better quantified, so that its relative contribution to the erosion rate can be considered. Finally, the influence of different vegetation covers needs to be taken into account in the next studies. Important aspects to be accounted for are related to the number of pins employed and the wave height measurements. A larger number of erosion pins would useful to reduce the uncertainty in the measurements, and the employ of photo-electronic erosion pins (PEEP) might give a continuous information on the erosive trend. Wave height measurements could be further improved by the installation of a permanent station, provided that an adequate protection is installed to avoid damages due to extremely high tide and storm surges.

This notwithstanding, the present findings are fundamental not only for prediction purposes, but also for developing and validating bank erosion models.

Chapter 5

Morphodynamic Modelling of a 1-D Salt Marsh Bank Profile

In this chapter the modifications to the hydro-morphodynamic model XBeach [*Roelvink* et al., 2009] are described and the results obtained with the modified version of the model are presented.

The main objective is to develop a numerical tool able to describe the erosion of a cross section of a salt marsh bank at the time scale of days and months, including the time evolution of the system by varying the soil composition and accounting for the effect of vegetation. The obtained tool can be applied as an exploratory model to investigate the effect of possible changes of the main parameters such as soil composition, or the presence of vegetation, on the final results. Since the focus is put on the bank profile, the 1-D version of XBeach is applied in this work.

In the first section, the structure of the current version of the XBeach model is reported. The subsequent section is dedicated to the modifications implemented in the model. Results from numerical experiments are reported in the third section. In the last section, the conclusions and recommendations for possible future developments are drawn.

5.1 XBeach model

XBeach is a numerical model developed to describe the effect of storm surges on dune erosion [*Roelvink* et al., 2009]. In this section, the model is described but only the processes implemented in the numerical code which are relevant to the present study are reported. The employed version of the model is the "2012-04-06-XBeach-v19-Easter", freely downloadable from the Deltares website[1]. The structure of the model is reported in Figure 2.5 (Chapter 2).

[1]http://oss.deltares.nl/web/xbeach/home

5.1.1 Hydrodynamics

Hydrodynamics in XBeach can be described by two different approaches.

The first approach couples short waves and induced long waves and currents by solving respectively the wave action balance equation [*Hasselmann* et al., 1973; *Booij* et al., 1999] (Equation 2.3) and the NSWE (Nonlinear Shallow Water Equations, Equation 2.1). In XBeach the directional distribution of the action density is considered, whereas the frequency spectrum is represented by a single wave frequency. This approach (phase-averaging) requires less computational efforts but it cannot directly simulate the processes related to single wave scale.

The other approach (phase-resolving) directly solves the NSWE with a pressure correction to account for the non-hydrostatic behaviour of the flow. Due to its features, it implicitly accounts for wave steepening, swash process, wave reflection at the bank scarp and sediment transport at single wave scale, and is therefore computationally more expensive than the phase averaged approach. This is the main reason why the phase-averaged approach will be initially adopted.

XBeach is a nearshore model, as a consequence, only dissipative terms contribute to the source term S_{tot} in the action balance equation. These terms are: wave energy dissipation rate per direction due to bottom friction D_b^*, due to wave breaking D_{br}^* and due to the presence of vegetation D_{veg}^* (integration over directions gives, respectively, D_b, D_{br} and D_{veg}). The dissipation rate due to breaking is further used as a positive source term for the roller energy balance equation which reads [*Roelvink* et al., 2009]:

$$\frac{\partial E_r^*}{\partial t} + \frac{\partial c_{r,x} E_r^*}{\partial x} + \frac{\partial c_{r,y} E_r^*}{\partial y} + \frac{\partial c_\theta E_r^*}{\partial \theta} = -D_r^* + D_{br}^* \tag{5.1}$$

where $c_{r,x} = c_p \cos\theta + u_L$, $c_{r,y} = c_p \sin\theta + v_L$ and c_θ are the propagation velocities in the respective directions and D_r^* is the roller energy dissipation rate per direction (integration over directions gives D_r).

Several models can be used in XBeach to describe the wave breaking process. In this study, the value of the energy dissipation rate due to breaking D_{br} is calculated through the formulation proposed by *Janssen* and *Battjes* [2007] and *Alsina* and *Baldock* [2007], that is an improvement of the breaking model proposed by *Baldock* et al. [1998], specifically referred to steep slope beaches. The dissipation rate due to the presence of vegetation is determined following *Mendez* and *Losada* [2004]:

$$D_{veg} = -\frac{1}{2\sqrt{\pi}} \rho C_{Dv} b_v N_v \left(\frac{k}{2\sigma}\right)^3 \frac{\sinh^3(k\alpha h) + 3\sinh(k\alpha h)}{3k\cosh^3(kh)} H_{rms}^3 \tag{5.2}$$

in which C_{Dv} is the bulk drag coefficient and b_v, N_v and αh are characteristics of vegetation (stem width, density and height).

The NSWEs are formulated by means of the Generalized Lagrangian Mean (GLM) approach [*Andrews* and *McIntyre*, 1978], in which continuity and momentum equations are expressed in term of the depth averaged Lagrangian velocities u_L and v_L in x and y directions. The relation with the Eulerian velocities u_E and v_E is given by:

$$u_L = u_E + u_S \text{ and } v_L = v_E + v_S \tag{5.3}$$

where u_S and v_S represent the Stokes drift in x and y directions:

$$u_S = \frac{E_w \cos\theta}{\rho h c_p} \text{ and } v_S = \frac{E_w \sin\theta}{\rho h c_p} \tag{5.4}$$

and $c_p = \sigma/k$ is the phase velocity computed by linear theory. It is important to stress that the NSWEs are forced by radiation stresses, calculated by linear wave theory [*Dean* and *Dalrymple*, 1991]. These are included as source terms in the momentum balance equation.

The effect of vegetation on the mean flow field is considered by adding a net force per unit mass F_{veg} acting on the flow [*Dalrymple* et al., 1984; *Suzuki* et al., 2011]:

$$F_{veg} = \frac{1}{2} C_{Dv} b_v N_v \frac{\alpha h}{h} |u_L| u_L \tag{5.5}$$

From now on, since a 1-D model is considered, wave energy E_w and roller energy E_r (i.e. E_w^* and E_r^* integrated over directions) will be a function of space x and time t, and only the velocity component in x direction will be considered.

5.1.2 Sediment transport and morphodynamics

Sediment transport is modelled in XBeach using a depth-averaged advection diffusion equation for each sediment class (Equation 2.9). The advective term is computed through the Eulerian velocity. Source term $E - D$ is determined by:

$$E - D = \frac{hC_{eq} - hC}{T_s} \tag{5.6}$$

where C_{eq} is the depth-averaged equilibrium sediment concentration computed through the approach proposed by *Soulsby* [1997] and T_s is an adaptation time scale based on sediment settling velocity.

Regarding bed elevation update, two versions of Exner equation are available:

$$\frac{\partial z_b}{\partial t} + \frac{f_{mor}}{(1 - n_p)} (\nabla \cdot \mathbf{q_b} - E + D) = 0 \tag{5.7a}$$

$$\frac{\partial z_b}{\partial t} + \frac{f_{mor}}{(1 - n_p)} \nabla \cdot (\mathbf{q_b} + \mathbf{q_s}) = 0 \tag{5.7b}$$

in which f_{mor} is a morphological acceleration factor [*Roelvink*, 2006] used to speed up the simulation and update the bed elevation less frequently, and $\mathbf{q_b}$ and $\mathbf{q_s}$ are respectively the bed load and suspended load transport fluxes. In this study the first version of the equation will be employed.

5.2 Modifications and implementation of additional processes in XBeach

The modifications implemented in the model are reported in Figure 5.1.

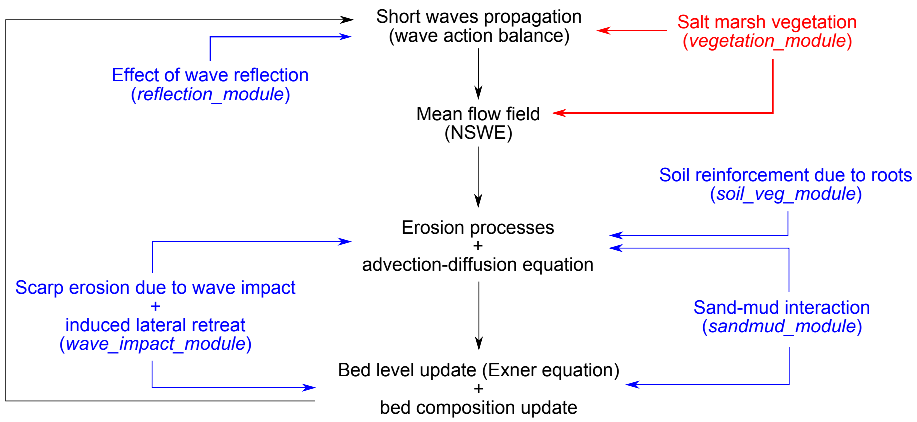

Figure 5.1: Physical processes implemented on the numerical model. Black writings represent processes already implemented in XBeach; red text identifies modified parts of the code and blue text new developed parts.

In this section, the physical processes introduced in the model are accurately described. A summary of the new and modified subroutines and modules implemented in the numerical code are reported in Appendix B. A flowchart describing the structure of the numerical code, with the implemented modifications, is outlined in Figure 5.2.

5.2.1 Implementation of sand-mud interaction

One of the purposes of this study is to introduce in the XBeach model the behaviour of cohesive sediments and their interaction with sand. To this aim, a new module (`sand_mud_module`) is developed, inspired by a simplified version of the sand-mud module already implemented in Delft3D [*Lesser* et al., 2004; *Deltares*, 2014]. The latter can describe the interaction of multiple sediment fractions, both cohesive and non-cohesive.

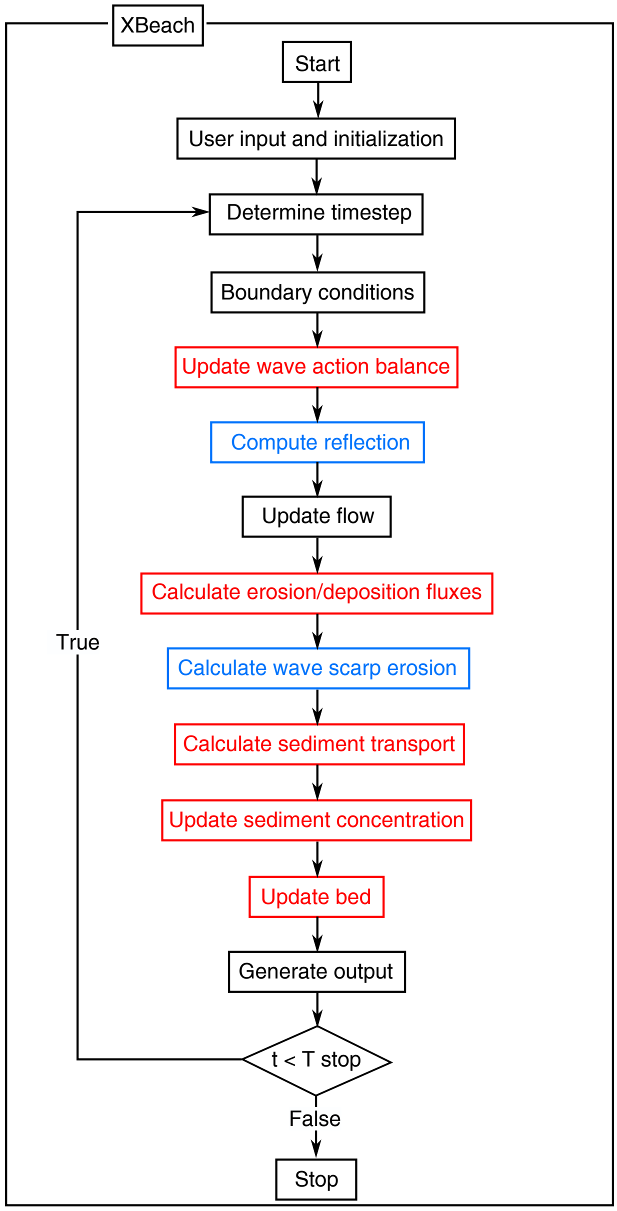

Figure 5.2: Flowchart of the main program. The principal modifications are highlighted in red and new parts in light blue.

Bed composition update for multiple sediment fractions

First, the bed update mechanism for generic multiple sediment fractions is introduced. Bed composition in XBeach is updated by means of a mixed Eulerian-Lagrangian approach [*Van Proijen*, 2012], which employs the sediment mixing layer concept [*Hirano*, 1971].

From a practical point of view, the bed is subdivided in several layers of thickness Δ_k. In each layer, sediment fractions are completely and instantaneously mixed. The thickness of the upper layer Δ_1 is kept constant during erosion and deposition processes, whereas the thickness of the underlying layer Δ_2 varies. In case Δ_2 exceeds a specific threshold (usually 1.1 times its initial thickness), it is split into two layers. In contrast, if the thickness Δ_2 becomes too small (usually less than 0.1 times the initial thickness), the layer is merged with the layer immediately below. A sketch of the process is reported in Figure 5.3.

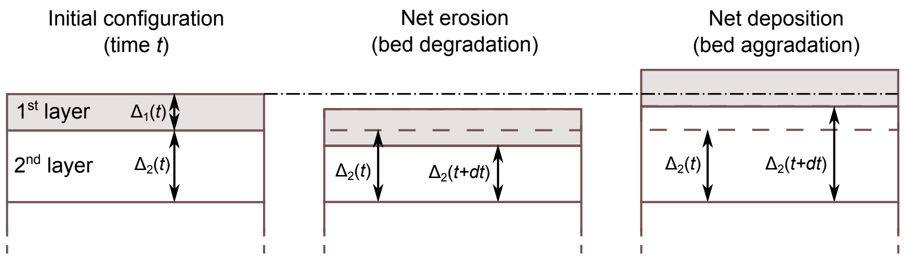

Figure 5.3: Mechanism underlying the mixing layer concept. The sketch represents the cross section of a computational cell of the spatial domain. In case of net erosion occurring during the time span dt, the upper layer (light grey) moves downward and the thickness of the second layer Δ_2 decreases. In case of net deposition occurring during the time span dt, the upper layer moves upward and the thickness of the second layer Δ_2 increases.

Formally, the thickness of a single layer is given by:

$$\Delta_k = \frac{1}{1 - n_{p,k}} \sum_{j=1}^{N_s} \frac{m_{j,k}}{\rho_{s,j}} \tag{5.8}$$

in which $n_{p,k}$ is the porosity of the k-th layer, N_s is the number of sediment classes in the bed, $m_{j,k}$ is the mass of the j-th sediment class in the k-th layer related to a specific cell area, and $\rho_{s,j}$ is the density of the j-th sediment fraction. Since in XBeach only uniform porosity and sediment density are allowed, the mass fraction per layer per class $p_{j,k}$ corresponds to the volume fraction, that is:

$$p_{j,k} = \frac{m_{j,k}}{\rho_s \Delta_k \left(1 - n_p\right)}. \tag{5.9}$$

The time evolution of the j-th mass fraction for the first and second layer is given by:

$$\frac{\partial p_{j,1}}{\partial t} = \frac{1}{\Delta_1 (1 - n_p)} \Bigg[- p_{j,f12} \sum_{i=1}^{N_s} (D_i - p_{i,1} E + q_{i,in} - q_{i,out}) + + D_j - p_{j,1} E + q_{j,in} - q_{j,out} \Bigg] \tag{5.10a}$$

$$\frac{\partial p_{j,2}}{\partial t} = \frac{1}{\Delta_2 (1 - n_p)} \Bigg[p_{j,f12} \sum_{i=1}^{N_s} (D_i - p_{i,1} E + q_{i,in} - q_{i,out}) \Bigg] \tag{5.10b}$$

where $q_{i,in} - q_{i,out}$ is the net sediment flux in vertical direction at a cell of the computational domain due to the divergence of the bed load sediment flux for the i-th class, and $p_{j,f12} = p_{j,1}$ in case of bed aggradation, whereas $p_{j,f12} = p_{j,2}$ for bed degradation.

Sand-mud mixtures

The set of subroutines developed in this study can handle at most two sediment fractions, one cohesive (mud) and one non-cohesive (sand), respectively indicated with p_m and p_s. Equations to describe the interaction are based on the studies of *Van Ledden* [2003] and *Carniello* et al. [2012] and the report "Bed module for sand-mud mixtures", by *Van Kessel* et al. [2012].

In tidal environments sand ($0.063 < d < 2$ mm), silt ($0.004 < d < 0.063$ mm) and clay ($d < 0.004$ mm) are present in variable fractions. The ratio between clay and silt is fairly constant in these environments [*Flemming*, 2000], so they can be combined in a single sediment class called mud ($d < 0.063$ mm). Since the cohesive behaviour of sediment depends on the clay content [*Raudkivi*, 1990; *Van Ledden*, 2003], it is possible to define a critical mud fraction $p_{m,cr}$ as a threshold between the cohesive and non-cohesive regime of the mixture in terms of erosion/deposition behaviour.

Following the approach proposed by *Van Ledden* [2003], if $p_m \geq p_{m,cr}$ the sediment behaves in a cohesive way and it is the mud fraction which controls the erosion rate of the mixture and bed load is assumed to be negligible. Conversely, if $p_m < p_{m,cr}$ the regime is non-cohesive, the sand fraction controls the erosion rate and bed load can be significant. In this study, very fine sediments are considered (for the sand $d_{50,s} = 0.2$ mm) and bedload is neglected in the calculations in both regimes.

Erosion rates for sand and mud read:

$$E_m = \begin{cases} p_m E_m^*, & p_m \geq p_{m,cr} \\ p_m E_s^*, & p_m < p_{m,cr} \end{cases} \tag{5.11a}$$

$$E_s = \begin{cases} (1-p_m)\, E_m^*, & p_m \geq p_{m,cr} \\ (1-p_m)\, E_s^*, & p_m < p_{m,cr}. \end{cases} \tag{5.11b}$$

where E_m^* and E_s^* are the absolute volumetric erosion rates per unit area, respectively for the cohesive and non-cohesive regime.

The absolute erosion rate in the cohesive regime is:

$$E_m^* = \frac{1}{\rho_s} M_c \left(\frac{\tau_b}{\tau_{cr,c}} - 1\right) H_f \left(\frac{\tau_b}{\tau_{cr,c}} - 1\right) \tag{5.12}$$

in which M_c is the erosion parameter in the cohesive regime, τ_b is the bottom shear stress, $\tau_{cr,c}$ is the critical shear stress in cohesive regime, and H_f is the Heaviside function. Similarly, the absolute erosion rate in the non-cohesive regime reads:

$$E_s^* = \frac{1}{\rho_s} M_{nc} T_{nc}^{\alpha_{nc}} \tag{5.13}$$

where M_{nc} is the erosion parameter for the non-cohesive regime and T_{nc} a dimensionless transport parameter [*Van Rijn*, 1993]:

$$T_{nc} = \left(\frac{\tau_b}{\tau_{cr,nc}} - 1\right) H_f \left(\frac{\tau_b}{\tau_{cr,nc}} - 1\right) \tag{5.14}$$

with $\tau_{cr,nc}$ the critical shear stress in the non-cohesive regime.

The values of the erosion parameter are calculated as follows (a more detailed explanation is given in Appendix B):

$$M_{nc} = \rho_s w_{s,s} F_s \cdot 0.015 \frac{d_{50,s}}{a_c d_*^{0.3}} \tag{5.15a}$$

$$M_c = \left(\frac{M_{nc}}{M_m}\right)^{\frac{1-p_m}{1-p_{m,cr}}} \cdot M_m \tag{5.15b}$$

in which $w_{s,s}$ is the sand settling velocity, F_s is a shape factor accounting for the sediment distribution along the water column [*Van Rijn*, 1993], a_c is the reference height from the bed for the sediment equilibrium concentration, d_* is the dimensionless grain size and M_m is the erosion parameter for pure mud, ranging from 10^{-5} to 10^{-3} kg/(m^2·s) [*Jacobs* et al., 2011; *Winterwerp* et al., 2012]. In order to avoid a discontinuous variation passing from a regime to another, the exponent α_{nc} of the dimensionless transport parameter (Equation 5.13) is set equal to 1 instead of the commonly set value 1.5. Furthermore, the proposed formulations (Equations 5.15a, b) do not directly depend on water depth h. This is done on purpose, in order to avoid sharp variations in erosion parameters, as a consequence of the high gradients in bed elevation due to the presence of the scarp.

Critical shear stresses for the two regimes are defined as [*Van Ledden*, 2003]:

$$\tau_{cr,nc} = \tau_{cr,s} \left(1 + p_m\right)^{\beta}, \qquad p_m < p_{m,cr} \tag{5.16a}$$

$$\tau_{cr,c} = \frac{\tau_{cr,s} \left(1 + p_{m,cr}\right)^{\beta} - \tau_{cr,m}}{1 - p_{m,cr}} \left(1 - p_m\right) + \tau_{cr,m}, \qquad p_m \geq p_{m,cr} \tag{5.16b}$$

where $\tau_{cr,s}$ and $\tau_{cr,m}$ are the critical shear stresses, respectively for pure sand and pure mud, and β is a parameter equal to 1.5 [*Van Ledden*, 2003].

Deposition rates for sand and mud, D_s and D_m, are calculated independently, assuming no interaction between sand and mud during settling process. This is true when the mud concentration in the water column is lower than the "gel point concentration" which is around 30-180 kg/m^3 [*Winterwerp*, 1999], corresponding to 0.01-0.07 m^3/m^3. Such concentrations are hardly reached during simulations.

Sand settling velocity $w_{s,s}$ is calculated through the formulation proposed by *Van Rijn* [1993], valid for non-cohesive sediment:

$$w_{s,s} = \begin{cases} \frac{\Delta_s g d_{50}^2}{18\nu}, & 0.063 < d_{50} \leq 0.1 \text{ mm} \\ \frac{10\nu}{d_{50}} \left[\sqrt{1 + \frac{0.01\Delta_s g d_{50}^3}{\nu^2}} - 1\right], & 0.1 < d_{50} \leq 1.0 \text{ mm} \\ 1.1\sqrt{\Delta_s g d_{50}}, & d_{50} \geq 1.0 \text{ mm}, \end{cases} \tag{5.17}$$

where $\Delta_s = \frac{\rho_s - \rho}{\rho}$ is the submerged density and ν the water kinematic viscosity. Settling velocity of mud is determined employing the formulation proposed by *Cole* and *Miles* [1983] in which $w_{s,m}$ is proportional to the mud concentration in the water column:

$$w_{s,m} = K_{w,m} C_m \tag{5.18}$$

with $K_{w,m}$ an empirical coefficient ranging from 0.001 to 0.002 and C_m the depth-averaged mud concentration.

Deposition rates are then obtained from:

$$D_s = w_{s,s} C_s \tag{5.19}$$

$$D_m = w_{s,m} C_m \left(1 - \frac{\tau_b}{\tau_{dep}}\right) H_f \left(1 - \frac{\tau_b}{\tau_{dep}}\right) \tag{5.20}$$

where τ_{dep} is the critical shear stress below which mud can deposit, determined from an experimental activity [*Krone*, 1962].

In the present formulation the effect of biological processes on erosion is not accounted for. It is initially neglected in order to maintain a simpler approach, even if it can play a role in sediment erodibility [*Le Hir* et al., 2007].

Characteristic values for the parameters introduced above are reported in Table 5.1. All the described processes are implemented in the `sand_mud_module` added to the original XBeach structure.

Determination of bed shear stress

In the original XBeach code erosion/deposition fluxes are considered through the net sediment flux from the bottom to the fluid phase, given by the difference between the depth averaged sediment concentration C and the sediment equilibrium C_{eq} concentration, multiplied by the water column h and divided by an adaptation time T_s (Equation 5.6). In this study, erosion and deposition fluxes are explicitly calculated, based on the value of the bottom shear stress τ_b. A distinction is made between bottom shear stress used in the hydrodynamic computations and the one used to determine erosion and sediment transport: the former accounts both for skin friction and form drag, whereas the latter only accounts for the skin friction.

The value of the bed stress τ_b, induced by combined waves and currents, is determined through the relation proposed by *Soulsby* [1997], in case wave and current have the same direction:

$$\tau_b = \tau_w + \tau_c \left[1 + 1.2 \left(\frac{\tau_w}{\tau_c + \tau_w} \right)^{3.2} \right]. \tag{5.21}$$

τ_w is the bed shear stress due to waves:

$$\tau_w = \frac{1}{2} \rho f_w u_{rms}^2 \tag{5.22}$$

where the friction factor f_w is given by:

$$f_w = 1.39 \left(\frac{A_{orb}}{z_0} \right)^{-0.52} \tag{5.23}$$

where $A_{orb} = u_{rms} T_p / 2\pi$ is the amplitude of the orbital excursion, u_{rms} the bottom orbital velocity, T_p the peak period and z_0 is the grain related roughness. τ_c is the bed shear stresses due to currents:

$$\tau_c = \rho C_D u_E^2 \tag{5.24}$$

with:

$$C_D = \left[\frac{\kappa}{\ln(h/z_0) - 1} \right]^2 \tag{5.25}$$

with $\kappa = 0.4$ the von Karman constant. Above formulations are implemented in the subroutine `tau_bed` contained in the module `sand_mud_module`.

Table 5.1: Values for the parameters used in the formulation for sand-mud mixtures reported in selected published studies. In the present table, $\tau_{cr,m}$ and M_m represent the critical shear stress and the erosion parameter for both pure mud and cohesive mixtures. $\tau_{cr,s}$ and M_s indicate critical shear stress and erosion parameter for both pure sand and non-cohesive mixtures.

Parameter	**Value**	**Dimension**	**Reference**
$\tau_{cr,s}$	0.5	[N/m^2]	[*Carniello* et al., 2012]
	0.4		[*Paarlberg* et al., 2005]
$\tau_{cr,m}$	0.5–3.0	[N/m^2]	[*Amos* et al., 2010]
	0.8		[*Carniello* et al., 2012]
	0.4		[*D'Alpaos* et al., 2007]
	0.7		[*Fagherazzi* et al., 2006]
	0.4–0.8		[*Marani* et al., 2010]
	0.7		[*Mariotti* and *Fagherazzi*, 2010]
	0.5		[*Van Ledden* et al., 2004]
	1.1		[*Winterwerp* et al., 2012]
M_m	$1.4{\cdot}10^{-3}$	[kg/(m^2·s)]	[*Fagherazzi* and *Furbish*, 2001]
	$4.0{\cdot}10^{-4}$–$2.0{\cdot}10^{-3}$		[*Winterwerp* and *Van Kesteren*, 2004]
	$1.0{\cdot}10^{-4}$		[*Van Ledden* et al., 2004]
	$9.5{\cdot}10^{-4}$–$6.0{\cdot}10^{-3}$	[kg/(m^2·s·Pa)]	[*Van Ledden* et al., 2004]
	$4.1{\cdot}10^{-4}$		[*Mariotti* and *Fagherazzi*, 2010]
	$2.3{\cdot}10^{-4}$	[m/s]	[*D'Alpaos* et al., 2007]
	$1.0{\cdot}10^{-8}$		[*Van Kessel* et al., 2012]
M_s	$2.0{\cdot}10^{-4}$	[kg/(m^2·s)]	[*Le Hir* et al., 2011]
	$1.0{\cdot}10^{-1}$		[*Van Ledden*, 2003]
	$1.0{\cdot}10^{-2}$		[*Waeles* et al., 2007]
	$2.3{\cdot}10^{-4}$	[m/s]	[*Van Kessel* et al., 2012]
	$1.0{\cdot}10^{-6}$		[*Van Ledden*, 2003]
τ_{dep}	1.0	[N/m^2]	[*Carniello* et al., 2012]
	0.1		[*D'Alpaos* et al., 2007]
	1.5		[*Paarlberg* et al., 2005]
	0.1–1.0		[*Van Ledden* et al., 2004]
	-		[*Winterwerp* and *Van Kesteren*, 2004]
$w_{s,m}$	$2.0{\cdot}10^{-4}$	[m/s]	[*D'Alpaos* et al., 2007]
	$5.0{\cdot}10^{-4}$		[*Van Ledden* et al., 2004]

5.2.2 Effect of wave reflection

Salt marsh boundaries are generally characterized by a steep cliff. This morphological configuration may lead to a certain degree of wave reflection, which, in turns, can induce an increase in bottom orbital velocities and a decrease of the Stokes drift and of the radiation stresses, which drive the mean flow field.

The effect of reflected waves has been widely investigated for coastal structures [*Davidson* et al., 1996; *Zanuttigh* and van der *Meer*, 2008], but it is still not included in numerical models for coastal evolution, except for *Chellew* et al. [2011], though in a schematic way.

In tidal environments, in front of a steep slope bank, reflected waves may lead to increased shear stresses at bank toe, hindering sediment deposition. The presence of currents or wave induced return flow, can result in sediment displacement from the toe of the bank. In this framework, we refer to a cross sectional domain, so that currents parallel to the marsh boundary are not considered at this stage. However, removal of sediment at the bank toe can be triggered by the return flow due to Stokes drift that is anyway present in case of partial reflection. This effect can be simulated due to the GLM approach employed in XBeach.

The role of waves in sediment removal at the bank toe is also stressed by *Schwimmer* [2001], who observed it and the lateral retreat of marsh edges maintaining their steep slope in absence of significant tidal currents, in Rehoboth Bay, Delaware (US).

Based on the flow characteristics close to the scarp of the bank and on the local morphology, the reflection coefficient K_r is determined through the following formulation [*Seelig* and *Ahrens*, 1981]:

$$K_r = \frac{a_{K_r}\zeta_0^2}{\zeta_0^2 + b_{K_r}} \tag{5.26}$$

in which ζ_0 is the surf similarity parameter $\zeta_0 = \tan\beta_0/\sqrt{(H_{rms}/L_0)}$ [*Battjes*, 1974] and a_{K_r} and b_{K_r} are empirical coefficients. The average slope of the scarp $\tan\beta_0$ is approximated by a linear regression of $z_{b,i}$ (bed elevation of i-th cell) on x_i (spatial coordinate of i-th cell), considering a set of cells which elevation is bounded above by $\eta + H_{rms}/2$, and below by $\eta - H_{rms}/2$. In case the set contains less than four cells, then the linear regression is carried out among the four cells surrounding the mean water level η.

Once K_r is known, it is possible to estimate the effect of reflected waves reducing Stokes drift u_S and radiation stress S_{xx}, and increasing root-mean-squared orbital velocity u_{rms}.

It is assumed that the effect of the reflected waves affects part of the domain up to a certain distance, in the order of $3L/2$, from the point of reflection (with L the representative wave length). This assumption is based on the results of the experimental campaign conducted by *Xie* [1981], who studied the effect of

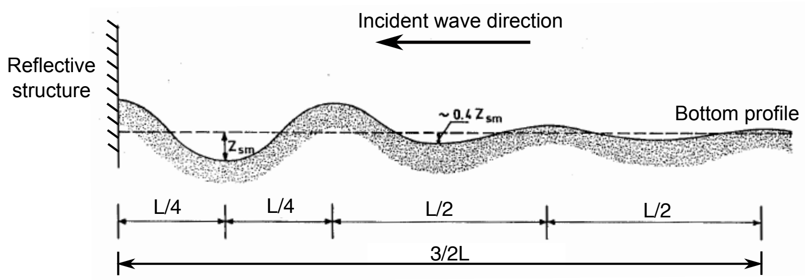

Figure 5.4: Scouring profile for erodible bottom under irregular waves. The transect represents the bottom at the toe of a vertical reflective structure identified by the vertical line [after *Xie*, 1981].

a reflective wave pattern on an erodible bottom. In Figure 5.4, the result of the experiment carried out by *Xie* [1981] with irregular waves is depicted. It is possible to notice that at a distance approximately equal to one and a half of the representative wave length, the effect of the increased scour is almost negligible. The main purpose is to convert the qualitative information given by Figure 5.4 in a mathematical formulation. Thus, the following relation is proposed to determine the reflected wave height:

$$H_r(s) = H_{rms} K_r e^{-\frac{k}{3\pi}s} \tag{5.27}$$

where s is a spatial coordinate directed offshore, with the origin at the last dry cell; H_{rms} is the root mean squared incident wave height and H_r is the associated reflected wave height. The relation provides that at a distance of $3L/2$ from the bank, the effect of H_r is reduced as compared to its value at the waterline, that is equal to $H_{rms}K_r$. Indeed, after substitution of $s = 3L/2$ into Equation 5.27, the value of the reflected wave height is $H_r = H_{rms}K_r/e$. It is important to underline that Equation 5.27 is formulated based on a qualitative interpretation of the experimental results reported in Figure 5.4, and it need to be quantitatively verified in future studies.

The effect of the reflected waves on Stokes drift and radiation stress in x direction is given by:

$$\hat{u}_S = u_S \left(1 - \frac{H_r^2}{H_{rms}^2}\right) \tag{5.28}$$

$$\hat{S}_{xx} = S_{xx} \left(1 - \frac{H_r^2}{H_{rms}^2}\right) \tag{5.29}$$

where $\hat{u}_S$ and $\hat{S}_{xx}$ are the modified values of the Stokes drift and the radiation stress.

The increase of u_{rms} requires more attention. The principal aim is to obtain a higher bed shear stress which might produce the seabed pattern observed in Figure 5.4. In case of complete reflection ($K_r = 1$), the bottom orbital velocity

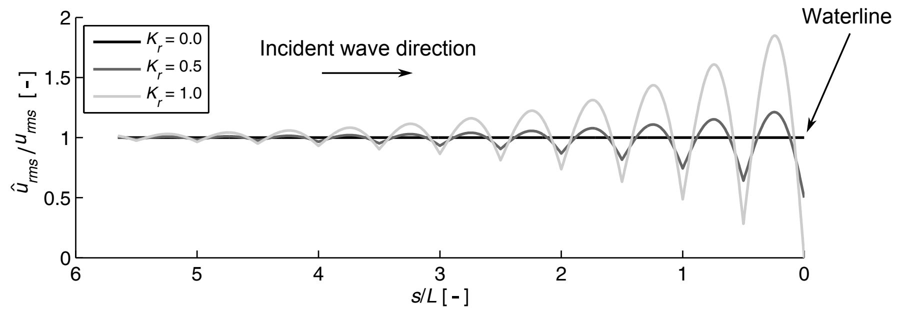

Figure 5.5: Spatial evolution of the root-mean-squared velocity $\hat{u}_{rms}$ determined from Equation 5.30, for different values of K_r. On the x-axis, the value of the distance from the shoreline is reported.

at the shoreline must be zero, and moving offshore from the shoreline, u_{rms} should be modulated by a periodical function. Above characteristics should reduce and vanish for $K_r = 0$. The following formula is thus proposed to describe the effect of reflection on u_{rms}

$$\hat{u}_{rms} = u_{rms} (1 + K_r) f_p(s) f_r(s) + u_{rms} [1 - f_r(s)] \tag{5.30}$$

where $f_p(s) = |\sin(ks)|$ accounts for the modulation of the signal and $f_r(s) = K_r \cdot \exp(-\frac{k}{3\pi} s)$ accounts for the damping of the reflected wave signal. For $K_r = 0$, $\hat{u}_{rms} = u_{rms}$, whereas for $K_r = 1$, $0 < \hat{u}_{rms} < 2u_{rms}$. In Figure 5.5 the value of $\hat{u}_{rms}$ is reported for different values of K_r. The modelling of the reflection process is introduced in the `reflection_module`.

5.2.3 Effect of vegetation

Effect on the flow field

In XBeach, the effect of vegetation in dissipating wave energy is accounted for in the wave action balance (Equations 2.3 and 5.2). Such an approach implicitly assumes that plant induced reflection is negligible and the movement of plants is not modelled. These effects are embedded in the bulk drag coefficient C_{Dv}. Apart from the specific characteristics of the plants (stem width b_v, density N_v and plant height αh), the bulk drag coefficient C_{Dv} is crucial in the determination of the wave energy dissipation rate due to vegetation D_{veg}.

Available laboratory experiments and field measurements lead to very different values of the bulk drag coefficient C_{Dv}, since it strongly depends on vegetation typology [*Mol*, 2003; *Bouma* et al., 2005; *Augustin* et al., 2009; *Jadhav* et al., 2013; *Ozeren* et al., 2013].

Mendez and *Losada* [2004] found a relation between C_{Dv} and the Keulegan-Carpenter number $KC = \frac{u_c \cdot T_{rep}}{b_v}$ (actually a slightly modified version of it), accounting also for the relative height of the plants $\alpha_v = \frac{\alpha h}{h}$, with u_c equal to:

$$u_c = \frac{H_{rms}\sigma \cosh(k\alpha h)}{2\sinh(kh)} \tag{5.31}$$

Nonetheless, their relation refers to artificial kelp models of *Laminaria Hyperborea* that are really flexible seaweeds which hydrodynamic behaviour is different from a more stiff salt marsh plant.

Ozeren et al. [2013] found several relations for the bulk drag coefficient from experiments based on different vegetation typology, among which *Spartina Alterniflora* plant. *Jadhav* et al. [2013] also obtained C_{Dv} from field data on a marsh covered by *S. Alterniflora*. They respectively proposed the following relations:

$$C_{Dv} = 0.036 + \frac{50}{KC^{0.93}}, \qquad \text{for } \textit{Ozeren} \text{ et al. [2013]} \tag{5.32a}$$

$$C_{Dv} = \frac{70}{KC^{0.86}}, \qquad \text{for } \textit{Jadhav} \text{ et al. [2013].} \tag{5.32b}$$

However, it is important to stress that *Jadhav* et al. [2013] based their regression analysis on a slightly different formulation with respect to Equation 5.2.

In this study, the characteristics of vegetation will be taken from Table 5.2, whereas C_{Dv} will be determined from Equation 5.32a (with a threshold for the obtained value at really low KC).

This part is implemented in the subroutine `bulkdragcoeff` added to the `vegetation_module`.

Effect on strengthening the soil

The effect of vegetation in enhancing soil strength, thus reducing erosion, is a widely accepted concept, specifically for salt marsh banks [*Van Eerdt*, 1985b; *King* and *Lester*, 1995; *Chen* et al., 2012], even if a debate remains among researchers [*Feagin* et al., 2009]. Indeed, *Feagin* et al. [2009] argued that salt marsh plants do not mitigate the total amount of erosion along the wetland edge and that the soil type is the primary variable that influences the lateral erosion rate. Plants may only indirectly influence erosion rate via modification of the soil parameters. Nevertheless, they refer specifically to the process of detachment of particles from a volume of soil where roots are present and not to the role of vegetation in enhancing the overall bank stability. Recently, *Francalanci* et al. [2013] showed through laboratory experiments that the presence of vegetation can induce a delay in mass failure, even if its effect in decreasing total eroded amount of material was not really high.

Field observations of marsh edges usually show the presence of cantilever profiles with a vegetated upper part and scour at bank toe. This may suggest a positive role played by vegetation in strengthening the soil against erosion as shown in Chapter 4 above.

Table 5.2: Plant characteristics from several authors to be used in Equation 5.2. Only vegetation present on salt marshes is reported.

Parameter	Value	Dimension	Plant typology	Reference
b_v	8.0	[mm]	*S. Alterniflora*	[*Jadhav* et al., 2013]
	2.3–3.9		*Z. Noltii*	[*Mol*, 2003]
	3.0–5.0		*S. Anglica*	[*Bouma* et al., 2005]
	2.4–6.5		*S. Alterniflora*	[*Ozeren* et al., 2013]
N_v	422	[units/m^2]	*S. Alterniflora*	[*Jadhav* et al., 2013]
	1550		*S. Anglica*	[*Suzuki*, 2011]
	620–1700		*Z. Noltii*	[*Mol*, 2003]
	395–13400		*S. Anglica*	[*Bouma* et al., 2005]
	540–2860		*S. Alterniflora*	[*Ozeren* et al., 2013]
αh	0.4	[m]	*S. Alterniflora*	[*Jadhav* et al., 2013]
	0.3–0.5		*S. Anglica*	[*Suzuki*, 2011]
	0.3–0.4		*Z. Noltii*	[*Mol*, 2003]
	0.1		*S. Anglica*	[*Bouma* et al., 2005]
	0.6–1.0		*S. Alterniflora*	[*Ozeren* et al., 2013]

It is important to stress that salt marshes are subjected to both shear stress erosion and wave impact erosion. In both cases vegetation can play a role in modifying the erosion rates. In this study the effect of vegetation is assumed to increase only the soil critical shear stress. Therefore, bank erodibility due to wave impact is initially assumed not to be influenced by vegetation (see next section).

To model the effect of vegetation on soil erodibility, the approach proposed by *Van der Meer* et al. [2007] and *Tuan* and *Oumeraci* [2012], who obtained their results with reference to sea dikes, is followed.

The formulation for the critical velocity for the erosion of the grass-permeated soils $u_{cr,v}$ reads:

$$u_{cr,v} = 0.64 \log\left(\frac{8.8h}{d_a}\right)\sqrt{\Delta_s g d_a + \frac{1}{\rho}\left(0.6C_{cu} + C_r\right)} \tag{5.33}$$

where d_a is the size of the clay detaching aggregates (order of 0.003–0.005m), $C_{cu} = 0.035c_u$ is the fatigue rupture strength of the clay (c_u is the undrained shear strength), and $C_r = 1.2 \cdot RAR \cdot t_r$ [*Wu* et al., 1979] accounts for the effect of roots, called "root cohesion". RAR is the root area ratio, defined as the root area per unit area, and t_r is the root tensile strength [*Wu* et al., 1979]. *Tuan* and *Oumeraci* [2012] proposed a refinement of the above relation to account for the partial strength mobilization of grass roots and its variation with depth. We initially neglect this aspect to maintain a simpler approach.

This assumption allows to calculate the value of RAR from literature data as reported in Appendix B.

Looking at Equation 5.33 three terms are identifiable under the square root, corresponding to different resistance effects. The first term accounts for the submerged weight of the removed aggregates, whereas the terms related to C_{cu} and C_r respectively account for the resistance due to the cohesion of the material and the reinforcement due to the presence of roots.

Equation 5.33 specifically refers to cohesive soils. However, it will be employed also for mixtures of mud and sand. To consider this aspect, the term accounting for the cohesion of the material (C_{cu}) is multiplied by the initial mud fraction in the bed.

Critical shear velocity $u_{cr,v}$ can be related to the critical shear stress for erosion of root-permeated soils $\tau_{cr,v}$ via [*Tuan* and *Oumeraci*, 2012]:

$$\tau_{cr,v} = \frac{1}{2}\rho g \left(\frac{u_{cr,v}}{C_{cz,v}}\right)^2 \tag{5.34}$$

where $C_{cz,v}$ is the Chezy coefficient in presence of vegetation.

To adapt the present formulation to Equations 5.16a and b, the following formula is proposed:

$$\tau_{cr,v} = \tau_{cr} C_{sv}^2 \left(1 + \frac{C_r}{\rho \Delta_s g d_a + p_m 0.6 C_{cu}}\right) \tag{5.35}$$

where $C_{sv} = C_{cz}/C_{cz,v}$, C_{cz} is the Chezy coefficient for the bare soil and τ_{cr} can be indifferently be equal to $\tau_{cr,c}$ or $\tau_{cr,nc}$. Passages to get Equation 5.35 are reported in Appendix B.

To employ Equation 5.35, root area ratio (RAR) data are necessary, as well as t_r, and c_u. The latter is obtained from literature [*Winterwerp* et al., 2012]. Information about the root area ratio can be achieved by the analysis of literature data on belowground biomass production. In Table 5.3 values of RAR from different authors for salt marsh plants are reported, and in Appendix B the procedure to obtain RAR from literature data is described.

Table 5.3: Values of root area ratio (RAR) obtained from available studies.

RAR [%]	Plant typology	Reference
0.66–2.21	*S. Alterniflora*	[*Blum*, 1993]
0.83–15.00	*S. Alterniflora, S. Patens*	[*Connor* and *Chmura*, 2000]
0.03–5.00	*S. Alterniflora*	[*Turner* et al., 2004]
0.25–0.83	*S. Americus, S. Alterniflora*	[*Kirwan* and *Guntenspergen*, 2012]
9.00–31.5	*A. Portulacoides, J. Maritimus*	[*Chen* et al., 2012]

Root tensile strength of marsh vegetation can be obtained from *Van Eerdt* [1985b], it results around 1966 kN/m^2. Such a value has to be carefully handled because, at the knowledge of the author, similar values for salt marsh vegetation are not available in literature.

From a computational point of view, the presence of vegetation in a cell of the spatial domain is specified by assigning a flag to it. In case the cell is eroded more than a certain threshold r_d (root depth), then the flag is "switched off" and the vegetation is considered to be removed, even if the cell is subsequently subject to deposition. Such a threshold is chosen based on a representative length of the root mat [*Blum*, 1993].

The effect of vegetation in increasing critical shear stress is implemented in the `soil_vegetation_module`.

5.2.4 Erosion due to wave impact and bed update

The impact of waves on the surface of the marsh scarp can induce the detachment of aggregates of particles of different sizes.

In the present work, the same framework proposed by *Mariotti* and *Fagherazzi* [2010] and *Marani* et al. [2011] is employed. The volumetric erosion rate per unit width R_{sc}, is linearly related to the wave energy flux W, averaged over a wave length (shoreward from the waterline), through an erodibility parameter M_{sc}.

Wave power is calculated by:

$$W = E_w \cdot c_g + E_r \cdot c_p \tag{5.36}$$

where E_w and E_r are the wave and roller energy, and c_g and c_p are the group and phase velocity. The volumetric erosion rate due to wave impact is then [*Mariotti* and *Fagherazzi*, 2010]:

$$R_{sc} = \begin{cases} 0, & W < W_{cr} \\ M_{sc}\left(W - W_{cr}\right), & W \geq W_{cr} \end{cases} \tag{5.37}$$

In order to update bed elevation z_b, the volumetric erosion rate R_{sc} has to be transformed into a vertical erosion rate E_{sc}, and split among the cells being part of the scarp. These are identified among those having a slope higher than a specific threshold s_{sc}, calculated in an upwind manner. Lower and upper cells are indicated respectively as $z_{b,toe}$ and $z_{b,top}$, and $b_h = z_{b,top} - z_{b,toe}$ is the local bank height.

At the same time, the erosion due to wave impact is better represented by an erosion rate in horizontal direction E^*_{sc}, which can be seen as a sort of celerity at which the scarp migrates onshore (Figure 5.6a).

To resemble the lateral retreat, first it is assumed the following equality (Figure 5.6a):

$$E^*_{sc} dz_b = E_{sc} dx = dR_{sc}, \tag{5.38}$$

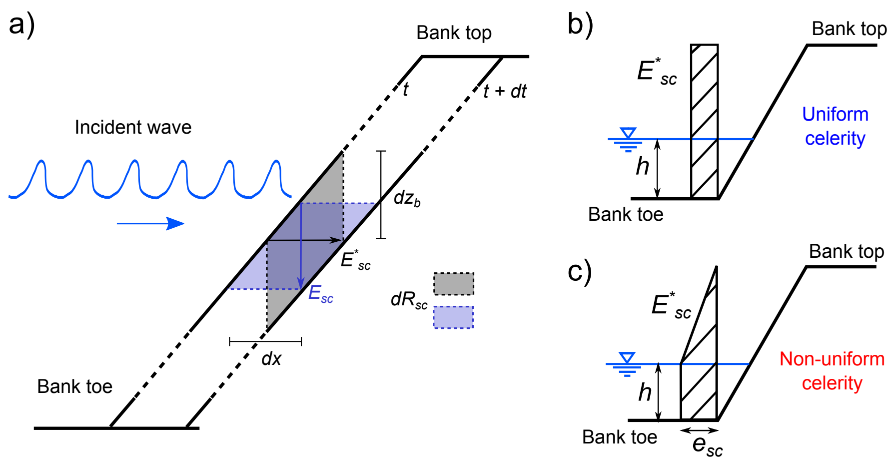

Figure 5.6: Sketch of the framework employed to describe the horizontal retreat of the bank due to wave impact. a) Relation between E_{sc}, E^*_{sc} and dR_{sc}. b) Retreat mechanism with uniform scarp celerity E^*_{sc} along vertical direction. c) Retreat mechanism with non uniform scarp celerity E^*_{sc} along vertical direction.

then, the value of E_{sc} computed by Equation 5.38 is substituted into the Exner equation by assuming that deposition rate and bedload are neglected (no deposition occurs on the scarp), and the following relation is obtained:

$$\frac{\partial z_b}{\partial t} + \frac{f_{mor}}{1-n_p} E^*_{sc} \frac{\partial z_b}{\partial x} = 0, \;\; z_{b,toe} \leq z_b \leq z_{b,top}. \tag{5.39}$$

Equation 5.39 is a first order linear hyperbolic equation [*Toro*, 2009], describing the "transport" of the bed elevation profile z_b, and E^*_{sc} is the celerity at which the scarp migrates. Moreover, it is possible to consider a non-uniform celerity (Figure 5.6c) to simulate the localized effect of wave impact. If waves hit the lower part of the bank, the upper part will be less damaged. In such a case Equation 5.39 is a non-linear hyperbolic equation which can lead to the formation of steep profiles, representing the steepening of the bank in case waves tend to erode the lower part of the salt marsh profile.

It is proposed to define E^*_{sc} as (Figure 5.6c):

$$E^*_{sc} = \begin{cases} e_{sc}, & z_{b,toe} \leq z_b < z_{b,toe} + h \\ \frac{e_{sc}}{z_{b,top} - z_{b,toe} + h} \left(z_{b,top} - z_b \right), & z_{b,toe} + h \leq z_b \leq z_{b,top} \end{cases} \tag{5.40}$$

with $e_{sc} = 2R_{sc}/(z_{b,top} - z_{b,toe} + h)$, and:

$$R_{sc} = \int_{z_{b,toe}}^{z_{b,top}} E^*_{sc} \, dz \tag{5.41}$$

The discretization of Equation 5.39 is carried out using a Godunov's scheme [*LeVeque*, 2002; *Toro*, 2009] (see Appendix B).

In Figure 5.7 the solution of Equation 5.39 at different time steps, in case E^*_{sc} is uniform (blue line) or non-uniform (red line), is reported (see also Figures 5.6b and c). It represents a schematic case in which horizontal and vertical coordinates are made dimensionless. It is possible to observe that in case the celerity is kept constant along the vertical dimension of the cliff, the temporal evolution of the profile (blue line in Figure 5.7a and b) is not affected by the water level at which waves strike the bank. On the contrary, in case E^*_{sc} depends on the water level at which waves impact on the cliff, the profile evolves differently (red line in Figure 5.7a and b) and a steeper slope develops.

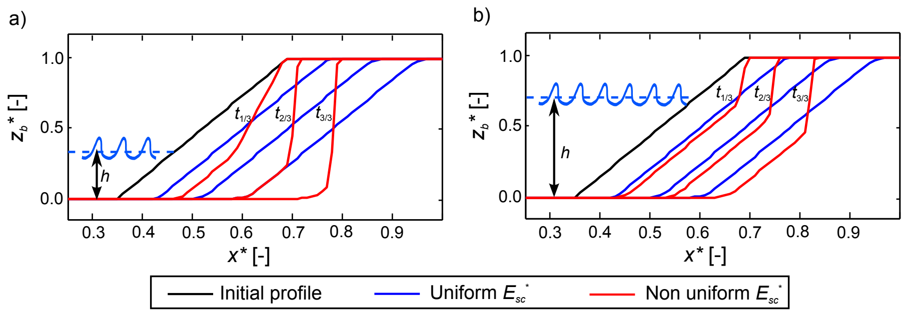

Figure 5.7: Qualitative comparison of the evolution of a bank scarp for two water levels applying Equation 5.39 with a constant value for E^*_{sc} (blue line) variable E^*_{sc}-value (red line). The evolution is compared at three different time steps, corresponding to one third, two thirds and the total duration of the simulation. For all the simulations the same value of wave forcing and erosion parameter have been used.

In the model, the eroded material from the dry part of the bank is distributed as an input sediment flux among the cells included within a wavelength from the waterline.

5.3 Model results and discussion

In this section, the results from the numerical experiments are shown and a critical analysis on the main outcomes is reported.

5.3.1 Results of the numerical experiments

Simulations are run in order to investigate the effect of soil composition and the presence of vegetation, starting from the initial configuration reported in Figure 5.8. All simulations lasted a time interval T_{run}, set equal to 6 days.

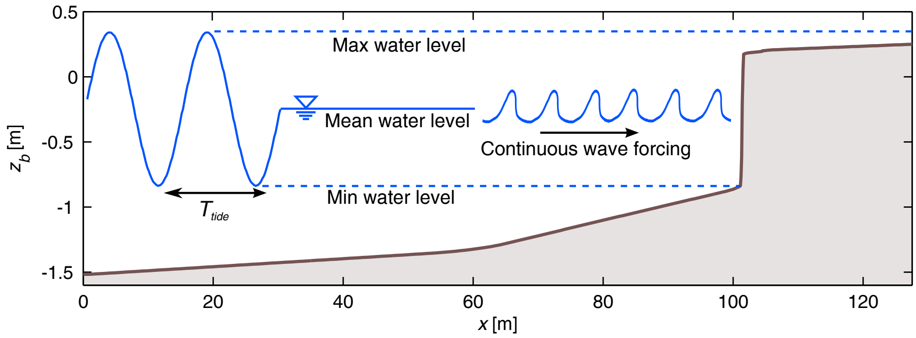

Figure 5.8: Initial bed level $z_{b,0}$ for the domain employed in the numerical experiments. Simulations are run with continuous wave forcing superimposed to a semidiurnal tide with period T_{tide} approximated to 12 hours.

Effect of soil composition on bank profile (without vegetation)

The first set of simulations is aimed at the investigation of the effect of soil composition on the evolution of the system. Four different numerical experiments are run by varying the sand (p_s) and mud (p_m) fractions composing the soil, in absence of vegetation. Following combinations are considered: $p_m = 0.8$ and $p_s = 0.2$; $p_m = 0.6$ and $p_s = 0.4$; $p_m = 0.4$ and $p_s = 0.6$ and $p_m = 0.2$ and $p_s = 0.8$. Critical mud fraction $p_{m,cr}$ is set equal to 0.3 [*Van Ledden*, 2003; *Van Ledden* et al., 2004; *Le Hir* et al., 2011].

It is important to stress that the avalanching process implemented in XBeach is usually deactivated during the simulations. If the initial mud fraction for the overall system is lower than $p_{m,cr}$, then the avalanching process of XBeach is activated.

At this stage, the value of the scarp erosion parameter M_{sc} and of the critical wave power for the onset of erosion W_{cr}, are affected neither by soil composition, nor by the presence of vegetation. Soil composition influences both the critical shear stress $\tau_{cr,c/nc}$ and the erosion parameter $M_{c/nc}$. Vegetation affects only the soil critical shear stress $\tau_{cr,c/nc}$, both in cohesive and non cohesive regime. Furthermore, the value of M_{sc} employed in the simulations is set to 2.5 times the value of the slope of the regression line of sector 4, if mass failures are present, that is roughly equal to $2.6 \cdot 10^{-8}$ m^3/J (Figure 4.11; based on the physical dimensions of the axis of the figure, the slope of the regression line is expressed in m^3/(yr·W), dividing it by the number of seconds in one year, it is possible to obtain m^3/J). Based on the results presented in Chapter 4, it is possible to expect an increase in M_{sc}, thus reducing the reference temporal scale. Indeed, it is important to note that the value of M_{sc} obtained by *Marani* et al. [2011], using data averaged over decades and several km, is of the order of $1.2 \cdot 10^{-9}$ m^3/J, roughly twenty times lower than the value obtained through the present field measurement in this study (discussion is given in Chapter 4). The value of

M_{sc} is indeed increased in order to emphasize the effect of wave impact erosion.

In Table 5.4 the applied parameters which remained unchanged for all the simulations are listed.

The final profiles for different soil compositions after 6 days of continuous wave forcing are plotted in Figure 5.9. Decreasing the mud fraction, the final bed configuration tends to flatten and the scarp is substituted by a gentler profile. This behaviour is clearly observable for the combination with $p_m = 0.2$ and $p_s = 0.8$, also because the avalanching process is activated. However, even for the combination $p_m = 0.4$ and $p_s = 0.6$, the bed elevation at the end of the numerical experiment tends towards a dissipative profile. On the other hand, the muddy bank tends to migrate landward maintaining its shape. Such a different behaviour can be explained by the fact that for a muddy bank the effect of bed shear stress is not strong enough to smooth the profile, whereas hydrodynamic forcing can easily wash away sediment for the case of sand being the predominant fraction.

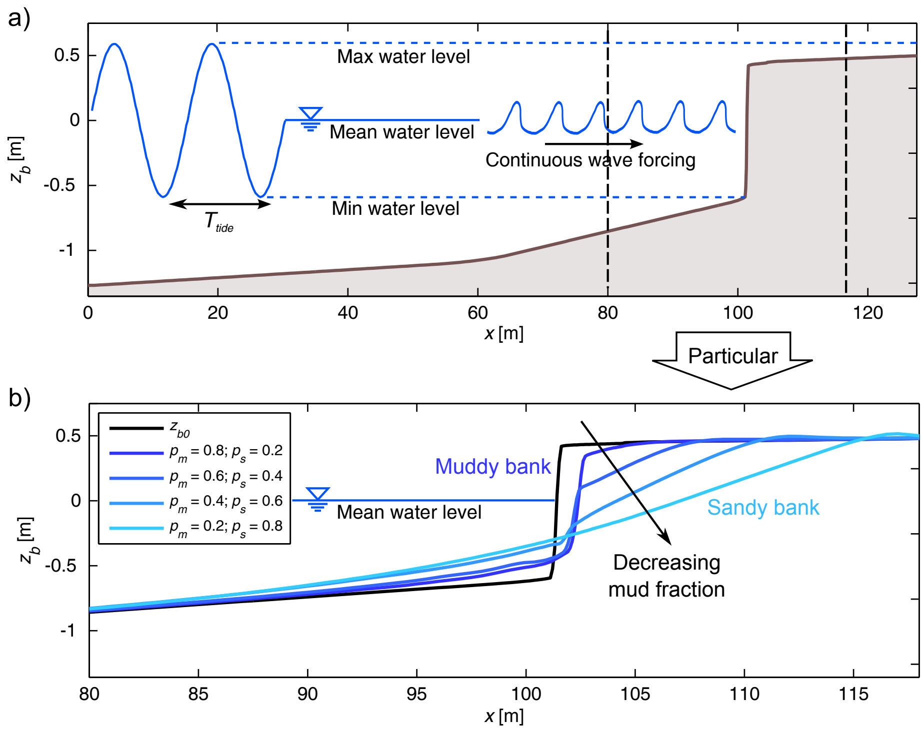

Figure 5.9: Comparison of salt marsh profiles after T_{run} = 6 days of continuous wave forcing for different soil compositions: $p_m = 0.8$ and $p_s = 0.2$ (darkest blue line); $p_m = 0.6$ and $p_s = 0.4$ (dark blue line); $p_m = 0.4$ and $p_s = 0.6$ (light blue line); $p_m = 0.2$ and $p_s = 0.8$ (lightest blue line). a) Global view of the final profiles. b) Zoomed view of the final profiles.

Table 5.4: Parameters of XBeach employed in the simulations.

Parameter	**Description and reference**	**Value**	**Dimension**
H_{rms}	Root-mean-squared wave height	0.28	[m]
h	Mean water depth in front of the bank	0.75	[m]
T_{rep}	Representative wave period	2.5	[s]
A_{tide}	Tidal amplitude	1.1	[m]
T_{tide}	Tidal period	12.0	[hours]
T_{run}	Duration of the simulation	6.0	[days]
$d_{50,s}$	Grain diameter sand	0.2	[mm]
$d_{50,m}$	Grain diameter mud	0.06	[mm]
ρ_s	Sediment density	2650	[kg/m^3]
n_p	Sediment porosity	0.4	[-]
z_0	Bed roughness [*Soulsby*, 1997]	0.2	[mm]
C_{cz}	Chezy coefficient [*Van Rijn*, 1993]	75	[m$^{1/2}$/s]
$C_{cz,v}$	Chezy coefficient for vegetation [*Rinaldo* et al., 1999]	20	[m$^{1/2}$/s]
M_m	Mud erosion parameter	$4.0 \cdot 10^{-4}$	[kg/m^3·s]
τ_m	Critical shear stress for pure mud	1.0	[N/m^2]
τ_s	Critical shear stress for pure sand	0.4	[N/m^2]
τ_m	Critical shear stress for deposition	-	[N/m^2]
M_{sc}	Erosion parameter due to wave impact	$6.5 \cdot 10^{-8}$	[m^3/J]
W_{cr}	Critical wave power for scarp erosion	0.0	[W/m]
$p_{m,cr}$	Critical mud fraction [*Van Ledden* et al., 2004; *Le Hir* et al., 2011]	0.3	[-]
a_{K_r}	Empirical parameter in equation 5.26	0.45	[-]
b_{K_r}	Empirical parameter in equation 5.26	10.0	[-]
CFL	Courant-Friedrichs-Lewy number	0.9	[-]
Δ_1	Thickness of the top sediment layer	0.05	[m]
Δ_n	Thickness of the underlying layers	0.1	[m]
f_{mor}	Morphological acceleration factor [*Roelvink*, 2006]	10	[-]
s_{sc}	Slope threshold over which a cell is subject to wave impact erosion	0.2	[-]
$sc_{sl,d}$	Slope threshold for avalanching for dry slope (XBeach default value)	1.0	[-]
$sc_{sl,w}$	Slope threshold for avalanching for wet slope (XBeach default value)	0.3	[-]

Effect of vegetation on bank erosion profile for different soil compositions

To test the effect of vegetation on the morphodynamic behaviour of the system, simulations are run for three different cases: no vegetation is present, vegetation affects only hydrodynamics and vegetation affects both hydrodynamic and soil resistance. In Table 5.5 the parameters related to the simulations in presence of vegetation are summarized. These characteristics of marsh plants are chosen on the basis of available literature studies [*Van Eerdt*, 1985b; *Blum*, 1993; *Jadhav* et al., 2013; *Ozeren* et al., 2013].

Figure 5.10 illustrates the differences among the final profiles for different soil compositions with and without vegetation on the top of the salt marsh. It is seen that the effect of vegetation in reducing the morphological variation of the system is more pronounced for a sandy bank than for a muddy bank.

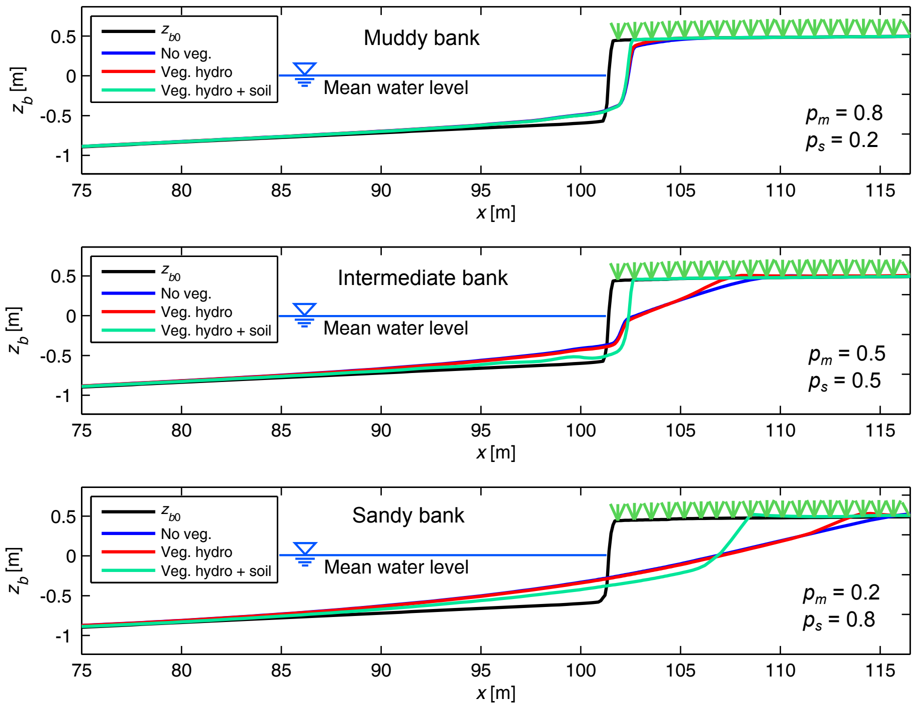

Figure 5.10: Comparison of salt marsh profiles after T_{run} = 6 days of continuous wave forcing for different soil compositions in presence of vegetation. Black line is the initial bed profile, blue line is the final profile in absence of vegetation, red line is the final profile in case vegetation affects only hydrodynamics and green line is the final profile in case vegetation affects both hydrodynamics and soil resistance. a) Muddy bank ($p_m = 0.8$ and $p_s = 0.2$). b) Intermediate bank ($p_m = 0.5$ and $p_s = 0.5$). c) Sandy bank ($p_m = 0.2$ and $p_s = 0.8$).

This behaviour can be ascribed to the fact that for a bank, mostly com-

Table 5.5: Parameters related to vegetation.

Parameter	Description and reference	Value	Dimension
αh	Vegetation height	0.35	[m]
b_v	Stem width	8.0	[mm]
N_v	Vegetation density	600	[units/m^2]
RAR	Root area ratio	1.0	[%]
t_r	Root tensile strength	1500	[kN/m^2]
r_l	Root depth	0.20	[m]

posed of mud, the critical shear stress for erosion is hardly exceeded by the bed shear stress, and the vegetation tends to increase an already high value of τ_{cr}. Conversely, for an intermediate or a sandy bank, the presence of vegetation lead to a sharp increase of the critical bed shear stress and the difference in the shape of the final profile, between the cases with and without vegetation, is more pronounced. This effect can be observed even in case mud fraction is really low (Figure 5.10c) and the system is assumed to globally behaves non-cohesively. A small cliff appears in the vegetated final profile (light green line), whereas the non-vegetated profile (blue line) and the one associated to the case when vegetation affects only hydrodynamics (red line), resulted in a dissipative gentle slope.

Effect of soil composition and vegetation on the eroded volume

In order to estimate the extent of the morphological variation occurred during each numerical experiment, the total eroded volume EV has been determined through the following relation:

$$EV = \int_{x_i}^{x_f} f\left[z_b(x, T_{run})\right]\, dx \tag{5.42}$$

where x_i and x_f are respectively the shoreward and landward boundaries of the spatial domain, and:

$$f(z_b) = \begin{cases} z_{b0} - z_b(x, T_{run}), & \text{if } z_{b0} - z_b(x, T_{run}) > 0 \\ 0, & \text{if } z_{b0} - z_b(x, T_{run}) \leq 0. \end{cases} \tag{5.43}$$

In Figure 5.11a the eroded volume computed through Equation 5.42a is described as a function of the mud fraction p_m, whereas in Figure 5.11b, the eroded volume is plotted against the RAR for two different soil compositions.

From Figure 5.11a, it is clear that the presence of vegetation tends to be less important for salt marsh banks characterized by a high mud fraction.

Figure 5.11b shows that beyond a certain RAR value (about 0.2 %), the behaviour of the system tends to remain unchanged. Once such a value decreases below a certain threshold, a sharp variation in system behaviour can be expected, at least for the sandy bank. For a sake of simplicity, only the RAR has been varied, instead of the tensile strength t_r, since $C_r = 1.2 \cdot RAR \cdot t_r$ depends linearly from both quantities considered individually.

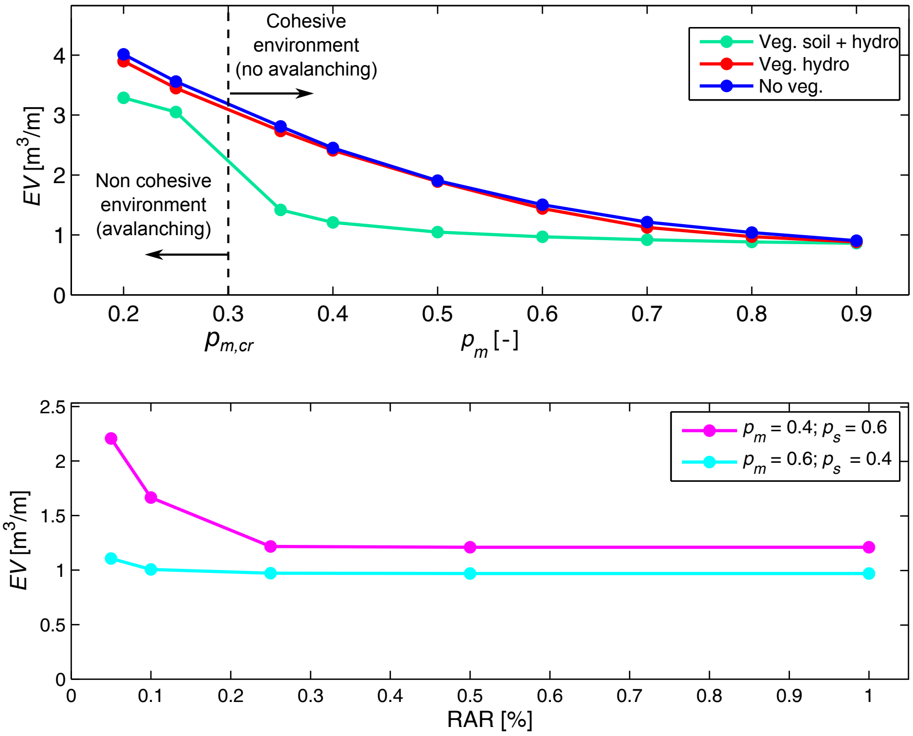

Figure 5.11: a) Eroded volume at the end of the numerical experiment as a function of the initial mud fraction of the system for three different scenarios: absence of vegetation (blue line); vegetation affects only hydrodynamics (red line); vegetation affects both hydrodynamics and soil resistance (green line). b) Eroded volume at the end of the numerical experiment ($T_{run} = 6$ days) as a function of the RAR for two different soil compositions: $p_m = 0.6$ and $p_s = 0.4$ (light blue line); $p_m = 0.4$ and $p_s = 0.6$ (magenta line).

5.3.2 Critical discussion

The numerical model developed in this chapter has been employed to investigate the effect of the characteristic parameters of a salt marsh bank on the bank profile evolution under wave forcing. Despite the simplifications introduced, the results provide an improved understanding of the differences among the profiles characterizing the salt marsh edges in several parts of the world (Figure 2.2).

The first set of numerical experiments is focused on the effect of soil composition on salt marsh bank profiles. Two main erosive processes can be identified, which act differently on shaping the scarp of the bank: wave impact erosion and shear stress erosion.

Wave impact erosion is mainly related to the wave-induced pressure on the bank scarp and promotes a horizontal erosion rate, leading to a landward migration of the bank profile. In this case, the eroded material is partially deposited at the bank toe and partially removed by the effect of waves. The amount of sediment removal from the bank toe increases, increasing finer fraction (p_m), because fine sediment, once eroded, are more easily washed away as soon as they are in suspension. Regarding the latter process, the effect of the waves consists in both sediment stirring due to partial reflection and return current due to the Stokes drift. Partial wave reflection is indeed due to the irregularity and the roughness of the vertical profile of the cliff. For the simulations, a value of $a_{K_r} = 0.45$ has been employed in Equation 5.26, leading to a maximum reflected wave height H_r almost half the incident wave height H_{rms}. The choice of $a_{K_r} = 0.45$ (that is the asymptotic value that K_r may reach, see Equation 5.26) is due to two different reasons. On the one hand, the surface of the marsh scarp is usually quite irregular, reducing the reflection process. On the other hand, results of simulations with higher values of a_{K_r} (around 0.75), led to an excessive scour at the bank toe, that is not observed in the field. The validity of this choice needs to be investigated and tested in future studies.

Shear stress erosion, is related to the effect of bed shear stress and tends to flatten the bed profile; it is more pronounced when the bank is characterized by a higher sand fraction. In Figure 5.12 the temporal evolution of the salt marsh bank profile is reported at different time steps with respect to the total simulation time T_{run} (6 days), in case $p_m = 0.4$ and $p_s = 0.6$ (avalanching process is not activated). It is possible to observe that in such a case, the effect of wave impact erosion is overcome by that of the shear erosion, which tends to smooth the shape of the scarp, promoting the formation of a gentle profile.

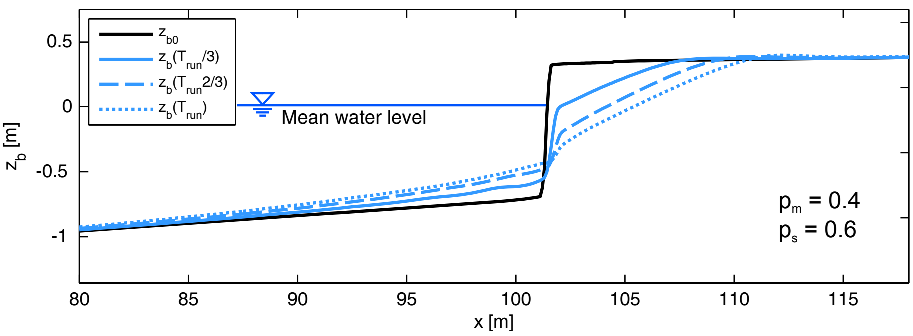

Figure 5.12: Temporal evolution of the salt marsh bank profile subject to continuous wave forcing superimposed to tide for $p_m = 0.4$ and $p_s = 0.6$. Black line: initial profile; light blue line: bank profile after one third of the simulation; dashed light blue line: bank profile after two third of the simulation; dash-dotted light blue line: bank profile at the end of the simulation.

Actually, the reduced significance of wave impact erosion as compared to that of shear erosion, might partially depend on the fact that scarp erosion parameter due to wave impact M_{sc} is tentatively assumed to be independent of the soil composition. In fact, it seems reasonable to expect that M_{sc} is higher for a sandy bank than for a muddy bank, but no information can be found in the literature on the dependency of M_{sc} from the soil composition. However, the principal aspect to be underlined is that the rate at which the bank is smoothed, is higher than the rate at which it tends to migrate landward, especially during the first time interval $t = T_{run}/3$ of the total simulation time T_{run} (Figure 5.12).

From the analysis of the numerical results, the stabilizing effect of vegetation might be crucial for the bank morphology, depending on the soil composition. Figure 5.10a shows that salt marshes characterized by a high mud fraction are not strongly affected by the presence of the root mat of vegetation.

A similar conclusion can be reached based on the field observations made by *Allen* [1989] on the salt marshes located in the Severn Estuary (UK). It was found that cohesive muddy sediments yield tall cliffs with a steep scarp, and the roots of the vegetation present on them form a thin layer, slightly contributing to a reduction of the erosion of the marsh scarp due to the already high strength of the cohesive soil. On the other hand, salt marshes characterized by sandy sediments tend to develop lower cliffs and the dense root mat in the upper part of the scarp significantly contributes to the reduction of local erosion, even though it promotes the formation of cantilever profiles. The latter feature is not represented by the model which, however, is able to reproduce the formation of a steep profile even if the bank is mostly composed by sand (Figure 5.10c). In such a case, when the effect of vegetation on the critical shear stress is not considered, the bank may develop a really flatter profile.

A peculiar aspect of the results is that vegetation does not significantly influence the morphodynamic evolution of the salt marsh, if only its effect on hydrodynamics is accounted for. This seems to be surprising, but it can be explained through the way shear stress erosion develops. The erosion due to bed shear stress initially acts on the shoreward part of the bank and propagates farther landward. At the bank edge vegetation has still not affected the flow field that has still enough energy to promote erosion, whereas, beyond the bank edge, the presence of plants reduces wave energy. Once the plants on the edge are removed, the process continues toward the next cell initially covered by vegetation. A different result would be expected if vegetation would cover the area in front of the cliff, allowing the reduction of the wave energy before it reaches the scarp, as it occurs when salt marsh plants are located in front of a sea dike in order to reduce the maintenance costs [*King* and *Lester*, 1995; *De Oude* et al., 2010; *Van Loon-Steensma*, 2015].

Figure 5.11a summarizes the behaviour of the salt marsh bank subject to wave forcing as a function of the initial mud content (p_m) in the system.

The shift from a cohesive to a non-cohesive system, based on the value of $p_{m,cr}$, is quite mild when no vegetation is present or when only the effect of vegetation on hydrodynamics is considered. When the stabilizing effect of the roots on the soil is considered, the shift between the cohesive and non-cohesive system is more definite. From Figure 5.11a it is seen that, moving from high values of p_m toward $p_{m,cr}$, the effect of vegetation becomes increasingly more pronounced. The trend changes when the initial mud content p_m of the system is lower than the critical mud content $p_{m,cr}$ (occurrence of the avalanching mechanism). The threshold value of $p_{m,cr}$ is based on the studies reported in the literature only for the shear stress erosion [*Van Ledden*, 2003; *Van Ledden* et al., 2004; *Le Hir* et al., 2011]. This means, regarding bank overall stability, the criterion for the occurrence of the avalanching process depends only on the geometry of the scarp and on the initial mud content, that has to be lower than the critical value $p_{m,cr}$ (non-cohesive regime). Indeed, avalanching is activated when the slope of a portion of the scarp is higher than sc_{sl} (see Table 5.4 and [*Vellinga*, 1986; *Roelvink* et al., 2009; *Van Thiel de Vries*, 2009]). At the moment no geotechnical analysis have been carried out in order to identify a critical mud content allowing the bank to maintain a steep cliff. This is a shortcoming of the model and it may likely affect the results for bank compositions with a predominant sand fraction (p_s = 0.6–0.8) and a non negligible mud fraction (p_m = 0.4–0.2). In the case $p_m \geq 0.5$ the predominance of mud allows the presence of steep cliff [*Allen*, 1989], whereas for $p_s \leq 0.2$ the system likely behaves as a sandy beach, that is the type of environment for which XBeach has been initially developed. Future developments should asses also this aspect in order to remove this shortcoming from the model.

The use of the sand-mud mixture model proposed by *Van Ledden* [2003] may, however, lead to some criticisms. Indeed, the model is more suited for long term simulation and it does not account for the effect of eroded and subsequently deposited mud which lost its cohesiveness, and results in a lower critical shear stress. To account for this aspect it has recently been introduce the concept of “fluff-layer” [*Van Kessel* et al., 2012]. However, during the erosion process of the bank edge induced by waves, the deposition rate of the mud is strongly reduced due to the characteristics of the flow and the mud tends to be washed away. For this reason, the erosion of the deposited mud does not likely occur and it is assumed to be negligible for the purpose of the present study. In addition the use of parameters from the literature for the mud erosion rate M_m and critical shear stress τ_m can be considered adequate, since a sensitivity analysis has been carried out and no site-specific forecast are performed.

Another important aspect to be discussed is related to rate at which marsh erosion occurs. For the numerical experiments the salt marsh bank has been subject to six days of continuous wave forcing in order to start with a simple case. However, this kind of uniform wave forcing in time is not fully representative of the wave forcing during a storm surge, which duration is around 2–4 days. Indeed, during a storm surge or a rough sea, the wave height generally tends to increase and then to decrease after a peak is reached. If we consider that the wave height employed in the simulation is equal to the average wave height associated to a time varying rough sea, and we compare the final bank profile for the two cases (uniform and time varying wave height), some differences might be present. The erosion due to wave impact depends on wave power which, in turns, is a function of H_{rms}^2, and the shear erosion depends on u_{rms}^2 (with u_{rms} a linear function of H_{rms}). This non-linearities may affect the final profile, likely increasing the total eroded volume. On the other hand, since erosion is a process based on a certain threshold, a variable wave forcing does not ensure a continuous change in morphology if such a threshold is not exceeded. Regarding the duration, six days of continuous forcing can be equate with a sequence of two or three storm surges, and this aspect would not affect the final bank profile.

In general, a time varying wave forcing may lead to higher eroded volumes, due to the non-linear dependence of erosion on hydrodynamics, with respect to an equivalent one characterized by an average uniform wave height. However, it is possible to argue that the global behaviour of the system, and the characteristics of the final profiles in relation to the different configurations (unvegetated and vegetated bank), tend to remain unchanged. Despite this conclusion, future studies should evaluate the sensitivity of the bank profile to different typologies of wave forcing in order to verify present results.

A sensitivity analysis on the effect of the water level temporal distribution (and then of the water depth) in front of the salt marsh bank would be really useful since this aspect strongly influences the erosion processes [*Mariotti* and *Fagherazzi*, 2013b].

Finally, a systematic model validation has not been carried out since adequate field data to test the model are still lacking and the data collected during the field campaign described in Chapter 4 are not readily suitable. This aspect will be further investigated in the next developments in order to check if the model is capable to perform detailed and reliable site-specific forecasts regarding the fate of the salt marsh banks. Indeed, the model may represent a valuable tool to asses the extent of marsh loss at short temporal and spatial scale for a specific site, especially when engineering projects regarding marsh restoration are planned.

5.4 Summary and concluding remarks

In this chapter, the process based numerical model XBeach [*Roelvink* et al., 2009] has been extended to simulate the lateral retreat of the salt marsh banks due to the effect of wind-induced waves. Several processes have been additionally implemented on the 1-D, phase averaging version of the model:

– the interaction mechanism between sand and mud;

– presence of reflected wave pattern in front of the bank;

– stabilizing effect of salt marsh vegetation (increase of soil resistance to shear erosion);

– effect of wave impact on steep cliffs, including a new approach to update the bed elevation in order to simulate a horizontal erosion rate.

The numerical model is applied as an exploratory tool to carry out a sensitivity analysis on the main parameters characterizing the lateral retreat of salt marsh edges. Numerical experiments are run to investigate the effect of soil and that of vegetation on the bank morphology. The bank has been subject to continuous wave forcing superimposed to tide for six days.

Results of numerical experiments carried out on a bare bank without vegetation shows that a high mud fraction (0.7 and more of the total sediment mass) promotes a lateral migration of the bank, while it roughly maintains its initial shape characterized by a steep scarp. Lowering the mud fraction, the final bed profile tends to flatten and to become more dissipative.

Once vegetation is added on the upper part of the bank (the tidal flat in front remains unvegetated), the dependence of the shape of the final profile on the soil composition is reduced. The higher the mud fraction p_m, the less pronounced is the strengthening effect of plant roots. For really high p_m (0.8–0.9), the effect of vegetation becomes almost negligible. However, for sandy banks, vegetation affects the shear erosion threshold and the final bank profile tends to show a small cliff which does not appear for the unvegetated case.

Future developments need to consider testing model against laboratory and field data, provided that a sufficiently detailed bathymetry of a cross section is available.

Moreover, several improvements can be implemented on the model. The variability of the scarp erosion coefficient M_{sc} will be accounted for, in order to consider a higher erodibility at the toe of the bank that is not protected by vegetation (as shown in Chapter 4), and further research is also needed to investigate the effect of soil composition on M_{sc}. In relation to the previous point, a simple description of mass failure events of cantilever type would be required, since their effect on the lateral erosion rate is now embedded in the value of M_{sc}.

Finally, the modification implemented in XBeach will be extended to the 2-D case.

Chapter 6

Summary, Conclusions and Recommendations

In this chapter, the key results are summarized, including their relevance and limitations. Based on the latter, recommendations for further research are then drawn.

6.1 Summary of key results

The mathematical model for the description of the incipient toppling failure of a block of soil from the salt marsh bank, was developed based on the experimental results of a laboratory study previously carried out. The main findings are listed below.

- Experimental observations showed that tension cracks are crucial in triggering mass failures and that cracks can form slowly due to subsequent tidal cycles, or faster due to wave-induced loads.

- The validation of the model against experimental data showed that the model is able to predict the toppling failure and to identify the group of waves responsible for the final detachment of the unstable blocks in three of the four monitored cases.

- Results of the simulations suggest that the most unfavorable configuration for bank stability is characterized by water filling the crack and low water level in front of the bank.

- Mass failure events are strongly affected by the dynamic response of the system when it is subject to continuous wave forcing. Indeed, a simple static model characterized by an instantaneous response of the system to a given fixed water level, would lead to smaller stresses and more stable conditions.

The field measurement campaign carried out at a salt marsh of the Lagoon of Venice provided the following results.

- The global average retreat rates can reach up to 70–80 cm/yr. There are generally differences among sectors due to the different wind exposure, the local bathymetric features and the possible effect of boat-induced waves. The effect of occasional mass failures can almost double the average retreat rate for a specific sector.

- A clear correlation between wave energy flux and bank erosion rate, at short (monthly) temporal scales, can be found when mass failure events are excluded from the analysis. The inclusion of mass failure events, allows to identify a linear correlation between wave energy flux and bank erosion rate only in case of frequent mass failures.

- The comparison of the present results with those from other studies suggests that the reference time scale for the calculation of the wave energy flux and bank erosion rate plays a significant role in the determination of a relationship between the two quantities.

- The formation of cantilever profiles, as generally observed in the field, can be explained by the higher vulnerability to erosion of the toe with respect to the top of the bank scarp. This difference in erodibility is likely due to the presence of the root mat in the upper bank portion as well as to the local characteristics of the flow field (i.e. high turbulence due wave breaking at the bank toe).

- A simple mathematical model, based on field data and observations, shows that the higher erodibility of bank toe can lead to higher cumulative retreat, as compared to an equivalent case where erodibility is uniformly distributed along the scarp of the salt marsh.

Numerical experiments using the new 1-D hydro-morphodynamic model allowed to identify the peculiarity of the salt marsh bank behaviour subject to continuous and intense wave forcing modulated by tide.

- Results of numerical experiments carried out on a bank of cohesive soil without vegetation show that a high mud (mixture of silt and clay) fraction (70% and more of the total sediment mass) promotes a lateral migration of the bank, while it roughly maintains its initial shape characterized by a steep scarp. If the mud fraction is reduced, the final bed profile tends to flatten and to become more dissipative.

- Once vegetation is added on the upper part of the bank, the effect of soil strengthening against shear erosion is more pronounced when the mud fraction is low. Such an effect becomes almost negligible for muddy banks.

– Vegetated sandy banks develop a final profile characterized by the presence of a small cliff which does not appear for a similar bank without vegetation.

– The total eroded volume can be strongly sensitive to variations of the characteristics of the root mat, after a certain threshold is exceeded.

Additional comments are required in connection with the outcomes presented in the different chapters. Results from Chapter 4 and 5 can be considered complementary even if they may initially appear to be in contrast. On the one hand, the mathematical model developed in Chapter 4 (*cantilever failure model*) shows that the presence of vegetation, strengthening the upper part of the marsh, does not necessarily ensure a lower cumulative retreat. On the other hand, results from numerical experiments carried out with the modified version of XBeach (*hydro-morphodynamic model*), show that the presence of plants reduces the total eroded volume of the final bank profile.

Actually, the *cantilever failure model* does not demonstrate that the presence of vegetation necessarily increases the cumulative lateral retreat. Indeed, given an average erodibility of the marsh scarp, if the toe is more prone to erosion than the top (non-uniform vertical distribution of erodibility), then, all things being equal, the cumulative retreat tends to increase. A representative situation might be the comparison between a muddy bank with a small amount of vegetation and a sandy bank strongly vegetated. The former would have a uniform erodibility along the vertical direction, whereas the latter would be characterized by a more resistant upper layer. Supposing an equivalent average erodibility, the bank mostly composed by sand, even more vegetated, would experience a higher cumulative retreat for the same wave forcing. This is something that is not fully captured by the *hydro-morphodynamic model*, which indeed can consider only a uniform scarp erodibility and, differently from the *cantilever failure model*, accounts for the shear erosion. Nevertheless, the *hydro-morphodynamic model* shows that the presence of vegetation strongly reduces erosion, as compared to a bare bank, even if plants affect the soil resistance only against shear erosion.

To sum up, the outputs from the *hydro-morphodynamic model* demonstrate that vegetation strongly protects the bank from shear erosion, avoiding the formation of smooth profiles and reducing the total eroded volume. This effect is more pronounced if the comparison between a vegetated and unvegetated bank is related to a salt marsh mostly composed by sand. The *cantilever failure model* allows to identify the particular role played by vegetation with respect to wave impact erosion. It can help to protect the bank but, if the toe is particularly prone to erosion, this feature would lead to a higher cumulative retreat.

The results obtained by the *cantilever failure model* and by the *hydro-morphodynamic model* can be then considered complementary. The latter was run considering a single value of bank erodibility M_{sc}. Next developments should investigate the possibility to run the numerical experiments with different values of scarp erodibility $M_{sc,i}$, calculated as multiple of M_{sc} in order to simulate the effect of the non-uniform distribution of the proneness to erosion of different parts of the bank scarp. These values can be easily computed from the output of the *cantilever failure model* as $M_{sc,i} = M_{sc} \cdot \frac{x_{avg,i}}{x_{avg,eq}}$.

6.2 Recommendations and future research

This research study provided several contributions to the current knowledge on the hydro-morphodynamic evolution of the salt marsh edges subject to wave forcing. Some simplifications and assumptions are made in order to deal with a rather complex topic and, new issues arose from the analysis and interpretation of the results.

Laboratory experiments allowed to observe the most relevant physical processes in a controlled environment. Future developments of the model for toppling failure will cover several aspects, i.e., the inclusion of the effect of vegetation on bank stability, the triggering mechanism for tension crack formation, and the 3-D character of the geometry of the unstable soil blocks, including the effect of lateral resisting forces.

Regarding field data, the effects of a single storm surge on bank morphology should be assessed through surveys carried out immediately before and after a strong storm event, while wave height should be directly measured by means of pressure transducers. This could be helpful in order to understand the effect of the reference time scale (decades, years, months, single storm surge) in determining the erodibility of the bank. The role of soil composition should also be investigated, collecting sample of soil at different locations on the monitored marsh. The role of boat induced waves should be better quantified, so that its relative contribution to the erosion rate can be considered. Finally, the influence of different vegetation covers needs to be taken into account in the next studies.

The hydro-morphodynamic model, employed herein in an exploratory way, could be used for simulations at time scales in the order of months. Furthermore, the new method to update the bed elevation in order to simulate the lateral retreat of a bank subject to hydrodynamic forcing, could be extended to other environments, such as coastal cliff or even river banks. Variations in the proneness to erosion for different portions of the scarp should be accounted for in order to attempt to introduce in numerical models the mass failure process of cantilever type. Indeed, a better quantification of the effect of mass failures on bank retreat would be required, since their effect on the lateral erosion rate is now simply embedded in the value the scarp erosion parameter.

Appendix A

Additional Informations on Toppling Failure Model and Related Experiments

A.1 System of ordinary differential equations

In order to solve Equation 3.4, the second order ordinary differential equation is transformed into a system of two ordinary differential equations.

Two variables are initially defined from the value of the angle φ: $\varphi_1 = \varphi$ and $\varphi_2 = d\varphi/dt$. Then, after substitution in Equation 3.4, the following system is obtained:

$$\frac{d\varphi_1}{dt} = \varphi_2 \tag{A.1a}$$

$$\frac{d\varphi_2}{dt} = \frac{1}{I_b}\left[-c_d\varphi_2 - k_{sp}\varphi_1 + f(t) + W_b\frac{l_b}{2}\left(\varphi_{1,0} + \varphi_1\right)\right] \tag{A.1b}$$

with $f(t) = -F_h\frac{Z}{3} + F_{hc}\frac{l_b^*}{3} - F_w(t)Z_w(t)$. Referring to Figure 3.5, I_b is the moment of inertia of the oscillating block, c_d and k_{sp} are respectively the dynamical spring stiffness and the damping coefficient, W_b is the block weight, F_h is the hydrostatic force due to water in front of the bank, F_{hc} is the hydrostatic force due to the water possibly filling the crack and F_w the wave-induced force.

A.2 Determination of Dynamic Spring Stiffness k_{sp} and Damping Coefficient c_d

The solution of Equation 3.4 requires the values of dynamic spring stiffness $k_{sp}(\sigma)$ and damping coefficient $c_d(\sigma)$, where $\sigma = 2\pi/T$ is the wave angular frequency. To determine these quantities, the principles of soil dynamics and soil-foundation interaction are employed. The main assumption is that the failure surface between the failing block and the underlying soil behaves similarly to the contact surface between soil and foundation.

Parameters k_{sp} and c_d are composed by a static and a dynamic contribution, and depend on the frequency of the forcing and the vibrating mechanism [*Gazetas*, 1991]. The static contribution depends on the characteristics of the soil and the foundation (here corresponding to the failure surface maintaining the block attached to the underlying layer). The dynamic contribution also depends on the main frequency of the forcing. First, it is necessary to obtain the static values associated to the two parameters k_{sp}^* and c_d^*. Then, a correction to account for the effect of the external forcing is applied to k_{sp}^* and c_d^*, to get k_{sp} and c_d. For a rectangular surface with dimensions L_b and d_b (with $L_b > d_b$), the static spring stiffness k_{sp}^* is determined by [*Gazetas*, 1991]:

$$k_{sp}^* = \frac{G}{1-\nu_P} I_s^{0.75} \left(\frac{L_b}{d_b}\right)^{0.25} \left(2.4 + 0.5\frac{d_b}{L_b}\right) \tag{A.2}$$

where G is the shear modulus of the soil and ν_P is the Poisson coefficient.

The correction coefficient $K_{sp}(\sigma)$ for the dynamic contribution to the spring stiffness reads:

$$K_{sp}(\sigma) \simeq 1 - 0.2a_0 \tag{A.3}$$

in which $a_0 = \frac{\sigma d_b}{2V_S}$ and V_S is the shear wave velocity. Hence:

$$k_{sp}(\sigma) = k_{sp}^* \cdot K_{sp}(\sigma) \tag{A.4}$$

In order to constraint oscillations, the dynamic stiffness coefficient has been modified. Indeed, the counter-clockwise rotation of the block beyond the initial equilibrium configuration is inhibited due to the presence of water and soil over the crack. For this reason, it is assumed that when angle φ is assigned negative values, k_{sp} tends to exponentially increase, following:

$$k'_{sp} = \begin{cases} k_{sp} \exp\left(-C_\varphi \cdot \varphi\right), & \varphi < 0 \\ k_{sp}, & \varphi \geq 0 \end{cases} \tag{A.5}$$

where C_φ is a constant chosen large enough to avoid significant counter-clockwise rotation. Here, it is assumed $C_\varphi = 5 \cdot 10^3$.

The damping coefficient c_d is determined from:

$$c_d = \rho_s V_{La} I_s C_c(\sigma) \tag{A.6}$$

in which V_{La} is the "Lysmer's analog" wave velocity, and $C_c(\sigma)$ is a correction coefficient depending on the ratio L_b/d_b and a_0 [*Gazetas*, 1991].

Since we are considering a normally consolidated soil with $\nu_P = 0.5$ (undrained load condition in saturated soil), G can be evaluated through the void ratio e_0, a parameter A_s (ranging from 200 to 400) and the confining pressure σ'_{s0} [*Marcuson* and *Wahls*, 1972]:

$$G = A_s f(e_0)\sigma'_{s0} \tag{A.7}$$

with

$$f(e_0) = \frac{(2.97 - e_0)}{1 + e_0} \tag{A.8}$$

and

$$\sigma'_0 = g\rho_s l_b. \tag{A.9}$$

A.3 Pressure measurements during *Pfailbank54* experiment

The measurement of dynamic pressure collected by the pressure transducers (PTs) located within the bank, during the first two minutes of the *Pfailbank54* experiment, are reported in Figure A.1. The numbers of the PTs are referred to Figure 3.3c

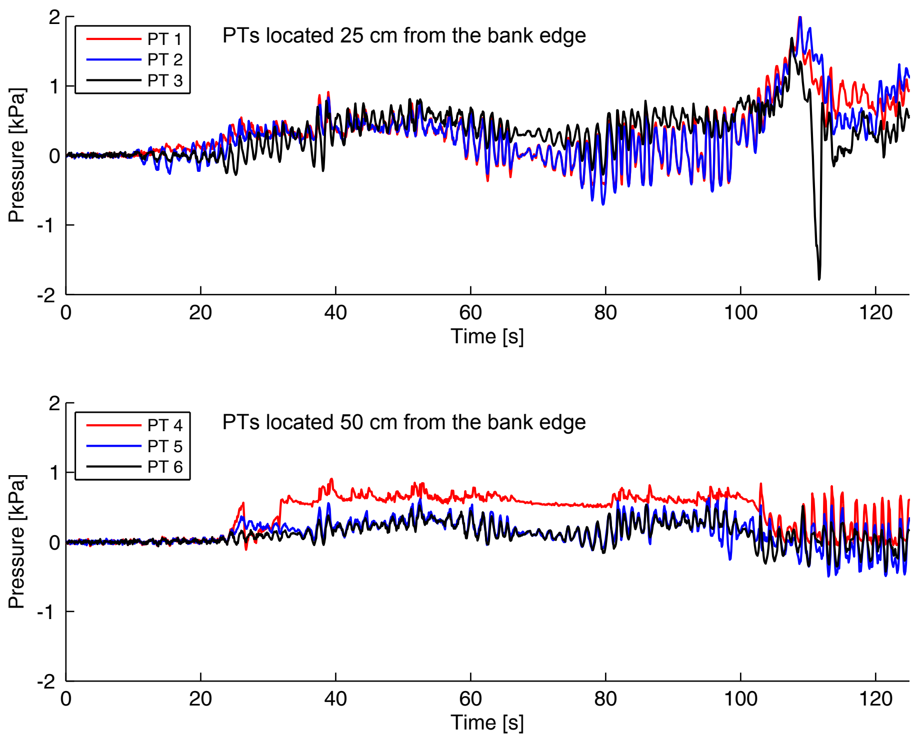

Figure A.1: Dynamic component of the wave-induced pressure within the bank. a) PTs located 25 cm from the bank edge; b) PTs located 50 cm from the bank edge.

Appendix B

Modifications and Extension of XBeach (1D)

B.1 Determination of erosion parameter M_{nc} for non-cohesive mixtures

For non-cohesive mixtures *Van Ledden* [2003] proposed an erosion parameter M_{nc} based on the bed load formula developed by *Van Rijn* [1993]. In this study, an approach similar to the one proposed by *Carniello* et al. [2012] is followed. Erosion and deposition rates are expressed similarly to Equation 5.6:

$$E_s - D_s = (1 - p_m)\, E_s^* - D_s = w_{s,s}\left[(1 - p_m)\, C_{eq,s} - C_s\right] \tag{B.1}$$

assuming $E_s^* = w_{s,s} C_{eq,s}$ and $D_s = w_{s,s} C_s$, $w_{s,s}$ is the sand settling velocity, C_s is the depth-averaged sand concentration, $C_{eq,s}$ the depth-averaged equilibrium sand concentration and p_m the mud fraction.

$C_{eq,s}$ is a depth averaged sediment concentration and can be obtained by the sediment concentration C_a at reference height a_c from the bed [*Van Rijn*, 1993]:

$$q_s = \int_{a_c}^{h} C(z) u(z)\, dz = C_a \bar{u} h F_s\left(\frac{a_c}{h}\right) \tag{B.2}$$

where $\bar{u}$ is a depth averaged velocity and F_s is a shape factor function, depending on a_c/h. Since it is possible to write the suspended load transport as $q_s = C_{eq}\bar{u}h$, it follows that:

$$C_{eq} = C_a \cdot F_s\left(\frac{a_c}{h}\right) \tag{B.3}$$

The concentration at the reference height is obtained through the formulation proposed by *Van Rijn* [1993]:

$$C_a = 0.015 \frac{d_{50} T_{nc}^{1.5}}{a_c d_*^{0.3}} \tag{B.4}$$

where the dimensionless grain size is defined as:

$$d_* = d_{50}\left(\frac{\Delta_s g}{\nu^2}\right)^{1/3} \tag{B.5}$$

with $\Delta_s = \frac{\rho_s-\rho}{\rho}$.

Recalling now Equation 5.13 and the definition of the entrainment rate E_s^* (equation B.1), it is possible to write:

$$\begin{aligned} E_s^* =& w_{s,s}\cdot C_{eq,s} = \\ =& w_{s,s}\cdot C_a \cdot F_s = \\ =& w_{s,s}F_s 0.015\frac{d_{50}}{a_c d_*^{0.3}}T_{nc}^{\alpha_{nc}} = \\ =& \frac{1}{\rho_s}M_{nc}T_{nc}^{\alpha_{nc}}, \end{aligned} \tag{B.6}$$

thus, the erosion parameter for non-cohesive soil mixture is:

$$M_{nc} = \rho_s w_{s,s} F_s 0.015\frac{d_{50}}{a_c d_*^{0.3}} \tag{B.7}$$

According to *Van Rijn* [1993], F_s is in the range 0.1–0.6 (the variation of F_s with a_c/h is reported in Figure 7.3.15, pag. 7.71 of [*Van Rijn*, 1993]; see also Table 7.8, pag 7.56 of the same book for information about the suspended sediment distribution over depth). It is assumed $F_s = 0.15$ and a_c equal to the Nikuradse roughness $k_s = 2.5d_{50}$ [*Soulsby*, 1997]. With above assumptions, the erosion parameter M_{nc} assumes values similar to those provided by other studies [*Waeles* et al., 2007; *Carniello* et al., 2012; *Van Kessel* et al., 2012].

B.2 Determination of critical shear stress $\tau_{cr,v}$ for vegetated soil

In order to obtain Equation 5.35, the following procedure was adopted. First, Equation 5.33, assuming $C_r = 0$ (no vegetation), is substituted into Equation 5.34 to obtain the value of the critical shear stress τ_{cr} in absence of vegetation, instead of $\tau_{cr,v}$. Some algebraic passages lead to:

$$\Psi^2 = \frac{\tau_{cr}}{\frac{1}{2}\rho g\left(\Delta_s g d_a + \frac{1}{\rho}p_m 0.6 C_{cu}\right)}C_{cz}^2 = \left[0.64\log\left(\frac{8.8h}{d_a}\right)\right]^2. \tag{B.8}$$

It is assumed Ψ^2 remains unchanged both with and without vegetation. Then, Equation 5.33 is substituted again into Equation 5.34 but considering the presence of vegetation, obtaining:

$$
\begin{aligned}
\tau_{cr,v} =& \frac{1}{2}\rho g \frac{1}{C_{cz,v}^2}\left[0.64\log\left(\frac{8.8h}{d_a}\right)\right]^2\left[\Delta g d_a + \frac{1}{\rho}\left(0.6C_{cu}+C_r\right)\right] = \\
=& \frac{1}{2}\rho g \frac{1}{C_{cz,v}^2}\Psi^2\left[\Delta g d_a + \frac{1}{\rho}\left(0.6C_{cu}+C_r\right)\right] = \\
=& \tau_{cr}\frac{C_{cz}^2}{C_{cz,v}^2}\left[\frac{\Delta g d_a + \frac{1}{\rho}\left(0.6C_{cu}+C_r\right)}{\Delta g d_a + \frac{1}{\rho}\left(0.6C_{cu}\right)}\right] = \\
=& \tau_{cr}\frac{C_{cz}^2}{C_{cz,v}^2}\left[1+\frac{C_r}{\left(\rho_s-\rho\right)g d_a + 0.6 p_m C_{cu}}\right]
\end{aligned}
\tag{B.9}
$$

which is equivalent to Equation 5.35.

Furthermore, in this way, the dependence of the critical shear stress on the water depth h is removed (it is present only in Equation 5.33). The proposed formulation is then preferable since strong gradients in bed elevation at the marsh scarp can lead to strong gradients in water depth, leading to really high variations of the critical shear stress.

B.3 Determination of RAR from literature data

The procedure to determine the RAR from literature data reduces to the calculation of the ratio of the root volume to the sampling volume. For this reason, it would be more correct to call this quantity root volume ratio. However, assuming a uniform distribution of the roots in the sample volume, and dividing both numerator and denominator by the height of the sample, the ratio between the root are and the sample area is obtained. Since several studies consider the RAR as a quantity to describe the increased soil resistance due to vegetation [*Wu* et al., 1979; *Van der Meer* et al., 2007; *Tuan* and *Oumeraci*, 2012], such a terminology is maintained in this study.

Blum [1993], *Turner* et al. [2004]

The author provides information about belowground biomass b_{bg} in [g/m^2], ranging from 150 to 2600. The depth reached by roots r_d varies from 10 to 40 cm. The ratio b_{bg} to r_d gives the belowground biomass density expressed in [g/m^3]. Based on a root density ρ_{root} = 300 kg/m^3 [*Stanczak* and *Oumeraci*, 2012], it is possible to recover the volume of roots V_{root}. Then, it is assumed roots are homogeneously distributed over soil depth, and the ratio V_{root} to V_{ref} = 1 m^3 is equivalent to the RAR.

Connor and *Chmura* [2000], *Kirwan* and *Guntenspergen* [2012]

The authors provide values of belowground biomass expressed in [mg/cm^3], ranging from 2.5 to 45. Again, using root density it is possible to recover the value of the RAR.

Chen et al. [2012]

In this case the ratio between dry root mass m_{root} and dry sediment mass $m_{s,d}$ is provided [g/g], $r_d = m_{root}/m_{s,d}$. Values range from 0.02 to 0.12. It is assumed that: roots are homogeneously distributed over the soil depth, $V_{root} = m_{root}/\rho_{root}$ and $V_s + V_v = m_{s,d}/\rho_{s,d}$, where V_s and V_v are the sediment and void volumes. Thus:

$$\begin{aligned} RAR = & \frac{V_{root}}{V_s + V_v + V_{root}} = \\ = & \frac{\frac{m_{root}}{\rho_{root}}}{\frac{m_{s,d}}{\rho_{s,d}} + \frac{m_{root}}{\rho_{root}}} = \\ = & \frac{\frac{r_d}{\rho_{root}}}{\frac{1}{\rho_{s,d}} + \frac{r_d}{\rho_{root}}} \end{aligned} \tag{B.10}$$

B.4 Discretizaion of non-linear Exner equation

In this section the discretization procedure of Equation 5.39 with E^*_{sc} given by Equation 5.40 is reported.

First, the equation is written in conservative form:

$$\frac{\partial z_b}{\partial t} + \frac{\partial F(z_b)}{\partial x} = 0 \tag{B.11}$$

with:

$$F(z_b) = \frac{f_{mor}}{1 - n_p} \int_{z_{b,toe}}^{z_b} E^*_{sc}(s)\, ds \tag{B.12}$$

which gives (with $\eta_{toe} = z_{b,toe} + h(x_{toe})$):

$$F(z_b) = \begin{cases} F_{low}, & z_{b,toe} \leq z_b < \eta_{toe} \\ F_{up}, & \eta_{toe} \leq z_b \leq z_{b,top} \end{cases} \tag{B.13}$$

and

$$F_{low} = e_{sc}\left(z_b - z_{b,toe}\right) \tag{B.14a}$$

$$F_{up} = \frac{e_{sc}}{z_{b,top} - \eta_{toe}} \left[-\frac{z_b^2}{2} + z_{b,top}\left(z_b - \eta_{toe}\right) + \frac{\eta_{toe}^2}{2} \right] + e_{sc} h. \tag{B.14b}$$

Equation B.11 is then discretized as follows:

$$z_{b,i}^{n+1} - z_{b,i}^{n+1} = -\frac{\Delta t}{\Delta x} \left(f^n_{i+1/2} - f^n_{i-1/2} \right) \tag{B.15}$$

where $f^n_{i+1/2}$ and $f^n_{i-1/2}$ are the numerical fluxes. To determine them two local Riemann problems have to be resolved at cell interfaces $i-1/2$ and $i+1/2$ with initial conditions $(z_{b,i-1}, z_{b,i})$ and $(z_{b,i}, z_{b,i+1})$ [*LeVeque*, 2002; *Toro*, 2009].

The solution procedure is divided in two steps.

- Step 1. The position of the computational cells with respect to the mean water level is checked and three cases are identified[1]:

$$\eta_{toe} < z_{b,i}, z_{b,i+1}, \qquad \begin{cases} F_L = F_{up}(z_{b,i}) \\ F_R = F_{up}(z_{b,i+1}) \end{cases}$$

$$z_{b,i} \leq \eta_{toe} \leq z_{b,i+1}, \qquad \begin{cases} F_L = F_{low}(z_{b,i}) \\ F_R = F_{up}(z_{b,i+1}) \end{cases}$$

$$z_{b,i}, z_{b,i+1} < \eta_{toe}, \qquad \begin{cases} F_L = F_{low}(z_{b,i}) \\ F_R = F_{low}(z_{b,i+1}). \end{cases}$$

- Step 2. Based on the value of the characteristics speed, that is:

$$\frac{\partial F_L}{\partial x} = E^*_{sc,L} \quad \text{and} \quad \frac{\partial F_R}{\partial x} = E^*_{sc,R}$$

numerical fluxes are determined via the following relations:

$$\text{if} \quad E^*_{sc,L} > E^*_{sc,R} \qquad \begin{aligned} f_{i+1/2} &= \begin{cases} F_L, & S_{sh} \geq 0 \\ F_R, & S_{sh} < 0 \end{cases} \\ S_{sh} &= \frac{F_R - F_L}{z_{b,i+1} - z_{b,i}} \end{aligned} \tag{B.16a}$$

$$\text{if} \quad E^*_{sc,L} \leq E^*_{sc,R} \quad f_{i+1/2} = \begin{cases} F_L, & E^*_{sc,L} > 0 \\ F_R, & E^*_{sc,R} < 0 \\ 0, & E^*_{sc,L} = E^*_{sc,R} = 0. \end{cases} \tag{B.16b}$$

One of the issue related to the present framework is that the value of Δt is determined from the Courant-Friedrics-Levy condition (with $CFL = 0.9$) related to hydrodynamics. In such a case, the maximum velocity is based on the characteristics of the flow field and it is several orders of magnitude larger than the celerity at which the scarp retreat. This gives rise to a significant numerical diffusion in the solution of Equation 5.39, since it is solved employing the same time step. Indeed, it means a really small $CFL = E^*_{sc}\frac{\Delta t}{\Delta x}$ is considered in the solution algorithm. As a consequence, the steepness of the profile can be partially reduced, leading to a smoother bank profile, that for longer simulations might affect significantly the result. A possible way to fix this aspect might be the updating of the scarp of the salt marsh not at every time step but each n time steps, which can be roughly estimated as $n \approx (u + \sqrt{gh})/E^{\star}_{sc}$.

[1] Note that the procedure to determine the extent of the scarp does not allow the scarp contains cells such that $z_{b,i} > z_{b,i+1}$.

B.5 Summary of modifications and extensions of the numerical code

In this part a table containing the name of the modified and new developed subroutines and modules is reported.

Table B.1: Summary of modified and new developed modules and subroutines. (M) modified module or subroutine; (N) new module or subroutine.

Module	Subroutine	Short description
`params` (M)	`all_input` (M)	Description of parameters used in the simulation
`wave_stationary_module` (M)	`wave_stationary` (M)	Wave action balance equation solver
`vegetation_module` (M)	`swvegatt` (M)	Wave energy dissipation due to vegetation
	`bulkdragcoeff` (N)	Determination of bulk drag coefficient for vegetation
`morphevolution` (M)	`transus` (M)	Determination of erosion, deposition, sediment transport (solution of advection-diffusion equation)
	`bed_update` (M)	Update of bed elevation
	`check_the_mass` (N)	Check sediment mass conservation
`sandmud_module` (N)	`sandmud_erodep` (N)	Main subroutine of the module
	`compute_fluxes` (N)	Main subroutine for the determination of erosion and deposition fluxes
	`erosion_par` (N)	Determination of erosion parameters for sand-mud mixtures
	`mud_fraction` (N)	Determination of the mud fraction at a single cell
	`mud_erosion` (N)	Determination of the mud erosion flux in cohesive regime
	`mud_deposition` (N)	Determination of the mud deposition flux
	`sand_erosion` (N)	Determination of the sand erosion flux in non cohesive regime

	settling (N)	Determination of settling velocity
	tau_bed (N)	Determination of the bed shear stress due to wave plus currents
soil_veg_module (N)	tau_soil_veg (N)	Determination of critical shear stress due to the presence of vegetation
reflection_module (M)	submergence (N)	Check if the domain is completely submerged
	boundline (N)	Find the last wet cell at the waterline
	ref_par (N)	Calculation of the reflection coefficient based on local bathymetry and hydrodynamics
	linereg (N)	Determination of the average slope of the bank
	reflected_H (N)	Calculation of the reflected wave height
	reduced_lastwetcell (N)	Reduction of too high values of variables at last wet cell
wave_impact_module (N)	wave_impact (N)	Main subroutine of the module
	retreat_scheme (N)	Implementation of the retreat scheme through modified Exner equation
	lambda_submerged (N)	Calculation of characteristics speed
	lambda_emerged (N)	Calculation of characteristics speed
	flux_submerged (N)	Calculation of numerical flux
	flux_emerged (N)	Calculation of numerical flux
	rankine_hugoniot (N)	Calculation of the speed of the discontinuity
	get_flux (N)	Get the right value of the flux at cell interface
	indentify_scarp (N)	Identification of cells being part of the scarp

	`distr_ero_dry` (N)	Distribution of the eroded material from dry cell of the scarp into the fluid phase
	`wave_energy_flux` (N)	Determination of the wave energy flux leading to the erosion of the bank

Bibliography

Ackers, P. and W.R. White (1973). Sediment transport: new approach and analysis. *Journal of the Hydraulics Division* 99 (hy11).

Adam, P. (1993). *Saltmarsh Ecology*. Cambridge University Press.

Adams, P.N., C.D. Storlazzi, and R.S. Anderson (2005). Nearshore wave-induced cyclical flexing of sea cliffs. *Journal of Geophysical Research: Earth Surface* 110 (F2).

Allen, J.R.L. (1989). Evolution of salt-marsh cliffs in muddy and sandy systems: a qualitative comparison of British west-coast estuaries. *Earth Surface Processes and Landforms* 14 (1), pp. 85–92.

Allen, J.R.L. (2000). Morphodynamics of Holocene salt marshes: a review sketch from the Atlantic and Southern North Sea coasts of Europe. *Quaternary Science Reviews* 19 (12), pp. 1155–1231.

Allen, J.R.L. and K. Pye (1992). *Saltmarshes: morphodynamics, conservation, and engineering significance*. Cambridge University Press.

Alsina, J.M. and T.E. Baldock (2007). Improved representation of breaking wave energy dissipation in parametric wave transformation models. *Coastal Engineering* 54 (10), pp. 765–769.

Amini, M., A. Majdi, and Ö. Aydan (2009). Stability analysis and the stabilisation of flexural toppling failure. *Rock Mechanics and Rock Engineering* 42 (5), pp. 751–782.

Amos, C.L., G. Umgiesser, C. Ferrarin, C.E.L. Thompson, RJS Whitehouse, TF Sutherland, and A Bergamasco (2010). The erosion rates of cohesive sediments in Venice lagoon, Italy. *Continental Shelf Research* 30 (8), pp. 859–870.

Andrews, D Gr and ME McIntyre (1978). An exact theory of nonlinear waves on a Lagrangian-mean flow. *Journal of Fluid Mechanics* 89 (04), pp. 609–646.

Armanini, A. (1995). Non-uniform sediment transport: dynamics of the active layer. *Journal of Hydraulic Research* 33 (5), pp. 611–622.

Augustin, L.N., J.L. Irish, and P. Lynett (2009). Laboratory and numerical studies of wave damping by emergent and near-emergent wetland vegetation. *Coastal Engineering* 56 (3), pp. 332–340.

Bagnold, R.A. (1966). An approach to the sediment transport problem from general physics. *Geological Survey Prof.* 422-I.

Baldock, T.E., P. Holmes, S. Bunker, and P. Van Weert (1998). Cross-shore hydrodynamics within an unsaturated surf zone. *Coastal Engineering* 34 (3), pp. 173–196.

Barbier, E.B., S.D. Hacker, C. Kennedy, E.W. Koch, A.C. Stier, and B.R. Silliman (2011). The value of estuarine and coastal ecosystem services. *Ecological Monographs* 81 (2), pp. 169–193.

Barbier, E.B., E.W. Koch, B.R. Silliman, S.D. Hacker, E. Wolanski, J. Primavera, E.F. Granek, S. Polasky, S. Aswani, L.A. Cramer, et al. (2008). Coastal ecosystem-based management with nonlinear ecological functions and values. *science* 319 (5861), pp. 321–323.

Battjes, JA.. (1974). Surf similarity. *Coastal Engineering Proceedings* 1 (14).

Battjes, J.A. and J.P.F.M. Janssen (1978). Energy loss and set-up due to breaking of random waves. *Coastal Engineering Proceedings* 1 (16).

Bendoni, M. (2011). Analisi Sperimentale sull'Erosione delle Barene Lagunari (in Italian). In Italian. MA thesis. Department of Civil and Environmental Engineering, University of Florence.

Bird, P.A.D. (1993). Measurement and analysis of sea waves near a reflective structure. PhD thesis. University of Plymouth.

Bishop, C.T. and M.A. Donelan (1987). Measuring waves with pressure transducers. *Coastal Engineering* 11 (4), pp. 309–328.

Blum, L.K. (1993). Spartina alterniflora root dynamics in a Virginia marsh. *Marine Ecology Progress Series* 102, p. 697178.

Boesch, D.F. and R.E. Turner (1984). Dependence of fishery species on salt marshes: the role of food and refuge. *Estuaries* 7 (4), pp. 460–468.

Booij, N., R.C. Ris, and L.H. Holthuijsen (1999). A third-generation wave model for coastal regions: 1. Model description and validation. *Journal of Geophysical Research: Oceans* 104 (C4), pp. 7649–7666.

Boorman, L.A. (2003). *Saltmarsh Review. An overview of coastal saltmarshes, their dynamic and sensitivity characteristics for conservation and management.* JNCC Report 334.

Bouma, T.J., M.B. De Vries, E. Low, G. Peralta, I.C. Tanczos, J. van de Koppel, and P.M.J. Herman (2005). Trade-offs related to ecosystem engineering: a case study on stiffness of emerging macrophytes. *Ecology* 86 (8), pp. 2187–2199.

Breugem, W.A. and L.H. Holthuijsen (2007). Generalized shallow water wave growth from Lake George. *Journal of waterway, port, coastal, and ocean engineering* 133 (3), pp. 173–182.

Callaghan, D.P., T.J. Bouma, P. Klaassen, D. Van der Wal, M.J.F. Stive, and P.M.J. Herman (2010). Hydrodynamic forcing on salt-marsh development: Distinguishing the relative importance of waves and tidal flows. *Estuarine, Coastal and Shelf Science* 89 (1), pp. 73–88.

Carniello, L., A. Defina, and L. D'Alpaos (2009). Morphological evolution of the Venice lagoon: Evidence from the past and trend for the future. *Journal of Geophysical Research: Earth Surface* 114 (F4).

Carniello, L., A. Defina, and L. D'Alpaos (2012). Modeling sand-mud transport induced by tidal currents and wind waves in shallow microtidal basins: Application to the Venice Lagoon (Italy). *Estuarine, Coastal and Shelf Science* 102, pp. 105–115.

Carniello, L., A. Defina, S. Fagherazzi, and L. D'alpaos (2005). A combined wind wave–tidal model for the Venice lagoon, Italy. *Journal of Geophysical Research: Earth Surface* 110 (F4).

Castedo, R., M. Fernández, A.S. Trenhaile, and C. Paredes (2013). Modeling cyclic recession of cohesive clay coasts: effects of wave erosion and bluff stability. *Marine Geology* 335, pp. 162–176.

Cavaleri, L. (1980). Wave measurement using pressure transducer. *Oceanologica Acta* 3 (3), pp. 339–346.

Chapman, V.J. (1974). Salt marshes and salt deserts of the world. *Ecology of Halophytes*. Ed. by R.J. Reimold and W.H. Queen. Academic Press, Inc. Chap. 1.

Chauhan, P.P.S. (2009). Autocyclic erosion in tidal marshes. *Geomorphology* 110 (3), pp. 45–57.

Chellew, E., K. Rossington, I. Townend, C. Amos, and S. Richardson (2011). The significance of wave reflection on the morphology of intertidal mudflats. *Coastal Engineering Proceedings* 1 (32), sediment–50.

Chen, Y., C.E.L. Thompson, and M.B. Collins (2012). Saltmarsh creek bank stability: Biostabilisation and consolidation with depth. *Continental Shelf Research* 35, pp. 64–74.

Chmura, G.L., S.C. Anisfeld, D.R. Cahoon, and J.C. Lynch (2003). Global carbon sequestration in tidal, saline wetland soils. *Global biogeochemical cycles* 17 (4).

Cola S.and Sanavia, L., P. Simonini, and B.A. Schrefler (2008). Coupled thermohydromechanical analysis of Venice lagoon salt marshes. *Water Resources Research* 44 (5).

Cole, P. and G.V. Miles (1983). Two-dimensional model of mud transport. *Journal of Hydraulic Engineering* 109 (1), pp. 1–12.

Connor, R. and G.L. Chmura (2000). Dynamics of above-and belowground organic matter in a high latitude macrotidal saltmarsh. *Marine Ecology. Progress series* 204, pp. 101–110.

Cooley, J.W. and J.W. Tukey (1965). An algorithm for the machine calculation of complex Fourier series. *Mathematics of Computation* 19 (90), pp. 297–301.

Coops, H., N. Geilen, H.J. Verheij, R. Boeters, and G. Van der Velde (1996). Interactions between waves, bank erosion and emergent vegetation: an experimental study in a wave tank. *Aquatic Botany* 53 (3), pp. 187–198.

Costanza, R., O. Pérez-Maqueo, M.L. Martinez, P. Sutton, S.J. Anderson, and K. Mulder (2008). The value of coastal wetlands for hurricane protection. *AMBIO: A Journal of the Human Environment* 37 (4), pp. 241–248.

Costanza, R., M. Wilson, A. Troy, A. Voinov, S. Liu, and J. D'Agostino (2006). *The Value of New Jersey's Ecosystem Services and Natural Capital*. Tech. rep. New Jersey Department of Environmental Protection.

Costanza, R., R. d'Arge, R. de Groot, S. Farber, M. Grasso, B. Hannon, K. Limburg, S. Naeem, R.V. O'Neill, J. Paruelo, et al. (1997). The value of the world's ecosystem services and natural capital. *Nature* 38.

Council of European Union (1992). Council directive 92/43/EEC of 21 May 1992 on the conservation of natural habitats and of wild fauna and flora. *Official Journal of the European Communities*.

Cushman-Roisin, B., M. Gacic, P.-M. Poulain, and A. Artegiani (2013). *Physical oceanography of the Adriatic Sea: past, present and future*. Springer Science & Business Media.

Da Lio, C., A. D'Alpaos, and M. Marani (2013). The secret gardener: vegetation and the emergence of biogeomorphic patterns in tidal environments. *Philosophical Transactions of the Royal Society of London A: Mathematical, Physical and Engineering Sciences* 371 (2004), p. 20120367.

D'Alpaos, A., S. Lanzoni, M. Marani, and A. Rinaldo (2007). Landscape evolution in tidal embayments: modeling the interplay of erosion, sedimentation, and vegetation dynamics. *Journal of Geophysical Research: Earth Surface* 112 (F1).

D'Alpaos, Luigi (2010). *Fatti e misfatti di idraulica lagunare: la laguna di Venezia dalla diversione dei fiumi alle nuove opere alle bocche di porto*. Istituto Veneto di Scienze, Lettere ed Arti.

Dalrymple, R.A., J.T. Kirby, and P.A. Hwang (1984). Wave diffraction due to areas of energy dissipation. *Journal of Waterway, Port, Coastal, and Ocean Engineering* 110 (1), pp. 67–79.

Dalrymple, R.A. and B.D. Rogers (2006). Numerical modeling of water waves with the SPH method. *Coastal engineering* 53 (2), pp. 141–147.

Darby, S.E., D. Gessler, and C.R. Thorne (2000). Computer program for stability analysis of steep, cohesive riverbanks. *Earth Surface Processes and Landforms* 25 (2), pp. 175–190.

Darby, S.E. and C.R. Thorne (1996). Development and testing of riverbank-stability analysis. *Journal of hydraulic engineering* 122 (8), pp. 443–454.

Davidson, M.A., P.A.D. Bird, G.N. Bullock, and D.A. Huntley (1996). A new non-dimensional number for the analysis of wave reflection from rubble mound breakwaters. *Coastal Engineering* 28 (1), pp. 93–120.

Day, J.W., F. Scarton, A. Rismondo, and D. Are (1998). Rapid deterioration of a salt marsh in Venice Lagoon, Italy. *Journal of Coastal Research*, pp. 583–590.

Day, J.W., D.F. Boesch, E.J. Clairain, G.P. Kemp, S.B. Laska, W.J. Mitsch, K. Orth, H. Mashriqui, D.J. Reed, L. Shabman, et al. (2007). Restoration of the Mississippi Delta: lessons from hurricanes Katrina and Rita. *science* 315 (5819), pp. 1679–1684.

De Groot, R.S., M.A. Wilson, and R.M.J. Boumans (2002). A typology for the classification, description and valuation of ecosystem functions, goods and services. *Ecological economics* 41 (3), pp. 393–408.

De Oude, R., D.C.M. Augustijn, K.M. Wijnberg, F. Dekker, M.B. De Vries, and T. Suzuki (2010). Bioengineering in front of a River dike: wave attenuation by vegetation. *Environmental Hydraulics. Proceedings of the 6th International Symposium on Environmental Hydraulics*. Vol. 1, pp. 253–258.

De Vriend, H.J. and M. Van Koningsveld (2012). Building with Nature: Thinking, acting and interacting differently.

Dean, R.G. and R.A. Dalrymple (1991). *Water Wave Mechanics for Engineers and Scientists*. Ed. by Philip L.-F.L. Vol. 2. Advanced Series on Ocean Engineering. World Scientific.

Defina, A. (2000). Two-dimensional shallow flow equations for partially dry areas. *Water Resources Research* 36 (11), pp. 3251–3264.

Deltares (2014). *Delft3D-Flow User Manual*. 3.15.34158. Deltares.

Dingemans, M.W. (1997). *Water wave propagation over uneven bottoms: Linear wave propagation*. Ed. by Philip L.-F.L. Vol. 13. Advanced Series on Ocean Engineering. World Scientific.

Erikson, L.H., M. Larson, and H. Hanson (2007). Laboratory investigation of beach scarp and dune recession due to notching and subsequent failure. *Marine Geology* 245 (1), pp. 1–19.

Exner, F.M. (1920). Zur physik der dunen. *Akad. Wiss. Wien Math. Naturwiss. Klasse* 129 (2a), pp. 929–952.

Fagherazzi, S., L. Carniello, L. D'Alpaos, and A. Defina (2006). Critical bifurcation of shallow microtidal landforms in tidal flats and salt marshes. *Proceedings of the National Academy of Sciences* 103 (22), pp. 8337–8341.

Fagherazzi, S. and D.J. Furbish (2001). On the shape and widening of salt marsh creeks. *Journal of Geophysical Research: Oceans* 106 (C1), pp. 991–1003.

Fagherazzi, S., G. Mariotti, P. Wiberg, and K. McGlathery (2013). Marsh collapse does not require sea level rise. *Oceanography* 26 (3), pp. 70–77.

Fagherazzi, S., M.L. Kirwan, S.M. Mudd, G.R. Guntenspergen, S. Temmerman, A. D'Alpaos, J. Koppel, J.M. Rybczyk, E. Reyes, C. Craft, et al. (2012). Numerical models of salt marsh evolution: Ecological, geomorphic, and climatic factors. *Reviews of Geophysics* 50 (1).

Feagin, R.A., J.L. Irish, I. Möller, A.M. Williams, R.J. Colón-Rivera, and M.E. Mousavi (2009). Does vegetation prevent wave erosion of salt marsh edges? *Proceedings of the National Academy of Sciences* 106 (25), pp. 10109–10113.

Flemming, B.W. (2000). A revised textural classification of gravel-free muddy sediments on the basis of ternary diagrams. *Continental Shelf Research* 20 (10), pp. 1125–1137.

Francalanci, S., M. Bendoni, M. Rinaldi, and L. Solari (2013). Ecomorphodynamic evolution of salt marshes: Experimental observations of bank retreat processes. *Geomorphology* 195, pp. 53–65.

French, G.T. (1990). Historical shoreline changes in response to environmental conditions in west Delaware Bay. MA thesis. University of Maryland College Park.

French, J. (2006). Tidal marsh sedimentation and resilience to environmental change: exploratory modelling of tidal, sea-level and sediment supply forcing in predominantly allochthonous systems. *Marine Geology* 235 (1), pp. 119–136.

Friedrichs, C.T. and J.E. Perry (2001). Tidal salt marsh morphodynamics: a synthesis. *Journal of Coastal Research*, pp. 7–37.

Gabet, E.J. (1998). Lateral migration and bank erosion in a saltmarsh tidal channel in San Francisco Bay, California. *Estuaries* 21 (4), pp. 745–753.

Galappatti, R. (1983). *A depth integrated model for suspended transport*. Tech. rep. TU-Delft, Delft University of Technology.

Gazetas, G. (1991). Foundation Engineering Handbook. Ed. by H.I. Fang. Kliwer Academic Publishers, Massachusetts, U.S.A. Chap. 15 Foundation Vibrations, pp. 553–593.

Gedan, K.B., B.R. Silliman, and M.D. Bertness (2009). Centuries of human-driven change in salt marsh ecosystems. *Annual Review of Marine Science* 1, pp. 117–141.

Gedan K.B.and Kirwan, M.L., E. Wolanski, E.B. Barbier, and B.R. Silliman (2011). The present and future role of coastal wetland vegetation in protecting shorelines: answering recent challenges to the paradigm. *Climatic Change* 106 (1), pp. 7–29.

Goda, Y. and T. Suzuki (1976). Estimation of incident and reflected waves in random wave experiments. *Coastal Engineering Proceedings* 1 (15).

Goodman, R.E. and J.W. Bray (1976). Toppling of rock slopes. *Rock Engineering for Foundations and Slopes*. ASCE, pp. 201–234.

Gosselink, J.G. and R.M. Pope (1974). The Value Of The Tidal Marsh. (LSU-SG-74-03).

Gray, D.H., A.T. Leiser, et al. (1982). *Biotechnical slope protection and erosion control.* Van Nostrand Reinhold Company Inc.

Hasselmann, K., T.P. Barnett, E. Bouws, H. Carlson, D.E. Cartwright, K. Enke, J.A. Ewing, H. Gienapp, D.E. Hasselmann, P. Kruseman, et al. (1973). *Measurements of wind-wave growth and swell decay during the Joint North Sea Wave Project (JONSWAP)*. Tech. rep. Deutches Hydrographisches Institut.

Hirano, M. (1971). River degradation with armouring. *Transaction of JSCE* 3 (2), pp. 194–195.

Holthuijsen, L.H. (2007). *Waves in oceanic and coastal waters.* Cambridge University Press.

Houser, C. (2010). Relative importance of vessel-generated and wind waves to salt marsh erosion in a restricted fetch environment. *Journal of Coastal Research*, pp. 230–240.

Howes, N.C., D.M. FitzGerald, Z.J. Hughes, I.Y. Georgiou, M.A. Kulp, M.D. Miner, J.M. Smith, and J.A. Barras (2010). Hurricane-induced failure of low salinity wetlands. *Proceedings of the National Academy of Sciences* 107 (32), pp. 14014–14019.

Hughes, S.A. (1993). *Physical models and laboratory techniques in coastal engineering.* Vol. 7. World Scientific.

Jacobs, W., P. Le Hir, W. Van Kesteren, and P. Cann (2011). Erosion threshold of sand–mud mixtures. *Continental Shelf Research* 31 (10), S14–S25.

Jadhav, R.S., Q. Chen, and J.M. Smith (2013). Spectral distribution of wave energy dissipation by salt marsh vegetation. *Coastal Engineering* 77, pp. 99–107.

Janssen, T.T. and J.A. Battjes (2007). A note on wave energy dissipation over steep beaches. *Coastal Engineering* 54 (9), pp. 711–716.

Jones, N.L. and S.G. Monismith (2007). Measuring short-period wind waves in a tidally forced environment with a subsurface pressure gauge. *Limnology and Oceanography: Methods* 5 (10), pp. 317–327.

Keulegan, G.H. and L.H. Carpenter (1958). Forces on cylinders and plates in an oscillating fluid. *Journal of Research of the National Bureau of Standards* 60 (5).

King, S.E. and J.N. Lester (1995). The value of salt marsh as a sea defence. *Marine Pollution Bulletin* 30 (3), pp. 180–189.

Kirwan, M. and S. Temmerman (2009). Coastal marsh response to historical and future sea-level acceleration. *Quaternary Science Reviews* 28 (17), pp. 1801–1808.

Kirwan, M.L. and G.R. Guntenspergen (2012). Feedbacks between inundation, root production, and shoot growth in a rapidly submerging brackish marsh. *Journal of Ecology* 100 (3), pp. 764–770.

Kirwan, M.L., G.R. Guntenspergen, A. D'Alpaos, J.T. Morris, S.M. Mudd, and S. Temmerman (2010). Limits on the adaptability of coastal marshes to rising sea level. *Geophysical Research Letters* 37 (23).

Krone, R.B. (1962). *Flume studies of the transport of sediment in estuarial shoaling processes.* Tech. rep. Hydraulic Engineering Laboratory and Sanitary Engineering Research Laboratory, University of California, Berkeley, USA.

Langhaar, H. (1951). *Dimensional Analysis and Theory of Models.* Ed. by New York Wiley.

Larson, M., L. Erikson, and H. Hanson (2004). An analytical model to predict dune erosion due to wave impact. *Coastal Engineering* 51 (8), pp. 675–696.

Larson, M. and N.C. Kraus (1989). *SBEACH: Numerical Model for Simulating Storm-Induced Beach Change; Report 1: Empirical Foundation and Model Development.* Tech. rep. US Army Corps of Engineers, USAEWES, Coastal Engineering Research Center.

Le Hir, P., F. Cayocca, and B. Waeles (2011). Dynamics of sand and mud mixtures: a multiprocess-based modelling strategy. *Continental Shelf Research* 31 (10), S135–S149.

Le Hir, P., Y. Monbet, and F. Orvain (2007). Sediment erodability in sediment transport modelling: Can we account for biota effects? *Continental Shelf Research* 27 (8), pp. 1116–1142.

Lee, D.-Y. and H. Wang (1984). Measurement of surface waves from subsurface gage. *Coastal Engineering Proceedings* 1 (19).

Leonardi, N. and S. Fagherazzi (2014). How waves shape salt marshes. *Geology* 42 (10), pp. 887–890.

Lesser, G.R., J.A. Roelvink, J.A.T.M. Van Kester, and G.S. Stelling (2004). Development and validation of a three-dimensional morphological model. *Coastal Engineering* 51 (8), pp. 883–915.

LeVeque, R.J. (2002). *Finite Volume Methods for Hyperbolic Problems.* Vol. 31. Cambridge University Press.

Lin, P. and P.L.-F. Liu (1998). A numerical study of breaking waves in the surf zone. *Journal of fluid mechanics* 359, pp. 239–264.

Madsen, P.A., R. Murray, and O.R. Sørensen (1991). A new form of the Boussinesq equations with improved linear dispersion characteristics. *Coastal engineering* 15 (4), pp. 371–388.

Malkin, A.Y. and A.Y. Isayev (2006). *Rheological Concepts, Methods and Applications.* ChemTech, Toronto.

Marani, M., A. D'Alpaos, S. Lanzoni, L. Carniello, and A. Rinaldo (2010). The importance of being coupled: Stable states and catastrophic shifts in tidal biomorphodynamics. *Journal of Geophysical Research: Earth Surface* 115 (F4).

Marani, M., A. D'Alpaos, S. Lanzoni, and M. Santalucia (2011). Understanding and predicting wave erosion of marsh edges. *Geophysical Research Letters* 38 (21).

Marcuson, W.F. and H.E. Wahls (1972). Time effects on dynamic shear modulus of clays. *Journal of the Soil Mechanics and Foundations Division* 98 (12), pp. 1359–1373.

Mariotti, G. and J. Carr (2014). Dual role of salt marsh retreat: Long-term loss and short-term resilience. *Water Resources Research* 50 (4), pp. 2963–2974.

Mariotti, G. and S. Fagherazzi (2010). A numerical model for the coupled long-term evolution of salt marshes and tidal flats. *Journal of Geophysical Research: Earth Surface* 115 (F1).

Mariotti, G. and S. Fagherazzi (2013). Critical width of tidal flats triggers marsh collapse in the absence of sea-level rise. *Proceedings of the national Academy of Sciences* 110 (14), pp. 5353–5356.

Mariotti, G. and S. Fagherazzi (2013). Wind waves on a mudflat: The influence of fetch and depth on bed shear stresses. *Continental Shelf Research* 60, S99–S110.

Maurmeyer, E.M. (1978). Geomorphology and evolution of transgressive estuarine washover bbarrier along the western shore of Delaware Bay. PhD thesis. University of Delaware, Newark.

McAnally, W.H. and A.J. Mehta (2003). *Coastal and Estuarine Fine Sediment Processes*. Vol. 3. Proceedings in Marine Science. Elsevier.

McLoughlin, S.M., P.L. Wiberg, I. Safak, and K.J. McGlathery (2014). Rates and forcing of marsh edge erosion in a shallow coastal bay. *Estuaries and Coasts*, pp. 1–19.

Mendez, F.J. and I.J. Losada (2004). An empirical model to estimate the propagation of random breaking and nonbreaking waves over vegetation fields. *Coastal Engineering* 51 (2), pp. 103–118.

Mirtskhoulava, T.E. (1991). Scouring by flowing water of cohesive and noncohesive beds. *Journal of Hydraulic Research* 29 (3), pp. 341–354.

Mitchener, H. and H. Torfs (1996). Erosion of mud/sand mixtures. *Coastal engineering* 29 (1), pp. 1–25.

Mol, A.S.C. (2003). *Wave attenuation by vegetation*. Tech. rep. Z2837. Deltares.

Möller, I. (2006). Quantifying saltmarsh vegetation and its effect on wave height dissipation: Results from a UK East coast saltmarsh. *Estuarine, Coastal and Shelf Science* 69 (3), pp. 337–351.

Möller, I. and T. Spencer (2002). Wave dissipation over macro-tidal saltmarshes: Effects of marsh edge typology and vegetation change. *Journal of Coastal Research* 36 (1), pp. 506–521.

Möller, I., T. Spencer, J.R. French, D.J. Leggett, and M. Dixon (1999). Wave transformation over salt marshes: a field and numerical modelling study from North Norfolk, England. *Estuarine, Coastal and Shelf Science* 49 (3), pp. 411–426.

Möller, I., M. Kudella, F. Rupprecht, T. Spencer, M. Paul, B.K. van Wesenbeeck, G. Wolters, K. Jensen, T.J. Bouma, M. Miranda-Lange, et al. (2014). Wave attenuation over coastal salt marshes under storm surge conditions. *Nature Geoscience* 7 (10), pp. 727–731.

Morris, J.T., P.V. Sundareshwar, C.T. Nietch, B. Kjerfve, and D.R. Cahoon (2002). Responses of coastal wetlands to rising sea level. *Ecology* 83 (10), pp. 2869–2877.

Morris, P.H., J. Graham, and D.J. Williams (1992). Cracking in drying soils. *Canadian Geotechnical Journal* 29 (2), pp. 263–277.

Murray, W.A. (1977). Erodibility of coarse sand-clayey silt mixtures. *Journal of Hydraulic Engineering* 103 (10), pp. 1222–1227.

Nishi, R. and N.C. Kraus (1996). Mechanism and calculation of sand dune erosion by storms. *Coastal Engineering Proceedings* 1 (25).

Ojea, E., J. Martin-Ortega, and A. Chiabai (2012). Defining and classifying ecosystem services for economic valuation: the case of forest water services. *Environmental Science & Policy* 19, pp. 1–15.

Oumeraci, H. and A. Kortenhaus (1994). Analysis of the dynamic response of caissons breakwaters. *Coastal Engineering* 22, pp. 159–183.

Ozeren, Y., D.G. Wren, and W. Wu (2013). Experimental investigation of wave attenuation through model and live vegetation. *Journal of Waterway, Port, Coastal, and Ocean Engineering* 140 (5).

Paarlberg, A.J., M.A.F. Knaapen, M.B. de Vries, S.J.M.H. Hulscher, and Z.B. Wang (2005). Biological influences on morphology and bed composition of an intertidal flat. *Estuarine, Coastal and Shelf Science* 64 (4), pp. 577–590.

Paola, C. and V.R. Voller (2005). A generalized Exner equation for sediment mass balance. *Journal of Geophysical Research: Earth Surface* 110 (F4).

Parker, G. (1990). Surface-based bedload transport relation for gravel rivers. *Journal of Hydraulic Research* 28 (4), pp. 417–436.

Parker, G., C. Paola, and S. Leclair (2000). Probabilistic Exner sediment continuity equation for mixtures with no active layer. *Journal of Hydraulic Engineering* 126 (11), pp. 818–826.

Partheniades, E. (1965). Erosion and deposition of cohesive soils. *Journal of the Hydraulics Division, ASCE* 91 (1), pp. 105–139.

Phillips, J.D. (1985). AspatBay analysis of the shoreline erosion, Delaware Bay, New Jersey. PhD thesis. Rutgers University, New Brunswick.

Pranovi, F., S. Libralato, S. Raicevich, A. Granzotto, R. Pastres, and O. Giovanardi (2003). Mechanical clam dredging in Venice lagoon: ecosystem effects evaluated with a trophic mass-balance model. *Marine Biology* 143 (2), pp. 393–403.

Priestas, A.M. and S. Fagherazzi (2011). Morphology and hydrodynamics of wave-cut gullies. *Geomorphology* 131 (1), pp. 1–13.

Pringle, A.W. (1995). Erosion of a cyclic saltmarsh in Morecambe Bay, northwest England. *Earth Surface Processes and Landforms* 20 (5), pp. 387–405.

Raudkivi, A.J. (1990). *Loose Boundary Hydraulics.* 3rd. Oxford: Pergamon Press.

Ravera, O. (2000). The Lagoon of Venice: the result of both natural factors and human influence. *Journal of Limnology* 59 (1), pp. 19–30.

Ribberink, J.S. (1987). Mathematical modelling of one-dimensional morphological changes in rivers with non-uniform sediment. PhD thesis. Delft University of Technology, Delft.

Riffe, K.C., S.M. Henderson, and J.C. Mullarney (2011). Wave dissipation by flexible vegetation. *Geophysical Research Letters* 38 (18).

Rinaldi, M. and N. Casagli (1999). Stability of streambanks formed in partially saturated soils and effects of negative pore water pressures: the Sieve River (Italy). *Geomorphology* 26 (4), pp. 253–277.

Rinaldo, A., S. Fagherazzi, S. Lanzoni, M. Marani, and W.E. Dietrich (1999). Tidal networks 2. Watershed delineation and comparative network morphology. *Water Resources Research* 35 (12), pp. 3905–3917.

Roelvink, D., A. Reniers, A.P. Van Dongeren, J. Van Thiel de Vries, R. McCall, and J. Lescinski (2009). Modelling storm impacts on beaches, dunes and barrier islands. *Coastal Engineering* 56 (11), pp. 1133–1152.

Roelvink, J.A. (1993). Dissipation in random wave groups incident on a beach. *Coastal Engineering* 19 (1), pp. 127–150.

Roelvink, J.A. (2006). Coastal morphodynamic evolution techniques. *Coastal Engineering* 53 (2), pp. 277–287.

Sarretta, A., S. Pillon, E. Molinaroli, S. Guerzoni, and G. Fontolan (2010). Sediment budget in the Lagoon of Venice, Italy. *Continental Shelf Research* 30 (8), pp. 934–949.

Saville, T. (1954). *The effect of fetch width on wave generation.* Technical Memorandum 70. Beach Erosion Board, Washington DC.

Schwimmer, R.A. (2001). Rates and processes of marsh shoreline erosion in Rehoboth Bay, Delaware, USA. *Journal of Coastal Research*, pp. 672–683.

Seelig, W.N. and J.P. Ahrens (1981). *Estimation of wave reflection and energy dissipation coefficients for beaches, revetments, and breakwaters.* Tech. rep. DTIC Document.

Selby, M.J. (1993). *Hillslope Materials and Processes.* Oxford University Press.

Shepard, C.C., C.M. Crain, and M.W. Beck (2011). The protective role of coastal marshes: a systematic review and meta-analysis. *PLoS One* 6 (11), e27374.

Shields, A. (1936). Anwendung der Aehnlichkeitsmechanik und der Turbulenzforschung auf die Geschiebebewegung. In German. PhD thesis. Technischen Hochschule, Berlin.

Silliman, B.R., J. Van de Koppel, M.W. McCoy, J. Diller, G.N. Kasozi, K. Earl, P.N. Adams, and A.R. Zimmerman (2012). Degradation and resilience in Louisiana salt marshes after the BP–Deepwater Horizon oil spill. *Proceedings of the National Academy of Sciences* 109 (28), pp. 11234–11239.

Singh, A., K. Fienberg, D.J. Jerolmack, J. Marr, and E. Foufoula-Georgiou (2009). Experimental evidence for statistical scaling and intermittency in sediment transport rates. *Journal of Geophysical Research: Earth Surface* 114 (F1).

Solidoro, C., V. Bandelj, F.A. Bernardi, E. Camatti, S. Ciavatta, G. Cossarini, C. Facca, P. Franzoi, S. Libralato, D.M. Canu, et al. (2010). Response of the Venice Lagoon Ecosystem to Natural and Anthropogenic Pressures over the Last 50 Years. *Coastal Lagoons: Critical Habitats of Environmental Change.* Ed. by Michael J. Kennish. CRC Press. Chap. 19.

Soulsby, R. (1997). *Dynamics of marine sands: a manual for practical applications.* Thomas Telford.

Stanczak, G. and H. Oumeraci (2012). Modeling sea dike breaching induced by breaking wave impact-laboratory experiments and computational model. *Coastal Engineering* 59 (1), pp. 28–37.

Steetzel, H.J. (1993). Cross-shore transport during storm surges. PhD thesis. Technical University Delft.

Stokes, G.G. (1847). On the theory of oscillatory waves. *Transaction of the Cambridge Philosophical Society* 8, pp. 441–473.

Suzuki, T. (2011). Wave Dissipation Over Vegetation Fields. PhD thesis. Delft University of Technology.

Suzuki, T., M. Zijlema, B. Burger, M.C. Meijer, and S. Narayan (2011). Wave dissipation by vegetation with layer schematization in SWAN. *Coastal Engineering* 59 (1), pp. 64–71.

Swisher, M. (1982). The rates and causes of coastal erosion around a transgressive caoastal lagoon, Rehoboth Bay, Delaware. MA thesis. University of Delaware, Newark.

Temmerman, S., P. Meire, T.J. Bouma, P.M.J. Herman, T. Ysebaert, and H.J. De Vriend (2013). Ecosystem-based coastal defence in the face of global change. *Nature* 504 (7478), pp. 79–83.

Thorne, C.R. and N.K. Tovey (1981). Stability of composite river banks. *Earth Surface Processes and Landforms* 6 (5), pp. 469–484.

Toffolon, M. and S. Lanzoni (2010). Morphological equilibrium of short channels dissecting the tidal flats of coastal lagoons. *Journal of Geophysical Research: Earth Surface* 115 (F4).

Tonelli, M., S. Fagherazzi, and M. Petti (2010). Modeling wave impact on salt marsh boundaries. *Journal of Geophysical Research: Oceans* 115 (C9).

Toro, E.F. (2009). *Riemann Solvers and Numerical Methods for Fluid Dynamics: a Practical Introduction.* Springer Science and Business Media.

Trenhaile, A.S. (2009). Modeling the erosion of cohesive clay coasts. *Coastal Engineering* 56 (1), pp. 59–72.

Tsai, C.-H., M.-C. Huang, Fu-Ji Young, Y.-C. Lin, and H.-W. Li (2005). On the recovery of surface wave by pressure transfer function. *Ocean Engineering* 32 (10), pp. 1247–1259.

Tuan, Q.T. and H. Oumeraci (2012). Numerical modelling of wave overtopping-induced erosion of grassed inner sea-dike slopes. *Natural hazards* 63 (2), pp. 417–447.

Turner, R.E., E.M. Swenson, C.S. Milan, J.M. Lee, and T.A. Oswald (2004). Below-ground biomass in healthy and impaired salt marshes. *Ecological Research* 19 (1), pp. 29–35.

Valiela, I. and J.M. Teal (1979). The nitrogen budget of a salt marsh ecosystem. *Nature* 280 (5724), pp. 652–656.

Van de Koppel, J., D. Van der Wal, J.P. Bakker, and P.M.J. Herman (2005). Self-organization and vegetation collapse in salt marsh ecosystems. *The American Naturalist* 165 (1), E1–E12.

Van der Meer, J.W., H.J. Verheij, J. Lindenberg, A. Van Hoven, and G.J.C.M. Hoffmans (2007). *Wave overtopping and strenght of inner slopes of dikes.* Tech. rep. 05i028. in Dutch. WL|Delft Hydraulics, Geodelft.

Van der Wal, D. and K. Pye (2004). Patterns, rates and possible causes of saltmarsh erosion in the Greater Thames area (UK). *Geomorphology* 61 (3), pp. 373–391.

Van der Wal, D., A. Wielemaker-Van den Dool, and P.M.J. Herman (2008). Spatial patterns, rates and mechanisms of saltmarsh cycles (Westerschelde, The Netherlands). *Estuarine, Coastal and Shelf Science* 76 (2), pp. 357–368.

Van Eerdt, M.M. (1985). Salt marsh cliff stability in the Oosterschelde. *Earth Surface Processes and Landforms* 10 (2), pp. 95–106.

Van Eerdt, M.M. (1985). The influence of vegetation on erosion and accretion in salt marshes of the Oosterschelde, The Netherlands. *Vegetation* 62 (1-3), pp. 367–373.

Van Kessel, T., A. Spruyt-de Boer, J. Van der Werf, L. Sittoni, B. van Proijen, and H. Winterwerp (2012). *Bed module for sand-mud mixtures, Report in the framework of Building with Nature Project NTW 1.3 Mud Dynamics.* Tech. rep. Deltares.

Van Ledden, M. (2003). Sand-mud segregation in estuaries and tidal basins. PhD thesis. TU Delft, Delft University of Technology.

Van Ledden, M., W.G.M. Van Kesteren, and J.C. Winterwerp (2004). A conceptual framework for the erosion behaviour of sand–mud mixtures. *Continental Shelf Research* 24 (1), pp. 1–11.

Van Loon-Steensma, J.M. (2015). Salt marshes to adapt the flood defences along the Dutch Wadden Sea coast. *Mitigation and Adaptation Strategies for Global Change*, pp. 1–20.

Van Proijen, B.C. (2012). *Considerations on a generic water-bed exchange module.* Tech. rep. TU Delft, Delft University of Technology.

Van Rijn, L.C. (1984). Sediment transport, part I: bed load transport. *Journal of Hydraulic Engineering* 110 (10), pp. 1431–1456.

Van Rijn, L.C. (1984). Sediment transport, part II: suspended load transport. *Journal of Hydraulic Engineering* 110 (11), pp. 1613–1641.

Van Rijn, L.C. (1993). *Principles of Sediment Transport in Rivers, Estuaries and Coastal Seas.* Vol. 2. 3. Aqua publications Amsterdam.

Van Thiel de Vries, J.S.M. (2009). Dune erosion during storm surges. PhD thesis. TU Delft, Delft University of Technology.

Vellinga, P. (1986). Beach and dune erosion during storm surges. PhD thesis. TU Delft, Delft University of Technology.

Waeles, B., P. Le Hir, P. Lesueur, and N. Delsinne (2007). Modelling sand/mud transport and morphodynamics in the Seine river mouth (France): an attempt using a process-based approach. *Hydrobiologia* 588 (1), pp. 69–82.

Weinstein, M.P. and D.A. Kreeger (2000). *Concepts and controversies in tidal marsh ecology*. Springer Science & Business Media.

Welch, P. (1967). The use of fast Fourier transform for the estimation of power spectra: a method based on time averaging over short, modified periodograms. *IEEE Transactions on audio and electroacoustics*, pp. 70–73.

Wilson, C.A. and M.A. Allison (2008). An equilibrium profile model for retreating marsh shorelines in southeast Louisiana. *Estuarine, Coastal and Shelf Science* 80 (4), pp. 483–494.

Winterwerp, J.C. (1999). On the dynamics of high-concentrated mud suspensions. PhD thesis. TU Delft, Delft University of Technology.

Winterwerp, J.C. (2002). On the flocculation and settling velocity of estuarine mud. *Continental shelf research* 22 (9), pp. 1339–1360.

Winterwerp, J.C., W.G.M. Kesteren, B.C. Prooijen, and W. Jacobs (2012). A conceptual framework for shear flow–induced erosion of soft cohesive sediment beds. *Journal of Geophysical Research: Oceans* 117 (C10).

Winterwerp, J.C. and W.G.M. Van Kesteren (2004). *Introduction to the Physics of Cohesive Sediment Dynamics in the Marine Environment*. Ed. by T. Van Loon. Vol. 56. Development in Sedimentology. Elsevier.

Wolf, J. (1997). The analysis of bottom pressure and current data for waves. *7th International Conference on Electronic Engineering in Ocanography*. 49. Institute of Electronic Engineering. IET.

Wu, T.H., W.P. McKinnell III, and D.N. Swanston (1979). Strength of tree roots and landslides on Prince of Wales Island, Alaska. *Canadian Geotechnical Journal* 16 (1), pp. 19–33.

Xie, S.-L. (1981). Scouring patterns in front of vertical breakwaters and their influences on the stability of the foundation of the breakwaters. PhD thesis. TU Delft, Delft University of Technology.

Yalin, M.S. (1972). *Mechanics of sediment transport*. Pergamon press.

Young, I.R. and L.A. Verhagen (1996). The growth of fetch limited waves in water of finite depth. Part 1. Total energy and peak frequency. *Coastal Engineering* 29 (1), pp. 47–78.

Yu, I.S., P.S. Yu, O. Giovanardi, and L. Dalla Venezia (1996). Study of the ecosystem of the Lagoon of Venice, with emphasis on anthropogenic impact. *Marine Ecology Progress Series* 141, pp. 247–261.

Zanuttigh, B. and J.W. van der Meer (2008). Wave reflection from coastal structures in design conditions. *Coastal Engineering* 55 (10), pp. 771–779.

Zedler, J.B. and S. Kercher (2005). Wetland resources: status, trends, ecosystem services, and restorability. *Annuual Review of Environment and Resources* 30, pp. 39–74.

Zijlema, M., G. Stelling, and P. Smit (2011). SWASH: An operational public domain code for simulating wave fields and rapidly varied flows in coastal waters. *Coastal Engineering* 58 (10), pp. 992–1012.